Toroidal event horizons and other relativistic ray tracing adventures

A Dissertation

Presented to the Faculty of the Graduate School

of Cornell University

in Partial Fulfillment of the Requirements for the Degree of

Doctor of Philosophy

by

Andrew Douglas Bohn

August 2016

TOROIDAL EVENT HORIZONS AND OTHER RELATIVISTIC RAY TRACING ADVENTURES

Andrew Douglas Bohn, Ph.D.

Cornell University 2016

This thesis deals with the appearance of colliding black holes from two vantage points, dividing the thesis into two parts.

Part I (Chapters 2 to 4) investigates the topology of merging black hole event horizons. Chapter 2 introduces a new code for locating event horizons in numerical simulations. The code can automatically refine arbitrary regions of the event horizon surface to find features such as the hole in a toroidal event horizon.

With these tools, Chapter 3 shows the first binary black hole event horizon with a toroidal topology. It had been predicted that generically the event horizons of merging black holes should briefly have a toroidal topology, but such a phase has not been seen prior to this work. In all previous binary black hole simulations, in the coordinate slicing used to evolve the black holes, the topology of the event horizon transitions directly from two spheres during the inspiral to a single sphere as the black holes merge. Chapter 3 presents a transformation of the time coordinate that results in a toroidal event horizon. A torus could potentially provide a mechanism for violating the so-called topological censorship theorem; however, since these toroidal event horizons arise from a coordinate choice, they can be removed by the inverse coordinate transformation and do not violate the theorem.

Chapter 4 presents work toward reslicing the event horizon on slices of constant affine parameter in an effort to find an event horizon on a toroidal topology.

Part II (Chapters 5 and 6) considers what a binary black hole merger actually looks like for a nearby observer. Chapter 5 presents both demonstrative images illustrating details of the spatial distortion and realistic images of collections of stars taking both lensing amplification

and redshift into account. On large scales, the lensing from inspiraling binaries resembles that of single black holes, but on small scales the resulting images show complex and in some cases self-similar structure across different angular scales.

Chapter 6 presents miscellaneous gravitational lensing projects including producing content for the LIGO press conference for the first ever detection of gravitational waves. We also present a project visualizing physically accurately an accretion disk around a black hole, similar to the system from the movie *Interstellar*.

Biographical Sketch

Andy was born in Wyandotte, Michigan in September 1987 to Michael and Kimberly Bohn. Shortly after, he and his family moved to northwest Indiana (neither to be confused with nor associated with the rest of Indiana), where he was raised. He went to high school at Lake Central High School in Saint John, Indiana from 2002-2006, where he spent most of this time drumming. He auditioned and was selected for the first Bands of America honor band snare line in 2004, to march in the Tournament of Roses Parade in Pasadena, California. He also composed and performed in a bass drum ensemble winning the Indiana Percussion state championship in 2005.

In 2006, he began collegiate studies at Purdue University in West Lafayette, Indiana, where he majored in both Honors Physics and Mathematics. At Purdue, he investigated how to focus the Large Synoptic Survey Telescope using intra-focal and extra-focal images, under the supervision of Ian Shipsey. He spent the summer of 2008 at Caltech studying the strength and thermal noise of laser pulled and polished fused silica glass fibers to hold the 40 kg mirrors for the Advanced LIGO detectors.

In the summer of 2010, he began research at Cornell University under Julia Thom studying AC coupling in Silicon on insulator devices for the Large Hadron Collider. The following summer, he joined the Simulating eXtreme Spacetimes collaboration under Saul Teukolsky and Lawrence Kidder studying event horizons in merging black hole systems, where he carried out the work for this thesis. He received his Master's degree in 2013.

He accepted a position at SpaceX in early 2016, where he will begin as a flight software engineer for low Earth orbit satellites in late July 2016.

In the immortal words of my Dad, “now hear this!”

Acknowledgments

This thesis would not have been possible without the help and support of a large number of people.

I would like to begin by thanking my advisors, starting with my professorial advisor, Saul Teukolsky. In addition to providing many useful suggestions on the direction of my research and frequently recalling relevant page numbers from Numerical Recipes on demand, he treated me like an adult instead of a subordinate. I am very grateful for everything I have learned from my time with Saul, from approaching problems with first principles and simple base cases, to the proper way to write delicate emails by "always starting with a compliment." My work was additionally mentored by Larry Kidder, with whom I grew a strong rapport. His door was always open for me to bug him with arcane questions regarding the inner workings of scary portions of SpEC, or to chat about board games and debate if Minnesota or Detroit had worse sports outings the previous night. He managed to simultaneously be a friend and mentor. I could not have asked for a better pair of advisors. Thanks also go to my additional defense committee members Éanna Flanagan who miraculously managed to teach me some General Relativity and Cosmology, and Julia Thom for graciously agreeing to sit through my thesis and defense.

I am obliged to thank some of my officemates: Dan Hemberger for surviving DotA sessions with me, Kate Henriksson for making Debatable less debatable, and my psuedo-officemate Curran Muhlberger for indulging random computer science discussions and opening the channel from SXS to SpaceX. I would have been unable to complete this work without François Hébert and Will Throwe for being an absolute joy to work with for five years, engaging with me in often poorly founded research conversations, and enabling the successes of the gravitational lensing project. I also need to thank the latecomer to the office Nils Deppe for being an irreplaceable and unyielding *Strahlkorper* to me in the office every day.

I would like to thank the whiskey group of Cody Long, Ethan Kassner, John Stout, and Brian Leahy for fantastic tastings that were brief, civil, and classy. Special thanks go to

Ethan for living with me for almost 20% of my life, playing Mario Kart 64, and watching "Always Sunny" with the finest whiskey Canada has to offer. A song for Matt: Matt Bierbaum, Matt Bierbaum, opening up reddit.com; He is aplomb, and he is the bomb, Matt Bierbaum. Thanks to Corky "Robert" Wharton for being the Sir Donald Bradman of entertainment, but at last it is time for me to cash out of the Wharton money-friendship uncertainty principle $\sigma_m \sigma_f \geq \hbar/2$.

Finally, and most of all, I would like to thank my family, to whom I dedicate my thesis. My sister Emily, who I have always admired for her ability to battle through incredible adversities not limited to having to deal her brothers while growing up; e$\times$hale $\rightarrow$ Space$\times$!; My brother Mike, for getting me started with programming and fostering my curiosity through (mostly) playful competitiveness; My brother-in-law Alex, for indulging me with puzzles, generally nerdy maths, and being a fantastic addition to the family; My mom and dad, who taught me how to be inquisitive and empathetic, and provided me with everything I could have possibly needed and more; And to my _____ wife _____, may we have _____ more year(s) of _____ and _____! I love you all.

I thank not only those who I mentioned here, but everyone who has had a positive impact on my life.

Table of Contents

List of Figures

List of Tables

1 Introduction

"*The moon falls, even tho it gets no closer.*"

– Richard Feynman [1]

It is a great time to be a numerical relativist. We are currently striding along a rich avenue of opening doors and windows, with a decade of incremental successes in binary black hole simulations, ever increasing computational resources at our disposal, and of course the first detection of gravitational waves from merging black holes by Advanced LIGO in 2015. The universe blessed us by colliding black holes over a billion years ago and carrying the resulting violent ripples through spacetime toward Earth so that, one century after Einstein formulated General Relativity, we could detect their now faint blips with an pair of elaborate detectors.

With the hope that Advanced LIGO will detect an accelerating number of gravitational wave signals as technology and understanding improves, we are transitioning into the age of "multi-messenger astronomy." Traditionally, astronomy has depended only on detecting light in a wide range of frequencies from radio waves to gamma rays. The dream is to observe a single event in our universe, like a binary black hole merger or supernova core collapse, using both traditional astronomy as well as gravitational wave astronomy. However, even simply accumulating more gravitational wave signals will propel gravitational theory far into the future.

This thesis advances our understanding of binary black hole mergers. It is split cleanly into two parts: Part I (Chapters 2 to 4) studies the topology of the event horizons during

the merger, and Part II (Chapters 5 and 6) studies how systems such as merging black holes strongly deflect light that passes nearby. I begin this section with a brief history of gravitational theory in Section 1.1, introduce some basics of General Relativity in Section 1.2, and finish with useful background for the thesis in Section 1.3.

1.1 Brief history of gravitational theory

There are four fundamental interactions in nature: electromagnetism, the force between electrically charged particles that describes phenomena like friction and light; the strong nuclear force, an incredibly short range and powerful force responsible for holding subatomic particles together; the weak nuclear force that governs nuclear phenomena such as radioactive decay; and gravitation, the weakest of the interactions that is nevertheless the most important over large distances. Gravity explains the orbit of the Earth around the Sun, the rise and fall of the tides, and the formation of stars and galaxies. In the pursuit to understand the fundamental interactions of the universe, gravitation was the first to be characterized mathematically, in the 17^{th} century by Isaac Newton [2].

Some early ideas about gravitation came from Greek philosophers such as Aristotle [3], who believed that all bodies move toward their "natural place." The element earth was thought to be the heaviest, so its natural place was beneath our feet toward the center of the universe. Covering the earth were lighter elements such as water, and air which is lighter than water since bubbles rise in water. Fire is even lighter than air, and therefore rises in air. Aristarchus of Samos [4] was the first to propose the *heliocentric* model that the Sun was at the center of the universe, around which the Earth revolved. The heliocentric model was largely rejected, however, in favor of *geocentric* models placing the Earth at the center of the universe.

These ideas persisted until the 17^{th} century, when Johannes Kepler [5] analyzed the positions of the planets as recorded over many years by Tycho Brahe. From this data, Kepler discovered three laws of planetary motion, but did not provide physical mechanisms for the

motion.

> "*While Kepler was discovering these laws, Galileo was studying the laws of motion. The problem was, what makes the planets go around? (In those days, one of the theories proposed was that the planets went around because behind them were invisible angels, beating their wings and driving the planets forward. You will see that this theory is now modified! It turns out that in order to keep the planets going around, the invisible angels must fly in a different direction and they have no wings. Otherwise, it is a somewhat similar theory!)* "
>
> – Richard Feynman [1]

Galileo [6] discovered the concept of *inertia*, stating if something is moving, it will continue to move in that direction and speed as long as it is not disturbed. He was also able to realize that objects accelerate to Earth when dropped, where the height changes quadratically with the time since it was dropped. After a suggestion about the gravitational force from Robert Hooke, Isaac Newton [7] refined Galileo's ideas and was able to derive Kepler's three laws of planetary motion using inertia, the concept that a body changing speed means a force was applied in that direction, and a simple equation describing the gravitational force:

> "*I deduced that the forces which keep the planets in their orbs must be reciprocally as the squares of their distances from the centres about which they revolve, and thereby compared the force requisite to keep the moon in her orb with the force of gravity at the surface of the earth and found them answer pretty nearly.*"
>
> – Isaac Newton, 1666

Newton's quotation is summarized with the proportionality

$$F \propto \frac{M_1 M_2}{R^2}, \tag{1.1}$$

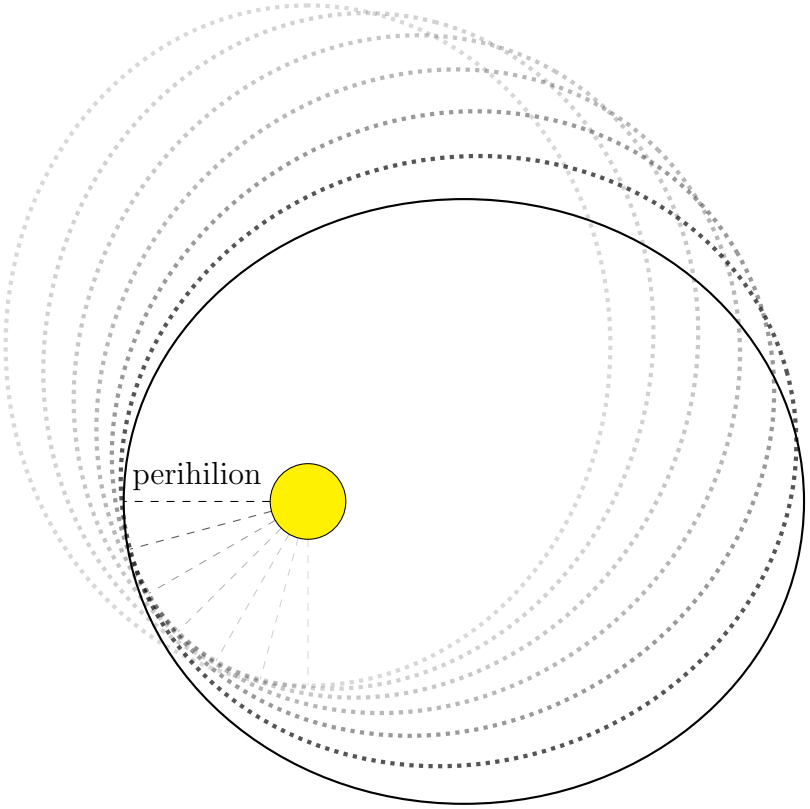

Figure 1.1: Perihilion precession around the Sun, where the point of closest approach of a planet to the Sun rotates around the Sun over time.

saying that the magnitude of the force between two objects with masses M_1 and M_2 is proportional to both of these masses, and inversely proportional to the square of the distance R between the masses. This is the first mathematical model describing gravitation, and describes the motion of objects in the Solar System to very high accuracy. The model also led to some bold predictions and discoveries. After analyzing the motion of the planet Uranus and finding irregularities, Urbain Le Verrier and John Couch Adams deduced with Newton's theory that there should be another planet, not yet seen, orbiting the Sun near Uranus [8]. Johann Gottfried Galle was then able to confirm the prediction by finding the planet Neptune [9].

Newtonian gravity predicts that, in the absence of any other masses, planets such as Mercury will trace out an ellipse with the Sun at a focus of the ellipse. The point where Mercury passes closest to the Sun, called *perihilion*, largely should not change position. Other

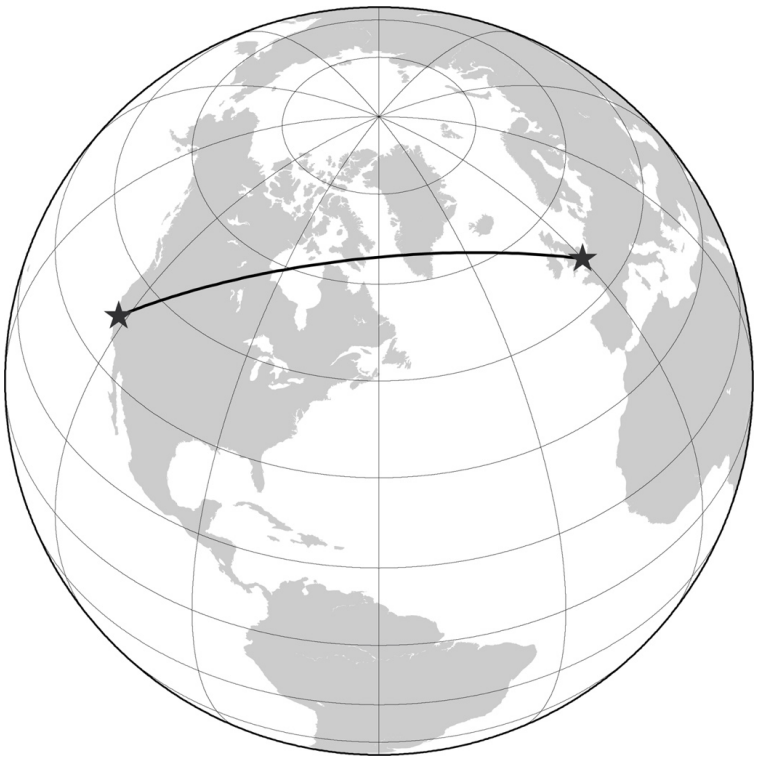

Figure 1.2: The shortest path for a flight across the Atlantic Ocean appears bent because of the curved surface of the Earth. Figure source: [11]

nearby masses will cause the Mercury's perihilion to slightly rotate around the Sun over time, as shown in Figure 1.1. The precession of the perihilion did not follow Newton's gravitational theory, implying there might be a missing massive body near Mercury. However, unlike the case with the missing planet Neptune, no one could find any such mass.

This issue was not resolved until 1915, when Albert Einstein [10] produced his theory of General Relativity that remarkably accurately predicted the motion of Mercury as well as many other phenomena.

1.2 General Relativity

"*Spacetime tells matter how to move; matter tells spacetime how to curve.*"

– John Archibald Wheeler

In General Relativity (GR), gravity is not described as an instantaneous force between

objects as in Newtonian theory, but the effects of gravity travel at the speed of light and are caused by the geometry of spacetime. Instead of the Earth feeling a gravitational force from the Sun causing the Earth to orbit the Sun, in GR, the Sun curves spacetime and the Earth moves in a straight line through this curvature. To understand how curved geometry changes the intuitive understanding of straight lines, consider a flight from California across the Atlantic Ocean, shown in Figure 1.2. The airline obviously would like to save money on fuel by taking the shortest route. We know that the shortest path between two points on a piece of paper is a straight line, but how do things change when the "piece of paper" is curved like the surface of the Earth? The term *geodesic* generalizes the idea of a straight line to spaces that are curved, where a geodesic is the shortest path between two points in curved space. Because the Earth's surface is curved, the shortest geodesic flight path does not appear as a straight line but appears bent. The trajectory of this airplane is analogous to how objects move in General Relativity.

We know that the Earth orbits the Sun, and this is explained in GR by the idea that the Earth follows a geodesic through spacetime that is primarily curved by the Sun. All objects try to follow a geodesic through spacetime, unless they are acted on by some external force such as the ground preventing people from falling toward the center of the Earth. We do not experience gravity pulling down on us, but only feel these external forces.

In addition to more accurately explaining the motions of objects we observe in the universe, GR predicts some very interesting phenomena. One prediction is the existence of *black holes*, where if mass is compressed into a sufficiently compact region of space, the curvature of spacetime will be so great that not even light can escape. A black hole behaves like a perfect black body, reflecting no light and radiating light [12] as if it had a temperature T that was inversely proportional to its mass. Therefore massive black holes radiate extremely slowly as if they had a small temperature.

Even though General Relativity is based on a simple-to-state idea, the mathematics involved are more complicated than the those required to study Newtonian gravity, where

many problems can be solved with algebra alone. GR uses the tools of differential geometry, a discipline of mathematics that describes curved surfaces and spaces. The warping of spacetime is described by the Einstein field equations

$$G_{\mu\nu} = 8\pi T_{\mu\nu}, \tag{1.2}$$

a set of 10 equations where $T_{\mu\nu}$ is the energy-momentum tensor describing the density and flux of energy and momentum in spacetime, and $G_{\mu\nu}$ is the Einstein tensor describing the curvature of spacetime in response to $T_{\mu\nu}$.

Karl Schwarzschild [13] found the first exact solution to Einstein's field equations, the solution for the spacetime outside a spherical mass:

$$d\lambda^2 = -\left(1 - \frac{r_s}{r}\right) dt^2 + \left(1 - \frac{r_s}{r}\right)^{-1} dr^2 + r^2 \left(d\theta^2 + \sin^2\theta d\phi^2\right). \tag{1.3}$$

Here $d\lambda^2$ that describes the invariant distance between two nearby points around the spherical mass, with r_s a constant proportional to the mass. Schwarzschild formulated this solution while serving on the Russian front in World War I, and subsequently sent Einstein his result only a month after GR was introduced. Einstein replied,

> "*I have read your paper with the utmost interest. I had not expected that one could formulate the exact solution of the problem in such a simple way. I liked very much your mathematical treatment of the subject. Next Thursday I shall present the work to the Academy with a few words of explanation.*"
>
> – Albert Einstein [14]

When tracing geodesics through the Schwarzschild solution, physicists found there was a magic sphere of radius r_s beyond which geodesics would not penetrate. Coincidentally, schwarzschild translated from German to English means "black shield." This black shield at radius r_s turned out to simply be a poor choice of coordinates, and in reality geodesics

can penetrate through it. However, geodesics that enter this sphere can never leave it. If an object could be compressed so tightly that all the mass was contained within the radius r_s, then object would become a black hole with an *event horizon* at r_s. An event horizon is by definition the surface of a black hole, and is the boundary beyond which light cannot escape.

1.3 Thesis overview

Geodesics, black holes, and event horizons are the subjects under consideration for this work. Part I focuses on merging black holes and the topology of their associated event horizons. We are interested in precisely how two black holes transition into one, in the sense of topology.

The event horizon in Schwarzschild's spherically symmetric spacetime is a perfect sphere of radius r_s, called the Schwarzschild radius, satisfying

$$r_s = \frac{2G}{c^2} M, \tag{1.4}$$

where G is the gravitational constant, c is the speed of light, and M is the mass of the central object. This suggests that if a distorted object with mass M is condensed into a sphere with radius smaller than r_s, then it will collapse to a black hole. This idea is known as the *Hoop Conjecture* from Thorne [15, 16]. The radius of the event horizon scales linearly with the mass of the objectwhere the coefficient $2G/c^2$ is incredibly small, $\mathcal{O}(10^{-27})\,\mathrm{m/kg}$. For examples, the mass of the Sun is about $\mathcal{O}(10^{30})\,\mathrm{kg}$, meaning it would collapse to a black hole if it were compressed to a sphere of radius $\mathcal{O}(1)\,\mathrm{km}$, or Earth is $\mathcal{O}(3 \times 10^5)$ times lighter so it would need to be compressed to a sphere of radius $\mathcal{O}(1)\,\mathrm{cm}$.

The Schwarzschild solution found in 1916 describes non-rotating black holes. The solution for rotating black holes is more complicated and was not found until 1963 when it was discovered by Roy Kerr [17]. The event horizon around a rotating black hole (in some coordinate systems) is not simply a sphere, but an oblate spheroid, like the shape that occurs after lightly squeezing opposite sides of a balloon. Nevertheless, both event horizons (and the

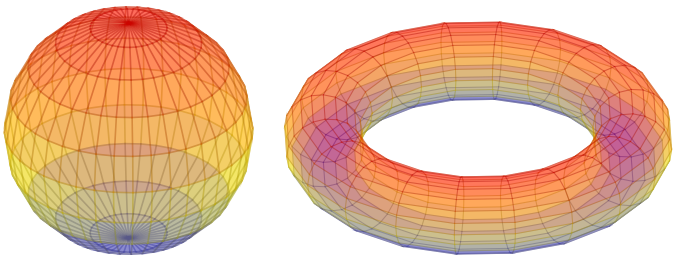

(a) Sphere ($\mathcal{S}^2$) (b) Torus ($\mathcal{T}^2$)

Figure 1.3: Topologically distinct surfaces, a sphere and a torus

balloon) have the spatial topology of a 2-sphere ($\mathcal{S}^2$), because they enclose a three dimensional volume and there are no holes through the surface. Therefore, the oblate spheroid and sphere are said to be *homeomorphic*, where, simply stated, one shape can be continuously morphed into the other without tearing the shape or gluing parts of it together. An example of a shape that is not homeomorphic to a sphere is a donut with a hole in it, which has the topology of a torus ($\mathcal{T}^2$). When attempting to morph a sphere into a torus, the sphere would need to be ripped and glued back together to form the hole for the torus. Examples of a sphere and a torus are shown in Figure 1.3.

The event horizon is formally a $2+1$-dimensional hypersurface. Looking at the Schwarzschild event horizon at a given instant in time on a spatial plane called a *Cauchy surface*, the event horizon is a 2-dimensional sphere in a 3-dimensional space. After combining together all possible instants in time, we obtain the global structure of the event horizon which is a $2+1$-dimensional hypersurface in $3+1$-dimensional spacetime. To be clear, when we speak about the topology of the event horizon in this work, unless otherwise specified we mean the spatial topology on specified Cauchy surfaces as opposed to the global topology of the full $2+1$-dimensional event horizon. The global topology is independent of the coordinate system, but as we will see, the spatial topology of the event horizon is dependent on the Cauchy surfaces used to view the event horizon. In other words, the spatial topology of the event horizon is a coordinate dependent phenomenon. However, this does not mean that any spatial topology is possible, because we restrict ourselves to using Cauchy surfaces. Cauchy surfaces are spacelike hypersurfaces, meaning the normal to any location on the

hypersurface is timelike, or in the light cone. Each hypersurface corresponds to the spatial volume accessible to some physical observer.

With the physically reasonable assumption that the dominant energy condition holds, meaning matter density is never observed to be negative and mass-energy cannot move faster than the speed of light, stationary black hole spacetimes should contain an event horizon with a spherical topology [18, 19, 20]. The stationary condition states that the metric describing the spacetime is independent of time. The Schwarzschild and Kerr spacetimes are both stationary and both contain event horizons that are topological spheres, so they support this result. Until the 1970s, it was thought that only spherical event horizons were possible.

However, the topology can be more complicated when the spacetime is allowed to change with time. In 1976, Gannon [21] showed that smooth dynamical black hole event horizons could either have a spherical or a toroidal topology, permitting the possibility of an event horizon shaped like a torus. A spacetime with a toroidal event horizon must not be stationary, because the event horizon would otherwise be forced to have a spherical topology as shown earlier. In fact, the hole through the toroidal event horizon must itself be a time dependent feature of the spacetime.

In 1993, a theorem called *topological censorship* [22] was published stating that observers cannot probe any topological structure of the spacetime. A way for an observer to attempt to probe or examine a topological structure such as the hole through a toroidal event horizon is by passing photons through the hole. The way to both satisfy topological censorship and also have a toroidal event horizon is by enforcing that the hole in the torus close faster than it takes light to traverse the hole [22, 23, 24]. Such a quickly collapsing toroidal event horizon would only look like a torus in *some* coordinate systems. A different coordinate system must always exist where the topology is spherical for this event horizon [25, 26]. In this way, observers trying to pass photons through the hole in the torus could not say in a coordinate independent way that a hole in the event horizon existed.

This idea can be understood in the language of Special Relativity and with an event

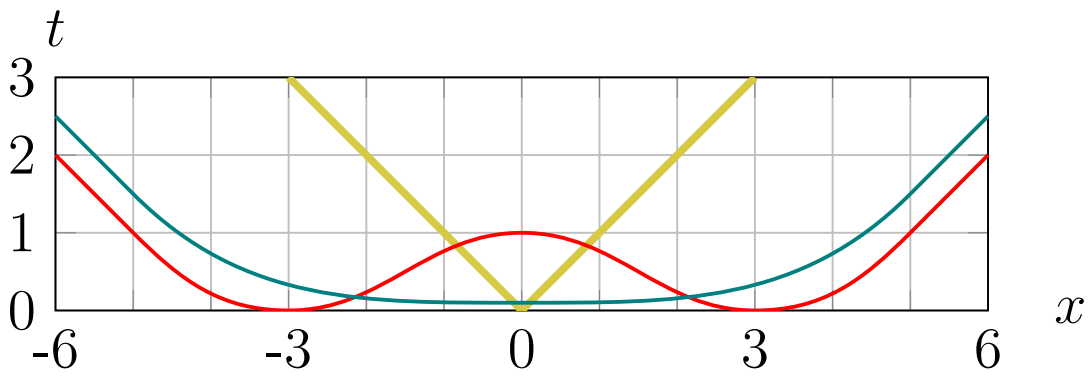

(a) Spacetime diagram with light rays in yellow, a toroidal event horizon in red, and a resliced event horizon in blue

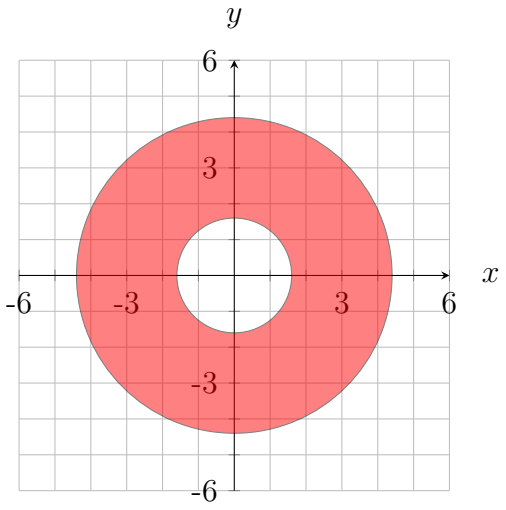

(b) red surface at $t = 0.5$

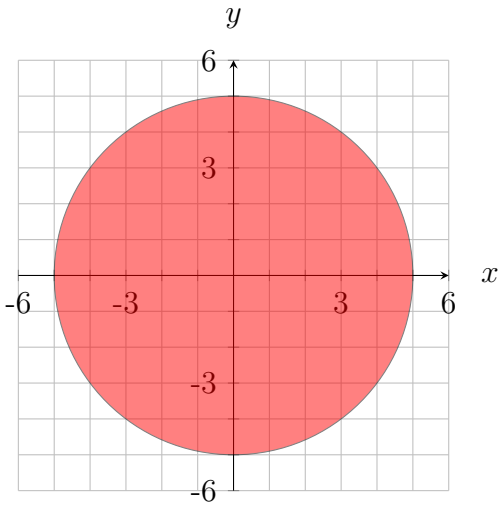

(c) red surface at $t = 1$

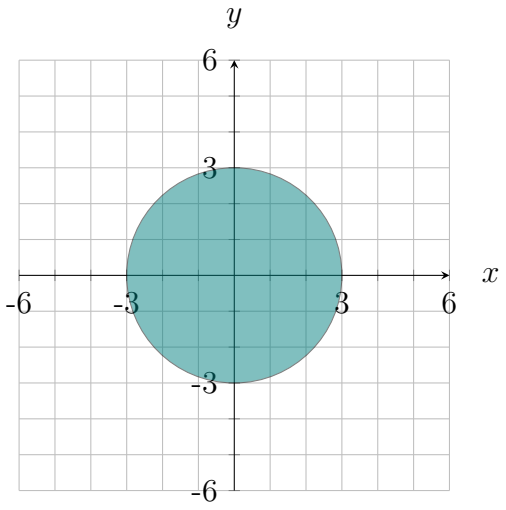

(d) blue surface at $t = 0.5$

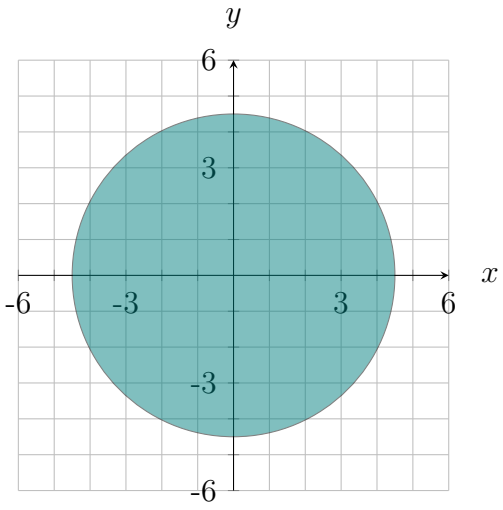

(e) blue surface at $t = 1$

Figure 1.4: A toroidal event horizon model where the hole in the torus in the torus closes faster than the speed of light. The red and blue data correspond to the same event horizon in coordinate systems where the topology is different.

horizon that appears initially as a torus. In Figure 1.4, we see a spacetime diagram in panel (a) showing the boundary of this event horizon surface in red and a light cone in yellow. Panel (b) shows what the horizon looks like in the xy-plane at $t = 0.5$. At this time, the event horizon has a toroidal topology, and the hole through the surface is closing quickly into panel (c) at $t = 1$. The spacetime diagram in panel (a) shows the edge of the hole at $t = 0$, $x = \pm 3$, and that the hole closes at $t = 1$, $x = 0$. These two events in spacetime are separated by a spacelike interval, meaning light does not have enough time to travel between them. Because of this fact, we can find another coordinate system that makes the event at $t = 1$, $x = 0$ occur before the events at $t = 0$, $x = \pm 3$, meaning there would never be a hole in the event horizon. In the new coordinate system shown in blue, the event horizon initially appears at $t' = 0$, $x' = 0$ and grows outward. Panels (d) and (e) show that the event horizon in this coordinate system never has a hole. In the language of General Relativity, the portion of the event horizon surface between $x = \pm 3$ is a spacelike hypersurface. The setup in Figure 1.4 closely represents numerical simulations of the collapse of a rotating distribution of matter, where the event horizon initially appeared with a toroidal topology that quickly transitioned into a sphere [27, 28].

The situation with merging black holes is more complicated. Siino [26] and Husa and Winicour [29] predicted that the event horizon of a generic binary black hole system should briefly exhibit a toroidal topology during the merger. However, no toroidal event horizons have been found in numerical simulations of merging black holes. The topology has only been seen to transition from two spheres during the inspiral to a single sphere after the merger. Cohen *et al.* [30] of the Simulating eXtreme Spacetimes (SXS) collaboration studied a range of binary black hole mergers and found that the event horizon always had a spherical topology. They argued that part of the full $2+1$-dimensional event horizon lived on a spacelike hypersurface as in Figure 1.4, implying that it was possible to find another coordinate system where the event horizon was toroidal. However, they did not exhibit such a coordinate system and the discrepancy between the theoretical expectation and the numerical simulations

remained. Simulations of three black holes [31] and eight black holes in a ring [32] similarly did not exhibit a toroidal event horizon, where the hope was that the event horizons would join together in a ring before joining together at the origin.

In Part I, we find results in agreement with Cohen *et al.* [30] that the topology of the event horizon for binary black hole mergers transitions from two spheres to a single sphere in the coordinate system used to merge the binary. However, we explicitly perform a coordinate transformation to a new coordinate system where the event horizon briefly has a toroidal topology. We therefore confirm that toroidal event horizons are possible in generic binary black hole mergers, yet they only appear in some coordinate systems. We also show that it is possible to change the topology of the event horizon before the merger from two spheres during the inspiral to a brief period with three spheres before all the spheres merge. The additional sphere showing up during the merger we call a "baby" event horizon, and is also only seen in certain coordinate systems.

However, this is not what can be detected by an observer. In Part II, we explore what an observer near merging black holes would see as the black holes inspiral, merge, then settle to a stationary black hole by tracing rays of light through the spacetime. This project was spawned by childhood curiosities, unadulterated enjoyment, and 2 A.M. frustrations in the office. In General Relativity, the path of light is bent by the curvature of spacetime, a phenomenon called gravitational lensing. Starlight passing by the Sun has been directly observed, but this deflection is only about 2 arc seconds, or 5×10^{-4} degrees. Of course the situation is more interesting when compact objects like black holes are involved. The maximum possible deflection of light passing by a black hole is in theory unlimited, since photons can orbit the black hole many times before eventually escaping.

Although no light is emitted from black holes, we get some interesting images when looking at a black hole. Because black holes strongly deflect photons that pass nearby, we get a distorted view of not only stars behind the black hole, but stars everywhere in the universe including behind the camera! The gravitational lensing of a single black hole has been studied

for roughly a century, and detailed images began appearing in the 1970s. However, no one had studied what merging black holes should look like because of the complexities of both solving for the spacetime around merging black holes, as well as tracing photons to probe the spacetime. Thankfully, in the SXS collaboration we have an accurate and fast laboratory for simulating merging black holes. And I had already written a general parallelized ray tracer for GR for the purpose of locating event horizons. With these tools at our disposal, William Throwe, François Hébert, and I began our quest to answer the question "What does a binary black hole merger look like?"

The result of this work was featured in the LIGO press conference announcing the first direct detection of gravitational waves. A century after Einstein revealed General Relativity to the world, we are able to use supercomputers to see what observers near merging black holes would actually see during the violent collision. Perhaps another century from now we will be able to travel to these systems and see them with our own eyes.

Bibliography

[1] Richard P Feynman, Robert B Leighton, and Matthew Sands. *The Feynman Lectures on Physics, Desktop Edition Volume I*, volume 1. Basic books, 2013.

[2] PhilosophiæNaturalis Principia Mathematica (Newton's personally annotated 1st edition). http://cudl.lib.cam.ac.uk/view/PR-ADV-B-00039-00001/. Accessed: June 2, 2016.

[3] Istvan Bodnar. Aristotle's natural philosophy. In Edward N. Zalta, editor, *The Stanford Encyclopedia of Philosophy*. Spring 2012 edition, 2012.

[4] Thomas Heath. *Aristarchus of Samos, the Ancient Copernicus: A History of Greek Astronomy to Aristarchus, Together with Aristarchus's Treatise on the Sizes and Distances of the Sun and Moon*. Cambridge University Press, 2013.

[5] Johannes Kepler, Eric J Aiton, Alistair Matheson Duncan, and Judith Veronica Field. *The harmony of the world*, volume 209. American Philosophical Society, 1997.

[6] Henrik Lagerlund. *Encyclopedia of medieval philosophy: philosophy between 500 and 1500*, volume 1. Springer Science & Business Media, 2010. p. 504.

[7] I Bernard Cohen and George E Smith. *The Cambridge Companion to Newton*. Cambridge University Press, 2002.

[8] Roger Hutchins. Adams, John Couch (1819–1892). *Oxford Dictionary of National*

Biography, 2004. http://www.oxforddnb.com/view/article/123 (accessed May 25, 2016).

[9] A Brief History of Astronomy in Berlin and the Wilhelm-Foerster-Observatory. http://www.planetarium-berlin.de/pages/hist/WFS-History.html. Accessed: May 25, 2016.

[10] A Einstein. The foundation of the generalised theory of relativity. *On a Heuristic Point of View about the Creation and Conversion of Light 1 On the Electrodynamics of Moving Bodies 10 The Development of Our Views on the Composition and Essence of Radiation 11 The Field Equations of Gravitation 19 The Foundation of the Generalised Theory of Relativity 22*, page 22, 1916.

[11] Schuyler Erle, Rich Gibson, and Jo Walsh. *Mapping hacks: tips & tools for electronic cartography.* " O'Reilly Media, Inc.", 2005.

[12] Stephen W Hawking. Particle creation by black holes. *Communications in mathematical physics*, 43(3):199–220, 1975.

[13] Karl Schwarzschild. On the gravitational field of a point mass according to einsteins theory. *Sitzungsber. Preuss. Akad. Wiss., Phys. Math*, 1916.

[14] Jean Eisenstaedt. The early interpretation of the schwarzschild solution. In D. Howard and John Stachel, editors, *Einstein and the History of General Relativity*. Birkhäuser, 1989.

[15] K. S. Thorne. In J. Klauder, editor, *Magic Without Magic; John Archibald Wheeler*. Frieman, San Francisco, 1972.

[16] Charles W. Misner, Kip S. Thorne, and John Archibald Wheeler. *Gravitation*. Freeman, New York, New York, 1973.

[17] R. P. Kerr. Gravitational Field of a Spinning Mass as an Example of Algebraically Special Metrics. *Phys. Rev. Lett.*, 11:237–238, September 1963.

[18] Steven W. Hawking and G. F. R. Ellis. *The Large Scale Structure of Space-time*. Cambridge University Press, Cambridge, England, 1973.

[19] S. W. Hawking. Black holes in general relativity. *Commun. Math. Phys.*, 25(2):152, 1972.

[20] Piotr T Chrusciel and Robert M Wald. On the topology of stationary black holes. *Class. Quantum Grav.*, 11(12):L147, 1994.

[21] Dennis Gannon. On the topology of spacelike hypersurfaces, singularities, and black holes. *Gen. Relativ. Gravit.*, 7(2):219, 1976.

[22] John L. Friedman, Kristin Schleich, and Donald M. Witt. Topological censorship. *Phys. Rev. Lett.*, 71(10):1486–1489, 1993. Erratum: [33].

[23] Gregory J Galloway. On the topology of the domain of outer communication. *Class. Quantum Grav.*, 12(10):L99, 1995.

[24] Ted Jacobson and Shankar Venkataramani. Topology of event horizons and topological censorship. *Class. Quantum Grav.*, 12(4):1055, 1995.

[25] Masaru Siino. Topological appearance of event horizon: What is the topology of the event horizon that we can see? *Progress of Theoretical Physics*, 99(1):1–32, 1998.

[26] Masaru Siino. Topology of event horizons. *Phys. Rev. D*, 58:104016, Oct 1998.

[27] S. A. Hughes, C. R. Keeton, P. Walker, K. T. Walsh, S. L. Shapiro, and S. A. Teukolsky. Finding black holes in numerical spacetimes. *Phys. Rev. D*, 49:4004, 1994.

[28] S. L. Shapiro, S. A. Teukolsky, and J. Winicour. Toroidal black holes and topological censorship. *Phys. Rev. D*, 52:6982, 1995.

[29] Sascha Husa and Jeffrey Winicour. The asymmetric merger of black holes. *Phys. Rev. D*, 60(8):084019, Sep 1999, gr-qc/9905039.

[30] Michael I. Cohen, Jeffrey D. Kaplan, and Mark A. Scheel. Toroidal horizons in binary black hole inspirals. *Phys. Rev. D*, 85:024031, 2012, 1110.1668.

[31] Peter Diener. A new general purpose event horizon finder for 3D numerical spacetimes. *Class. Quantum Grav.*, 20:4901–4917, 2003.

[32] M. Ponce, C. Lousto, and Y. Zlochower. Seeking for toroidal event horizons from initially stationary BH configurations. *Class. Quantum Grav.*, 28(14):145027–+, July 2011, 1008.2761.

[33] John L. Friedman, Kristin Schleich, and Donald M. Witt. Topological censorship[phys. rev. lett. 71, 1486 (1993)]. *Phys. Rev. Lett.*, 75:1872–1872, Aug 1995.

Part I

Binary black hole event horizon topologies

2 A Parallel Adaptive Event Horizon Finder for Numerical Relativity

Abstract

With Advanced LIGO detecting the gravitational waves emitted from a pair of merging black holes in late 2015, we have a new perspective into the strong field regime of binary black hole systems. Event horizons are the defining features of such black hole spacetimes. We introduce a new code for locating event horizons in numerical simulations based on a Delaunay triangulation on a topological sphere. The code can automatically refine arbitrary regions of the event horizon surface to find and explore features such as the hole in a toroidal event horizon, as discussed in our companion paper. We also investigate various ways of integrating the geodesic equation and find evolution equations that can be integrated efficiently with high accuracy.

Authors: Andy Bohn, Lawrence E. Kidder, Saul A. Teukolsky

Submitted to *Physical Review D*

2.1 Introduction

In late 2015, the Advanced LIGO interferometers detected the gravitational radiation from a pair of merging black holes [1]. This observation gives a unique view into the highly nonlinear regime of compact-object binary mergers, and the observed gravitational waveform

is entirely consistent with General Relativity [2]. While numerical relativity simulations help with detecting and analyzing signals that Advanced LIGO receives, they also provide a laboratory for exploring the entire compact object coalescence parameter space, including the 7-dimensional space of binary black hole (BBH) mergers. Algorithmic improvements in addition to increasing computational power over time have led to a large surge in the number of BBH simulations available to the community [3, 4, 5, 6, 7, 8].

Among the properties of the spacetime that can be studied using numerical simulations, perhaps the most interesting are those of black hole *event horizons* (EH), the boundaries of the causal past of future null infinity. The EH surface is therefore dependent on the entire future of the spacetime, making it impossible to locate during BBH simulations that progress forwards in time. A similar surface, called the *apparent horizon* (AH), is the boundary between outward directed light rays moving away from or toward the center of the black hole. In particular, the EH always contains the AH if it exists, and the surfaces are equal if the black hole has settled down to equilibrium. Locating an AH at a certain time requires only information at that time, so AHs are commonly located during BBH simulations as an EH substitute. Even though EHs are more difficult to locate, we are interested in how to find them because they define the surface of black holes, and physical properties such as the mass and angular momentum of black holes are determined by integrations over the event horizon surface [9].

We locate event horizons in BBH mergers by utilizing a theorem that the event horizon is generated by null geodesics having no future end point [10, 11, 12]. Long after the black holes have merged, the spacetime settles down to Kerr, where the EH is identical to the AH. So we can select a set of outgoing null geodesics that lie on the apparent horizon of the remnant black hole near the end of the BBH simulation [13] and integrate the geodesics backwards through time [13, 14, 15, 16, 17, 18, 19]. The convention that we will follow in this paper is to call these geodesics event horizon generators, though they are only very good approximations to the true generators [19]. Although generators of the horizon have no

future endpoint, while tracing the generators backwards in time, some may "leave" the event horizon surface where they meet other generators of the horizon. These points are called *caustics* when infinitesimally neighboring generators join together, and *crossover points* when non-neighboring generators cross paths [16, 19, 20, 21, 22]. After they leave the event horizon surface backwards in time, generators are known as *future generators* of the horizon. When viewing the event horizon forwards in time, future generators become generators of the event horizon after they join through either caustics or crossover points.

The previous generation of event horizon finding code in SpEC [18, 19] was sufficient to locate event horizons reasonably accurately, but lacked the ability to adaptively refine itself to study small scale features of the EH surface. An example of a small scale feature we are interested in exploring is a topological hole through the event horizon surface, causing the EH topology to be toroidal. The companion to this paper [23] focuses on locating such short-lived toroidal event horizons. This paper outlines the details behind our new event horizon finder, and the adaptive refinement tools that are essential to resolve a toroidal event horizon.

The organization of this paper is as follows: In Section 2.2 we give an overview of the backwards geodesic method for locating event horizons. In Section 2.3 we present the Delaunay triangulation [24, 25] on a spherical topology that we use to represent the event horizon surface, allowing for adaptive refinement. In Section 2.4 and Section 2.5, we show efficient null geodesic evolution equations and outline how we handle metric data during generator evolution. In Section 2.6, we describe the initial data calculation for event horizon generators, and in Section 2.7 we describe how we identify future generators during the backwards in time evolution.

2.2 Backwards geodesic method overview

Cohen *et al.* [18] compared three methods for locating event horizons and found the most robust method to be the backwards geodesic method. We follow this approach, where we

evolve a set of event horizon generators backwards in time to trace out the EH surface. The generators are outward null geodesics that exponentially converge to the true EH surface when traced backwards through time. As we will discuss in Section 2.3, we connect the generators together to form a polygon approximating a smooth surface with the topology of a sphere that may be self-intersecting. This surface does not approximate the event horizon only, but represents the union of the true event horizon and the locus of future generators [26].

To make the discussion concrete, consider a head-on equal mass binary black hole merger, shown in Figure 3.1. We see spatial cross-sections of apparent horizon surfaces shown blue or green, event horizon surfaces shown in orange, and the future generator surface shown in translucent purple. In panel (a), sufficiently long before the merger, the event horizon surfaces are almost identical to the blue apparent horizon surfaces, which are hardly visible at this time. The future generator surface consists of future generators that will join onto the event horizon surface in the future. When rotating this panel about the rotational axis of symmetry, the union of the event horizon surfaces and future generator surface forms a smooth topological sphere. In panel (b), shortly before the merger, the future generator surface is smaller because some of the future generators joined the event horizon between this panel and the previous panel. We can see the difference between the AH and EH surfaces increases as we get closer to the merger. There are no more future generators in panel (c) since they have all joined the event horizon surface.

In panel (d), a common apparent horizon shown in green has formed around the two interior apparent horizons, and all three apparent horizons lie entirely on or within the event horizon, as they should. As time progresses to panels (e) and (f), we stop tracking the blue inner apparent horizons, the EH settles to a stationary state, and the common AH approaches the event horizon until the two surfaces eventually coincide. With this picture in mind, the method used to locate the EH is to evolve generators backwards in time from panel (f) toward panel (a), which traces out the union of the event horizon surface with the future generator surface. Backwards in time, some generators "leave" the event horizon surface as seen in

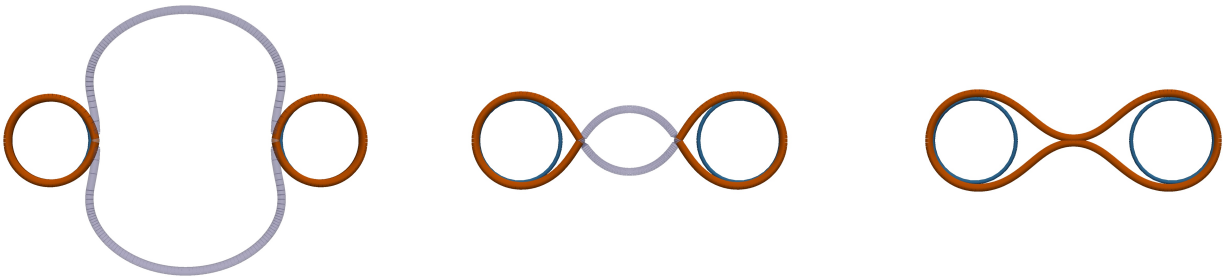

(a) $t = 414.000M$ (b) $t = 416.500M$ (c) $t = 417.500M$

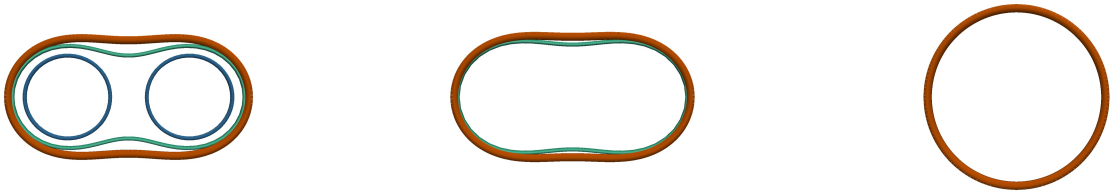

(d) $t = 420.003M$ (e) $t = 420.266M$ (f) $t = 470.639M$

Figure 2.1: Cross-sections through apparent horizons and the locus of event horizon generators for a head-on BBH merger, similar to Fig. 1 of [18]. Shown in translucent purple are future generators of the horizon that continuously merge onto the event horizon, shown in orange, until the merger in panel (c). Shown as blue curves in panels (a-d) are apparent horizons associated with the two individual black holes, and shown as a green curve in panels (d-f) is a common apparent horizon.

panels (b) and (a), so we must be able to identify which generators leave the surface and when they leave.

2.3 Event horizon representation

One of the shortcomings of our previous event horizon finder was the lack of flexibility in refining the distribution of event horizon generators in certain regions of interest. The method of distributing event horizon generators in Cohen *et al.* [18] used collocation points in a spherical harmonic ($Y_{lm}(u, v)$) expansion, with u values chosen so that $\cos u$ were the roots of the Legendre polynomial of order $L + 1$, and v values uniformly distributed in $[0, 2\pi)$, yielding $2(L + 1)^2$ generators. This results in the generators not being distributed evenly over the event horizon surface, and does not allow one to increase the resolution of a small patch of the surface.

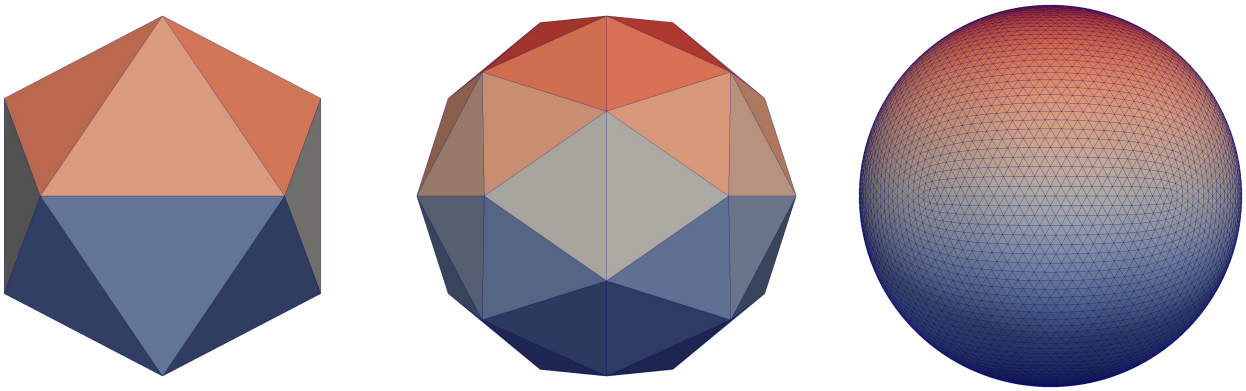

(a) Lowest resolution

(b) One iteration of uniform refinement

(c) Six iterations of uniform refinement

Figure 2.2: Varying resolutions of a triangulation over the unit sphere used during initial data generation. The lowest resolution has 12 vertices and 20 triangles evenly distributed over the sphere. One iteration of uniform refinement leads to a triangulation with 32 vertices and 60 triangles. Six iterations results in $7,292$ vertices.

We want to be able to evenly distribute event horizon generators over the event horizon as well as to be able to adaptively refine regions of the surface to sufficiently resolve the small scale features of the merger. Compared to other methods of locating event horizons [18], the backwards geodesic method allows simple adaptive refinement, in that we only need to add more generators wherever we want to refine. In addition to being able to place generators where desired, we require of our EH representation the ability to connect the generators to approximate a smooth surface.

To establish an initially evenly distributed set of generators, we begin with a regular icosahedron inscribing a unit sphere as seen in the first panel of Figure 2.2. This corresponds to our base resolution with 12 vertices and 20 triangles. The triangular faces of the icosahedron form a triangulation over the sphere, where each vertex corresponds to one generator of the event horizon. We will see later in Section 2.6 exactly how we map from this sphere to event horizon generators, but for now consider this to closely represent the distribution of generators over an event horizon.

We can reach arbitrarily high resolutions by applying the following triangle refinement procedure to each of the 20 triangles on the surface:

1. Choose a point at the median of the vertices of the triangle to be refined.

2. Move the point radially outward to the surface of the unit sphere.

3. Convert the original triangle to three smaller triangles by connecting the new point with the vertices of the original triangle.

4. Check the Delaunay condition, described below, along all exterior edges of the new triangles and perform an edge flip if necessary.

When we apply this procedure to all the triangles, we call it *uniform refinement*.

To understand the Delaunay condition and edge flips, consider four points connected to form the quadrilateral $\square ABCD$. There are two ways to form a set of two triangles from this quadrilateral, either by connecting $\overline{AC}$ to form $\triangle ABC$ and $\triangle ACD$, or connecting $\overline{BD}$ to form $\triangle ABD$ and $\triangle BCD$. The pair of triangles with the largest minimum angle among the six interior angles satisfies the Delaunay condition. An edge flip is the name for the process of converting a pair of triangles with a shared edge that fails the Delaunay condition into one that satisfies the condition. For example, we could "flip the edge" $\overline{AC}$ by removing $\overline{AC}$ and replacing it with $\overline{BD}$.

There are two choices for how to calculate the interior angles of these triangles, since the triangle vertices live on a sphere. The code can handle treating the triangles as either flat or curved along the surface of the sphere. We default to treating the triangles as curved when calculating angles, but this difference becomes less important as the triangles get sufficiently small.

One round of uniform refinement adds a vertex to each triangle, going from an icosahedron with 12 vertices to a Pentakis dodecahedron with 32 vertices shown in panel (b) of Figure 2.2. This procedure can be repeated indefinitely, but we typically uniformly refine the full triangulation six times, resulting in $7,292$ vertices evenly distributed over the surface as shown in panel (c) of Figure 2.2. In general, the n^{th} iteration of uniform refinement has

20×3^n triangles and $2 + 10 \times 3^n$ vertices[1].

While there are faster ways to generate uniform distributions of vertices over the sphere, the refinement method we use is general and can be used to adaptively refine arbitrary regions of the sphere by only refining a subset of the triangles, a procedure we call *selective refinement*. In practice, we typically do a pilot event horizon run using a uniform distribution of $7,292$ generators to determine the set of triangles we are interested in refining. Then we add generators to only those triangles in the region of interest and perform a second event horizon run. Selective refinement is crucial for studying small-scale features of the event horizon, such as the short-lived hole in a toroidal EH surface as discussed in the companion paper [23].

We have control over multiple parameters to tune the selective refinement:

- The *refinement depth* parameter roughly controls how many points are added to the selected triangles.
- The *refinement width* parameter controls how wide a region we are refining.
- We can control how many event horizon iterations we perform.

The refinement depth and width provide complete control over the refinement for the problems we are interested in, so we usually set the number of EH runs to two, corresponding to one round of refinement.

Before seeing examples of localized refinement, we must introduce the concept of a triangle *descendant*. When refining one triangle, we add a vertex and convert the triangle to three new triangles that are all labeled descendants of the original triangle. In addition, if we have to perform any edge flips, we convert two triangles into two new triangles that are both labeled descendants of the two previous triangles. We maintain a full tree-like structure of triangles that is useful for quickly locating triangles given a location on the sphere, but more importantly the tree is useful when adding more than one point to a triangle.

[1]Every iteration of uniform refinement adds one vertex per triangle in the triangulation, so we have $12 + 20 \sum_{i=1}^{n} 3^{i-1}$ vertices at the n^{th} level of refinement.

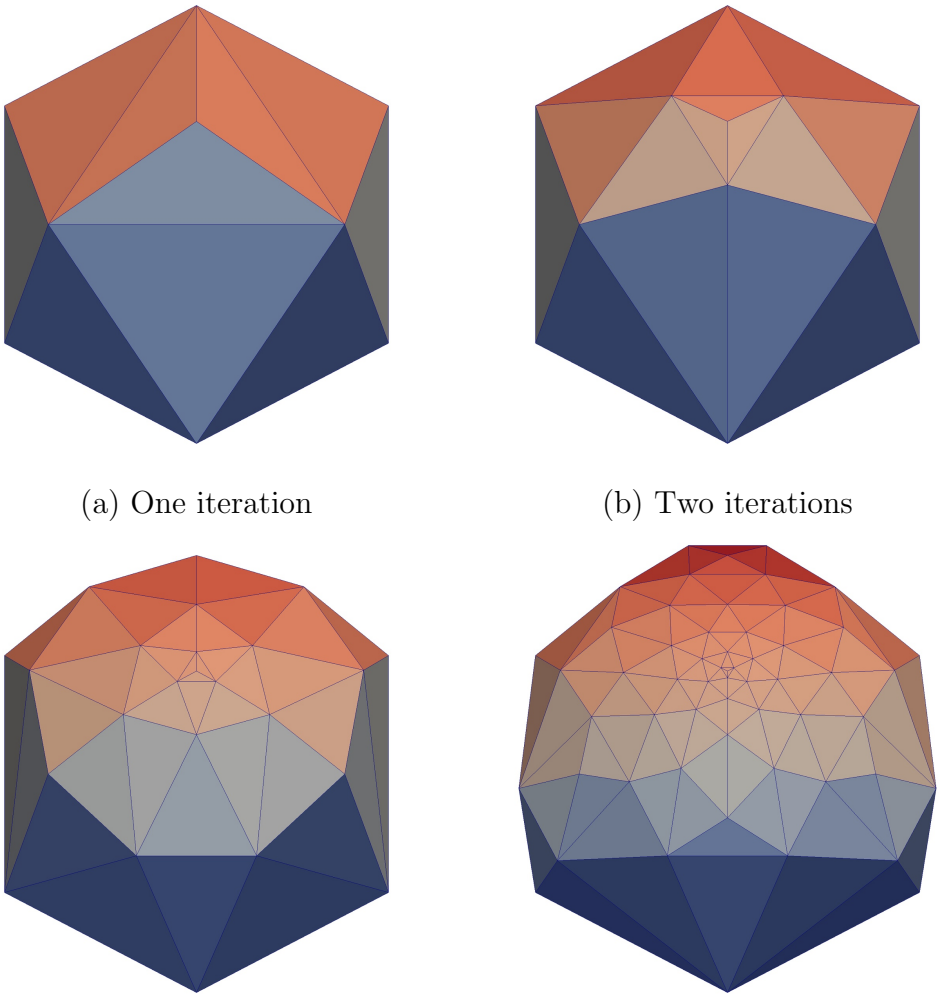

(a) One iteration

(b) Two iterations

(c) Three iterations

(d) Four iterations

Figure 2.3: Selective refinement of one triangle in the original 12 vertex triangulation shown in Figure 2.2. Panels (a)-(d) show one to four iterations of our refinement procedure applied to one triangle.

An example of selective refinement is shown in Figure 2.3, where we explore aggressive refinement of one triangle. Panel (a) shows one refinement iteration applied to one triangle, where a point is added and connected to the vertices of the triangle. The Delaunay condition is checked on all 3 edges opposite the new vertex, but in this instance, no edges needed to be flipped. In panel (b), to reach a second refinement iteration we add a point to each of the three previously created triangles, resulting in a total of 4 new points. In other words, we add a vertex to each descendant of the original triangle. Again the Delaunay condition is

checked on the edges opposing any of the new vertices, which is 6 edges in this case. We can see that all 6 edges are flipped here, giving an improved set of triangles. To perform a third refinement iteration, we must again add one vertex to each of the 12 descendant triangles of the original triangle and check for edge flips. The refinement depth is closely related to the number of refinement iterations. Our highest resolution event horizon run to date refined from $7,292$ to $246,687$ generators with this procedure, and the algorithm handles this with no problems.

Performing edge flips continually as we refine is important because we add points to the median of each triangle. If we want an even distribution of vertices, then we want each triangle to be as close to equilateral as possible, which amounts to maintaining a Delaunay condition on the sphere. These edge flips allow the density of vertices to change smoothly even though there is a large range of vertex densities over the sphere, as seen by comparing the density of vertices in panel (d) of Figure 2.3 to the original vertices in Figure 2.2. In practice, the refinement does not stray far beyond the region where we are interested in refining.

Figure 2.4 shows an example of selective refinement of an event horizon surface for a binary. The surface is the initial data surface for an event horizon simulation of a 6 to 1 mass ratio binary, with dimensionless spin $\chi \approx 0.9$ on the large BH and $\chi \approx 0.3$ on the small BH in arbitrary directions ([4] ID SXS:BBH:0165). To study the small scale features that arise where the event horizons first touch, we need to add generators to that portion of the surface. The right side of this figure shows a zoomed-in region of the event horizon surface to illustrate the transition between the low resolution and high resolution regions. Figure 2.5 shows the same simulation during the merger, where we can see the high density of event horizon generators located in the neck of the event horizon where the black holes met slightly earlier.

The density of generators is smooth and continuous between the low density and high density regions of generators. This good behavior arises partially from continually checking the

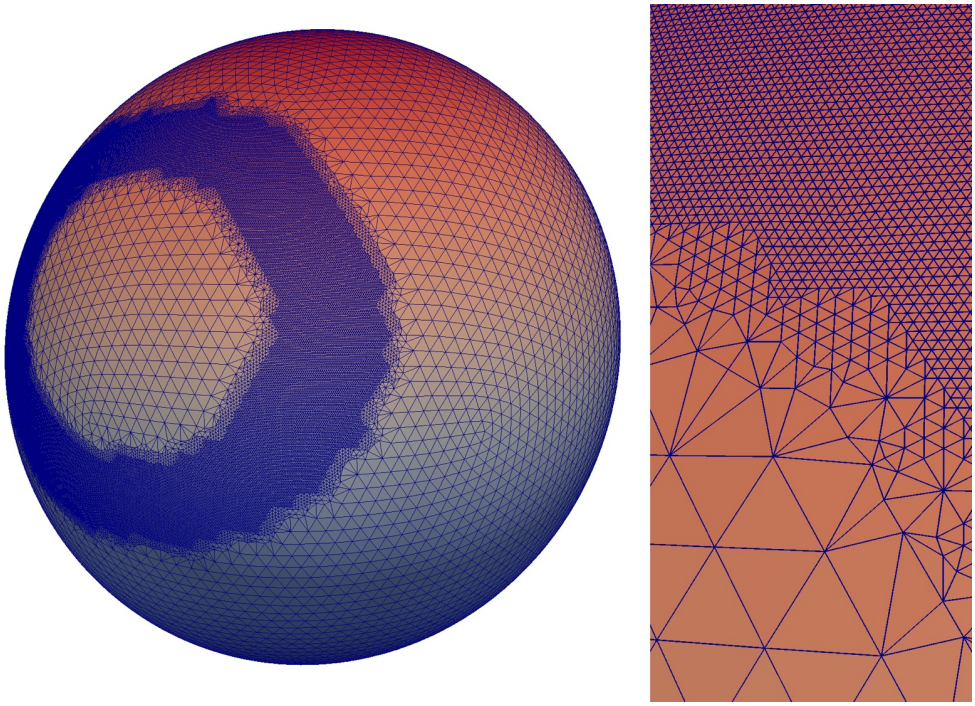

Figure 2.4: Selective refinement of event horizon generators for a BBH with mass ratio 6, refining from $7,292$ generators to $49,350$ generators. The right section of the figure shows a zoomed-in region of the left section, highlighting the smooth transition of generator density over the initial data surface. The regions where refinement occurs are chosen to be around the generators associated with the neck of the event horizon during the BBH merger, as seen in Figure 2.5.

Delaunay condition, as seen in Figure 2.3. In addition, the code sets the number of refinement iterations to smoothly transition between the low and high density regions automatically. While our selective refinement algorithm refines triangles, we determine which triangles to refine based on whether the generators at the vertices of the triangle were future generators in the past. If only one vertex of a triangle satisfies this property, then we set the number of refinement iterations to the specified refinement depth. For each additional vertex of that triangle associated with the neck region, we increment the number of refinement iterations by one. For example, if the refinement depth parameter is set to 3, as in Figure 2.4 and Figure 2.5, then we refine triangles along the border of the refinement region 3 or 4 iterations, and triangles in the interior 5 iterations.

The other tunable parameter is the refinement width, which controls how wide our

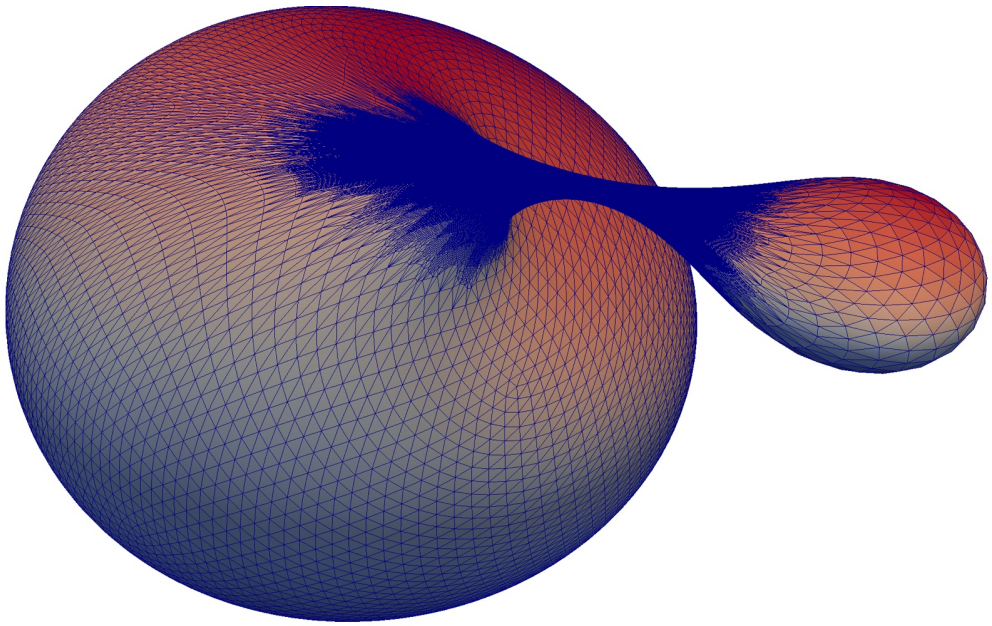

Figure 2.5: Generator locations during the merger of a 6 to 1 mass ratio binary, for which initial data is shown in Figure 2.4. Refinement occurs in the neck of the event horizon, where future generators joined the event horizon surface earlier in the merger.

refinement region is. Using Figure 3.1 as a reference, if we refined triangles associated with the future generators in panel (b) we would obtain a fairly thin refinement region, but if we refine based on the future generators in panel (a) we would widen the refinement region. Therefore we control the refinement width by choosing how long before the merger we identify triangles associated with future generators.

The parameters discussed so far refine the neck of the event horizon satisfactorily, but refine nowhere else. For high mass ratio binaries, such as the one shown in Figure 2.5, it may be worthwhile to consider refining the surface based on the curvature as well. In this case, the smaller black hole would have a large curvature compared to the number of generators in the region, and thus would have more generators added to that region. One way to accomplish this refinement is to look at the angle between the normal of a triangle and the normal of all its neighboring triangles, and add generators if the angle is too large. This type of refinement is not currently implemented since we are only interested in the neck region for this paper.

After assembling a useful distribution of generators on the EH, how do we calculate

quantities over the surface? Derivatives of scalars are calculated using first-order finite differencing, following [27] adapted to a curved surface. For some scalar f defined at the vertices of the triangulation, we can approximate the derivatives of the scalar inside the triangle using the function values at the vertices

$$\partial_\theta f \approx \left[(\phi_2 - \phi_3)f_1 + \ (\phi_3 - \phi_1)f_2 + \ (\phi_1 - \phi_2)f_3\right]/\Delta \tag{2.1a}$$

$$\partial_\phi f \approx -\left[(\theta_2 - \theta_3)f_1 + \ (\theta_3 - \theta_1)f_2 + \ (\theta_1 - \theta_2)f_3\right]/\Delta \tag{2.1b}$$

$$\Delta = (\phi_2 - \phi_3)\theta_1 + \ (\phi_3 - \phi_1)\theta_2 + \ (\phi_1 - \phi_2)\theta_3, \tag{2.1c}$$

as in equation (1) of [27], where f_i is the scalar value at the vertex with coordinates (θ_i, ϕ_i), $\partial_u f$ is the partial derivative of f with respect to u, and Δ is twice the coordinate area of the triangle. To evaluate the derivative at a vertex, we perform a weighted average of Equation (2.1a) over each triangle the vertex belongs to. The derivative of the scalar at a vertex can thus be approximated as

$$\partial_\theta f \approx \sum_{i=1}^{N} (\phi_{i+1} - \phi_{i-1})f_i/\Delta \tag{2.2a}$$

$$\partial_\phi f \approx \frac{1}{\sin\theta} \sum_{i=1}^{N} (\theta_{i+1} - \theta_{i-1})f_i/\Delta \tag{2.2b}$$

$$\Delta = \sum_{i=1}^{N} (\phi_{i+1} - \phi_{i-1})\theta_i. \tag{2.2c}$$

The derivatives in Equation (2.2a) are well-behaved far from the poles of the (θ, ϕ) coordinate system, but would require care when crossing the poles. Since our choice of vertices is evenly spread over the sphere, the vertices do not avoid the coordinate singularity at these poles. To obtain well-behaved derivatives everywhere, we set up three (θ, ϕ) coordinate systems on the sphere with the poles on the x, y, or z axis, using a cyclic permutation of the usual Cartesian to spherical coordinate transformation. The derivative at some vertex uses all neighboring vertices, so the lowest resolution triangulation our code supports must be

oriented such that each vertex and its neighbors live entirely in one of the three coordinate systems without crossing the poles. This corresponds to vertices at all cyclic permutations of $(\pm\phi, \pm 1, 0)/(\sqrt{1+\phi^2})$, where ϕ is the golden ratio, and we have normalized to 1. When computing quantities that do not depend explicitly on the choice of coordinate system on the sphere, we simply choose the coordinate system farthest from the poles, i.e. θ closest to $\pi/2$.

2.4 Generator evolution

Our code can trace event horizon generators independently through either numerical or analytic metric data, which is useful for performing code tests. It is common for numerical simulations to use the $3+1$ decomposition [28], so we express the metric in the form

$$ds^2 = -\alpha^2 dt^2 + \gamma_{ij}(dx^i + \beta^i dt)(dx^j + \beta^j dt), \tag{2.3}$$

where α is the lapse function, β^i is the shift vector, and γ_{ij} is the spatial metric.[2] We obtain numerical data from simulations performed using the Spectral Einstein Code (SpEC) [4, 29, 30, 31]. The generators are traced by evolving a solution to the geodesic equation

$$\frac{d^2 x^\tau}{d\lambda^2} + \Gamma^\tau{}_{\mu\nu} \frac{dx^\mu}{d\lambda} \frac{dx^\nu}{d\lambda} = 0, \tag{2.4}$$

where x^τ is the four-position of the geodesic, λ is an affine parameter, and $\Gamma^\tau{}_{\mu\nu}$ are the Christoffel symbols describing the effective force caused by spacetime curvature.

To facilitate the numerical geodesic evolution, we split this second-order differential equation into two first-order equations using an intermediate momentum-like variable such as $p^\tau = dx^\tau/d\lambda$. As we have some freedom in the definition of this momentum variable, we look for one that helps to minimize computational time and numerical errors when evolving through spacetimes with black holes.

[2] Our convention is that Greek indices, as in x^τ, denote temporal or spatial components, while Latin indices, as in x^i, denote only spatial components.

We initially explored using the variable $p_\tau = dx_\tau/d\lambda$ from Hughes *et al.* [15], along with converting the evolution equations from affine parameter λ to the coordinate time t of SpEC evolutions through the use of $p^0 = dt/d\lambda$. Although the resulting evolution equations are concise and have no time derivatives of metric variables, the quantities p^0 and p_i grow exponentially near black hole horizons in typical coordinate systems used by SpEC simulations. This forces our time-stepper to take prohibitively small steps in order to achieve the desired accuracy.

We therefore choose a momentum variable slightly different than p_τ to mitigate this time-stepping problem. Null geodesics satisfy $\vec{p} \cdot \vec{p} = 0$, which can be rewritten as $p^0 = \alpha^{-1}(\gamma^{ij} p_i p_j)^{1/2}$ using the metric in Equation (5.1). This expression shows that p^0 and p_i scale similarly, so we can eliminate the exponential behavior of these variables by evolving the ratio. Our intermediate variable thus becomes

$$\Pi_i \equiv \frac{p_i}{\alpha p^0} = \frac{p_i}{\sqrt{\gamma^{jk} p_j p_k}}, \tag{2.5}$$

where we also divide by α to reduce the number of terms in the resulting evolution equations. This choice of intermediate variable is the same one that appears in [32]. Using Π_i and the $3+1$ decomposition of Equation (5.1), we can express the geodesic equation in Equation (5.2) in the form

$$\frac{d\Pi_i}{dt} = -\alpha_{,i} + (\alpha_{,j}\Pi^j - \alpha K_{jk}\Pi^j\Pi^k)\Pi_i + \beta^k{}_{,i}\Pi_k - \frac{1}{2}\alpha\gamma^{jk}{}_{,i}\Pi_j\Pi_k \tag{2.6a}$$

$$\frac{dx^i}{dt} = \alpha\Pi^i - \beta^i, \tag{2.6b}$$

where K_{jk} is the extrinsic curvature (see, e.g., [28]) and Π^i is defined via the inverse spatial metric as $\Pi^i \equiv \gamma^{ij}\Pi_j$. Note that the geodesic equation consists of four second-order equations, yet we only have three pairs of coupled first-order equations in Equation (2.6). Because we are evolving a normalized momentum, Equation (5.3), we have lost information about p^0 during evolution. Compared to the evolution equations in Hughes *et al.* [15], we have

introduced a time derivative of the three-metric inside K_{jk}, but we have significantly sped up the evolution near black holes by removing the exponential growth of p^0 and p_i.

The equations in Equation (2.6) are similar to those in (28) of Vincent *et al.* [33]. In fact our intermediate evolution variable Π_i is related to their variable V^i by the three-metric, such that $\Pi^i = V^i$. But our Equation (2.6) has a reduced number of both temporal and spatial derivatives of metric quantities compared to Vincent's (28). More detailed information about splittings of the geodesic evolution equation can be found in Section 2.A.

2.5 Handling metric data

Because we perform the generator evolution through the SpEC metric data backwards in time, we must complete the binary black hole simulation beforehand while saving sufficient metric data to disk. We need all the metric components specified in Equation (2.6) at any given time and location in the evolution domain, or we need to be able to compute them. While we do not need all of the metric and its derivatives in our evolution equations, it is simpler to save $g_{\mu\nu}$ and all of the derivatives used during the SpEC BBH simulation and deal with slightly more disk space usage.

The metric and derivatives are stored on the BBH evolution grid points at a deterministic set of times such that we can interpolate the metric quantities to any spacetime point in the simulation domain. The metric $g_{\mu\nu}$ has 10 unique components when accounting for symmetry, and the derivatives $\partial_\delta g_{\mu\nu}$ have 40 components leading to a total of $50 N_{\text{pts}} N_t$ numbers, where N_{pts} is the average number of grid points and N_t is the number of time slices stored. In addition, some extra information about where the points are located and how they are distributed must also be stored.

For one fully generic BBH evolution of unequal mass black holes with arbitrary spin directions and magnitudes, the metric data can take many terrabytes of disk usage. Since typical clusters have one or two gigabytes of memory per core, we do not have nearly enough memory to read all the metric data at once. To handle this situation, we utilize a shared

memory paradigm by using OpenMP. During generator evolution, we read sections of the metric data into memory only as needed and at most once, storing it in a shared thread-safe cache. Other generators then simply access the cache to get the metric data instead of reading it from disk for themselves.

We maintain a priority queue of generators ordered by their current evolution time, such that generators that are farthest behind are given highest priority. After a pool of OpenMP threads is spawned, each thread will grab the next highest priority generator in the queue, evolve for one timestep, then insert the generator back into the priority queue. A potential concern that the CPU cache was not being utilized by taking only one timestep at a time turned out not to be valid. With the priority queue, generators are kept as close in time as possible, so that metric data in the cache is kept for as little time as needed. Since the domain structure in SpEC consists of many subdomains, only the required subdomains are read into memory. Periodically, we use the evolution time of the farthest-behind generator to determine which metric data stored in the cache is safe to be deleted[3].

When a generator requests metric data at a particular location and time, we must perform both a spatial and a temporal interpolation in general. Spatial interpolations are performed spectrally, taking advantage of the pseudo-spectral grid used during SpEC simulations. We are left with the innocent looking tasks of temporal interpolation and how to properly combine temporal and spatial interpolations. These tasks turn out to be quite complicated and are described in Section 2.B.

2.6 Initial data

We evolve a set of event horizon generators backwards in time to trace the event horizon surface, so we need to set an initial time, location, and direction for each generator. As hinted at by Figure 3.1, the apparent horizon and event horizon surfaces asymptotically

[3]Given that the farthest-behind generator is at time t, determining which metric data times are safe to delete is more complicated than just comparing the stored times against t. This is because we need to perform time interpolation, so the interpolation stencil width is also a factor.

approach each other after the merger. If we set the initial time of the backwards evolution to be late enough, the black hole will have settled to a nearly stationary solution and the apparent horizon surface could be used as initial data for the locations of the event horizon generators [13]. In SpEC, the apparent horizon is represented with a spherical harmonic decomposition, so we simply look for a time where the spherical harmonic coefficients are sufficiently stationary to choose an initial time.

Next we need to determine the positions of the generators using the triangulation over the unit sphere described in Section 2.3. We first note that each vertex of the unit sphere triangulation defines a (θ, ϕ) direction. The position of the generator associated with that vertex is then set to the intersection of the AH surface and the ray starting at the center of the AH pointing in the direction defined by the vertex. We use spectral interpolation on the spherical harmonic basis used to represent the AH to find the intersection. Since stationary black hole AHs have a nearly spherical shape when represented in typical coordinate systems used by SpEC, mapping between the reference sphere and the AH surface roughly maintains the carefully constructed distribution of vertices from Section 2.3.

Finally, we need to find the initial direction of each generator, used to calculate our intermediate evolution variable $p_i/(\alpha p^0)$ from Equation (2.6). Following [18], the initial direction of a generator should be the normal to the surface at the location of the generator, where the normal is calculated spectrally on the AH following Baumgarte *et al.* [34]. The normal direction is set to p^i, which is transformed into $p_i/(\alpha p^0)$ using the lapse and p^0 as calculated in Section 2.4.

It is important to note that refinement of the unit sphere in Section 2.3 never destroys vertices, but only destroys (and then creates) triangles. Once we trace an EH generator trajectory, we can store and reuse the trajectory after refinement without retracing the generator. Therefore we only calculate initial data for newly created vertices in the triangulation for which we need to find the trajectory. Unfortunately, while the generator trajectories from the pilot run do not need to be recalculated, determining when generators join the horizon

must be recalculated completely since the triangles have changed.

2.7 Identifying future generators

Although the event horizon surface is generated by null geodesics that never leave the horizon, event horizon generators readily join onto the horizon during the merger, as can be seen in Figure 3.1. In the backwards in time language, generators can leave the horizon where they meet other generators through one of two types of points: caustics, where neighboring generators converge to a point, or crossover points, where non-neighboring generators on the horizon meet. We must therefore identify and distinguish these caustics and crossover points.

When we trace event horizon generators, we record their locations at a predetermined set of times. In order to properly resolve the short-duration features appearing during the merger of the black holes, we need fine time resolution during the merger. However, the process of looking for caustics or crossover points scales linearly with the number of times where we record generator locations. We do not require such fine time resolution after merger where the event horizon is slowly varying and no more generators are joining, so we smoothly transition the separation between recording times from the fine resolution merger to the coarse resolution ringdown. We use a piecewise function with a hyperbolic tangent transition function to specify the spacing between recording times Δt,

$$\Delta t(t) = \begin{cases} \Delta t_{\text{coarse}} & t_{\text{coarse}} \leq t \\ \Delta t_{\text{coarse}} + (\Delta t_{\text{fine}} - \Delta t_{\text{coarse}}) \times & \\ \quad \left[0.5 \left(1 + \tanh\left\{\tan\left(\pi\left(1.5 - \dfrac{t - t_{\text{begin}}}{t_{\text{fine}} - t_{\text{coarse}}}\right)\right)\right\}\right)\right] & t_{\text{fine}} \leq t < t_{\text{coarse}} \\ \Delta t_{\text{fine}} & t < t_{\text{fine}} \ , \end{cases} \tag{2.7}$$

where Δt_{fine} and Δt_{coarse} specify the fine and coarse spacings, t_{fine} and t_{coarse} specify the boundaries for the fine and coarse spacing regions, and the transition function in square brackets varies between 0 and 1. The time range between t_{fine} and t_{coarse} is used to smoothly

transition between the different spacings, and any smooth monotonic transition function would be sufficient.

After performing the tracing, we must determine if and when generators leave the horizon backwards in time using the recorded generator locations. We search for caustics, where neighboring generators meet, by looking for generators with negative expansion parameter, similar to Cohen *et al.* [18]. The expansion of a generator is proportional to the fractional change of the area element around the generator,

$$\theta \propto \frac{1}{\sqrt{h}} \frac{\partial \sqrt{h}}{\partial t}, \tag{2.8}$$

where h is the determinant of the induced metric on the horizon at the location of the generator. Unlike Cohen *et al.* [18], where the induced metric is found using second-order finite difference stencils, it is not trivial to go beyond first-order finite differencing using our irregularly structured grid. Nevertheless, we see no evidence that the first-order derivatives are not accurate enough, since the adaptive refinement scheme discussed in Section 2.3 drastically decreases the distance between generators.

The induced metric on the event horizon is given by

$$h_{ab} = \gamma_{ij} \frac{\partial q^i}{\partial y^a} \frac{\partial q^j}{\partial y^b}, \tag{2.9}$$

where γ_{ij} is the spatial metric, q^i are the coordinates on the 3-dimensional spacetime slice, and y^a are the (θ, ϕ) coordinates on the horizon surface. The derivatives are calculated using Equation (2.2a). Since we are only interested in the fractional change in $\sqrt{\det h_{ab}}$ in Equation (2.8), we are free to perform a useful rescaling of the induced metric such that

$$\tilde{h} = \det \tilde{h}_{ab} = \frac{1}{\sin^2 \theta} \det h_{ab}. \tag{2.10}$$

For a spherically symmetric space, $\tilde{h}$ is a constant over the sphere, which provides a useful

correctness check and removes the coordinate dependence on θ.

When computing derivatives on the event horizon surface, to avoid coordinate issues around the poles of the coordinate system, we can align the poles with the x, y, or z axes by choosing the corresponding coordinate system defined in Section 2.3. We are free to change coordinate systems when calculating the expansion for different generators since we are not comparing neighboring generators, but only checking the sign of the expansion parameter.

To find the specific time t_{join} that a generator joins on the horizon, we first compute $\sqrt{\tilde{h}}$ for each generator at each stored time. Then we take the partial derivative with respect to time along each generator with a third order Lagrange interpolating polynomial and calculate the fractional change of $\sqrt{\tilde{h}}$ with respect to time, which is proportional to the expansion parameter. If this fractional change with respect to time changes sign between two recording times, we know the join time is between these times. We identify t_{join} by simply linearly interpolating the fractional change between the recording times where it changes sign to find when the expansion parameter passes through zero.

This algorithm to compute the expansion is parallelized using a set of MPI processes and a pool of OpenMP threads on each process. The set of generators on the event horizon surface is distributed evenly across the OpenMP threads and MPI processes to calculate the quantity $\sqrt{\tilde{h}}$. The next step is to take the time derivative, which is a relatively inexpensive operation, so it is currently only parallelized over the MPI processes and not over OpenMP threads.

The other way generators can join the surface is through crossover points, where non-neighboring generators meet. Since we are evolving a finite number of generators to approximate the surface, in general the generators we evolve will not cross each other. We therefore look for crossover points by checking for surface self-intersections by using a collision detection algorithm as described in [19], where every vertex is compared against every triangle to see if the generator at that vertex passed through the triangle between neighboring recording times. Our situation is simplified compared to Cohen *et al.* [19], however, because we explicitly start

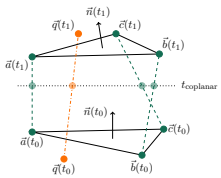

Figure 2.6: Checking for the collision of a moving triangle $\triangle abc$ and some other generator $\vec{q}(t)$ between times t_0 and t_1. The triangle is constructed by connecting three neighboring vertices $\vec{a}(t)$, $\vec{b}(t)$, and $\vec{c}t$. At some time, the four generators may become coplanar, as illustrated in the figure.

with an unchanging set of triangles as opposed to needing to define and construct a set of triangles from a (θ, ϕ) grid. Because the event horizon surface is approximated by connecting generators to form triangles, the collision of a triangle and any other generator between times t_0 and t_1 indicates that the generator joined the event horizon through a crossover at a time t_{join} satisfying $t_0 \leq t_{\text{join}} < t_1$.

The collision detection algorithm assumes each generator moves linearly through time between two neighboring times, as shown in Figure 2.6. The location of a generator $\vec{q}(t)$ is therefore a linear function between t_0 and t_1,

$$\forall t \in [t_0, t_1), \quad \vec{q}(t) = \vec{q}(t_0) + \frac{t - t_0}{t_1 - t_0} \left(\vec{q}(t_1) - \vec{q}(t_0) \right), \tag{2.11}$$

and similarly for the vertices of some triangle, $\vec{a}(t)$, $\vec{b}(t)$, and $\vec{c}(t)$. These generators and their trajectories are shown in Figure 2.6. The normal vector to the triangle $\triangle abc$ is then a quadratic function in time

$$\vec{n}(t) = \left(\vec{b}(t) - \vec{a}(t)\right) \times \left(\vec{c}(t) - \vec{a}(t)\right). \tag{2.12}$$

We first solve for all times when the generator $\vec{q}(t)$ and the triangle are coplanar by finding the roots of

$$\vec{n}(t) \cdot \left(\vec{q}(t) - \vec{a}(t)\right) = 0, \tag{2.13}$$

which is a cubic polynomial. An example of a coplanar time is shown in Figure 2.6 as the dotted horizontal line. We immediately disregard any roots of the cubic that lie outside the range $t_0 \leq t_{\text{coplanar}} < t_1$, and disregard complex roots. For every root t_{coplanar} remaining, we check whether $\vec{q}(t_{\text{coplanar}})$ lies inside triangle $\triangle abc$. If so, we mark the time at which the generator joins the horizon as this time, $t_{\text{join}} = t_{\text{coplanar}}$. It is possible that multiple roots of the cubic lie both in the desired time range and inside the triangle, but generators physically cannot cross after they join the horizon [35], so we choose the latest of the t_{coplanar} roots to be the join time.

We apply the collision detection algorithm for every pair of neighboring times where we have recorded generator location data, comparing each triangle to every other vertex. Since all generators of the event horizon are on the event horizon surface at late times, we start with the latest pair of neighboring times and work backwards. Since we are only interested in self-intersections of the actual event horizon surface, we must remove vertices and triangles from the algorithm after they leave the EH backwards in time. Once we find a join time t_{join} for a generator, either corresponding to joining as a caustic or a crossover, we do not need to check for collisions with that generator and other triangles as we move to earlier pairs of times where $t_0 < t_1 < t_{\text{join}}$. Choosing when to remove a triangle from the algorithm is more subtle, since triangles are formed from three EH generators. We only remove a triangle from

the algorithm once all three generators forming the triangle have left the EH surface, a choice that is described in Section 2.C.

This includes both when the generator would be used to form a triangle as well as when the generator would be the single vertex. If both the caustic and crossover point algorithms determine that $t_a \leq t_{\text{join}} \leq t_b$ for some pair of neighboring times t_a and t_b, then the later time must be the true join time, to satisfy the property that generators do not meet after they join the event horizon.

The search for crossovers is the most costly part of the event horizon simulation, since it is the only part of the simulation that scales quadratically with the number of generators. We have optimized the cost of each individual check for a collision between a vertex and a triangle to $\mathcal{O}(2\,\mu\text{s})$. In addition, for each pair of neighboring times, we use an OpenMP thread pool to parallelize over the triangles, and we parallelize all the remaining vertices over the MPI processes.

2.8 Conclusions

In this paper, we have presented a new event horizon finding code, with adaptive localized refinement, based on a Delaunay triangulation on a surface with the topology of a sphere. We now have the ability to refine arbitrary portions of the event horizon surface to discover and study small-scale features such as the hole in a toroidal event horizon, as discussed in our companion paper [23]. The triangulation is covered by three overlapping coordinate systems to avoid issues with coordinate singularities at the poles of the standard polar coordinate system. Using the backwards geodesic event horizon finding algorithm, we specify how to calculate initial data for event horizon generators and how to use the triangulation when searching for future generators of the event horizon.

There are several ways this event horizon finding code can be further improved. The refinement algorithm currently creates an even distribution of event horizon generators at late times in the BBH simulation, where the horizon looks like Kerr. Unfortunately, when

traced backwards in time, the event horizon surface becomes significantly stretched and distorted, leading the triangles and the distribution of generators to be similarly stretched. Since we are interested in studying the event horizon at the time of merger, we would like the generators to be evenly spaced at the time of merger. An improvement to the refinement algorithm would be to first perform an event horizon run using an even distribution of generators to determine how the triangles are stretched near merger, then use the stretch information to add new generators to the initial data surface so that the triangles are initially stretched in the orthogonal direction, but become unstretched near the merger into almost equilateral triangles. It is not obvious to us how to generate such a distribution. We note that it is difficult to re-triangulate the event horizon surface at every time step, because the re-triangulation procedure would need to understand that the surface is stretched, or else it would "cut corners" off the strongly distorted EH shape.

Furthermore, the collision detection algorithm, the slowest step in the EH locating process, is naively $\mathcal{O}(N^2)$ in the number of EH generators. One could improve the coefficient of this algorithm by dividing the space into spatial bins, with a quadtree for example, and ignoring collisions of a triangle and generator in entirely distinct spatial bins. This was not implemented because of the complexity of determining a good splitting of the surface and the problem of handling triangles or vertices that move between different regions.

Appendix

2.A Null geodesic evolution equations in the $3+1$ decomposition

It is common for numerical simulations to use the $3+1$ decomposition [28], so we express the metric Equation (5.1) in the form

$$g_{\mu\nu} = \begin{bmatrix} -\alpha^2 + \beta^i\beta_i & \gamma_{ij}\beta^i \\ \gamma_{ij}\beta^j & \gamma_{ij} \end{bmatrix}. \tag{2.14}$$

The inverse metric is

$$g^{\mu\nu} = \begin{bmatrix} -\dfrac{1}{\alpha^2} & \dfrac{\beta^j}{\alpha^2} \\ \dfrac{\beta^i}{\alpha^2} & \gamma^{ij} - \dfrac{\beta^i\beta^j}{\alpha^2} \end{bmatrix}. \tag{2.15}$$

The associated connection coefficients for this representation of the metric are

$$\begin{aligned}
\Gamma^0{}_{00} =& \frac{1}{\alpha}\left(\alpha_{,t} + \beta^k\alpha_{,k} - K_{ij}\beta^i\beta^j\right) \\
\Gamma^k{}_{00} =& \gamma^{kj}\left(\beta_{j,t} + \alpha\alpha_{,j} - \frac{1}{2}\left(\gamma_{mn}\beta^m\beta^n\right)_{,j}\right) - \beta^k\Gamma^0{}_{00} \\
\Gamma^0{}_{i0} =& \frac{1}{\alpha}\left(\alpha_{,i} - K_{ij}\beta^j\right) \\
\Gamma^k{}_{i0} =& -\alpha K_i{}^k + {}^{(3)}\nabla_i\beta^k - \Gamma^0{}_{i0}\beta^k \\
\Gamma^0{}_{ij} =& -\frac{1}{\alpha}K_{ij} \\
\Gamma^k{}_{ij} =& {}^{(3)}\Gamma^k{}_{ij} + \frac{K_{ij}}{\alpha}\beta^k = {}^{(3)}\Gamma^k{}_{ij} - \Gamma^0{}_{ij}\beta^k,
\end{aligned} \tag{2.16}$$

where ${}^{(3)}\nabla_i$ and ${}^{(3)}\Gamma^k{}_{ij}$ are the covariant derivative and connection coefficients associated with the spatial metric γ_{ij}, and we have used the extrinsic curvature

$$K_{ij} = \frac{1}{2\alpha}\left(-\gamma_{ij,t} + 2\gamma_{ik}\beta^k{}_{,j} + \gamma_{ij,m}\beta^m\right). \tag{2.17}$$

To numerically integrate the geodesic equation

$$\frac{d^2x^\tau}{d\lambda^2} + \Gamma^\tau{}_{\mu\nu}\frac{dx^\mu}{d\lambda}\frac{dx^\nu}{d\lambda} = 0, \tag{2.18}$$

we seek an efficient splitting into two first-order differential equations. A natural splitting arises through the use of the photon momentum

$$p^\mu = \frac{dx^\mu}{d\lambda}. \tag{2.19}$$

With this momentum variable, we have the evolution equations

$$\frac{dp^\tau}{d\lambda} = -\Gamma^\tau{}_{\mu\nu}p^\mu p^\nu \tag{2.20a}$$

$$\frac{dx^\tau}{d\lambda} = p^\tau. \tag{2.20b}$$

These can be converted to equations with respect to a coordinate time t by diving through by $p^0 = dt/d\lambda$.

Cohen *et al.* [18] use a similar form by evolving the quantity p^i/p^0 as an intermediate variable, although they define the variable p^i to be what is called p^i/p^0 here. This intermediate variable gives the evolution equations

$$\frac{d}{dt}\left(\frac{p^i}{p^0}\right) = \left(\Gamma^0{}_{\mu\nu}\frac{p^i}{p^0} - \Gamma^i{}_{\mu\nu}\right)\frac{p^\mu}{p^0}\frac{p^\nu}{p^0} \tag{2.21a}$$

$$\frac{dx^i}{dt} = \frac{p^i}{p^0}, \tag{2.21b}$$

which is a convenient intermediate variable choice as we will see shortly, but is problematic because it involves all of the connection coefficients during evolution. Additionally, the use of $\Gamma^{\mu}{}_{00}$ involves time derivatives of the lapse and shift (Equation (2.16)).

Performing the sum over all the connection coefficients is inefficient because of the number of terms being summed as well as inaccurate if the metric terms come from a numerical source versus an analytic source. There are many cancellations in the geodesic equation that can be taken advantage of with the appropriate choice of intermediate variable. Hughes et al. [15] explored using

$$p_\mu = g_{\mu\nu} p^\nu, \tag{2.22}$$

obtaining the evolution equations

$$\frac{dp_i}{d\lambda} = -\alpha\alpha_{,i}\left(p^0\right)^2 + \beta^k{}_{,i} p_k p^0 - \frac{1}{2}\gamma^{jk}{}_{,i} p_j p_k \tag{2.23a}$$

$$\frac{dx^i}{d\lambda} = \gamma^{ij} p_j - \beta^i p^0. \tag{2.23b}$$

Converting to an evolution with respect to coordinate time t gives

$$\frac{dp_i}{dt} = -\alpha\alpha_{,i} p^0 + \beta^k{}_{,i} p_k - \frac{1}{2}\gamma^{jk}{}_{,i}\frac{p_j p_k}{p^0} \tag{2.24a}$$

$$\frac{dx^i}{dt} = \gamma^{ij}\frac{p_j}{p^0} - \beta^i. \tag{2.24b}$$

These equations have considerably fewer terms than those in Equation (2.21) and also no time derivatives of metric functions. We note that although the variable p^0 is not evolved, it can be calculated by enforcing $\vec{p}\cdot\vec{p} = 0$, giving $p^0 = \sqrt{\gamma^{ij} p_i p_j}/\alpha$.

Unfortunately, these equations are poorly suited for evolving outgoing null geodesics near black hole horizons in the coordinate systems we are interested in, as $p^0 \sim e^t$ for an event horizon generator of a Schwarzschild spacetime expressed in Kerr-Schild coordinates for example. Other components of the 4-momentum have similar exponential dependence, leading to increasingly small timesteps. The evolution equations in Equation (2.21) conveniently

cancel the exponential behavior by evolving the ratio p^i / p^0. Can we get the best of both worlds, avoiding the exponential behavior of Equation (2.24) and avoiding the large number of terms in Equation (2.21)?

One attempt is to evolve the lower momentum normalized by p^0 as in

$$P_i \equiv \frac{p_i}{p^0}. \tag{2.25}$$

With the definition $P^i = \gamma^{ij} P_j$, this yields the evolution equations

$$\frac{dP_i}{dt} = -\alpha\alpha_{,i} + \beta^k{}_{,i} P_k - \frac{1}{2}\gamma^{jk}{}_{,i} P_j P_k + \frac{P_i}{\alpha}\left(-\alpha_{,j}\beta^j + 2\alpha_{,j}P^j + \dot{\alpha} - K_{jk}P^j P^k\right) \tag{2.26a}$$

$$\frac{dx^i}{dt} = P^i - \beta^i \tag{2.26b}$$

These equations certainly have more terms than Equation (2.24), but do not suffer from the issue of small timesteps.

We can reduce the number of terms involved in the equations further by including an extra factor of the lapse, such that

$$\Pi_i \equiv \frac{p_i}{\alpha p^0} = \frac{P_i}{\alpha} = \frac{p_i}{\sqrt{\gamma^{jk} p_j p_k}}. \tag{2.27}$$

Similarly, we define $\Pi^i = \gamma^{ij}\Pi_j$. The resulting evolution equations are those mentioned in the main text, which we repeat here for completeness

$$\frac{d\Pi_i}{dt} = -\alpha_{,i} + \left(\alpha_{,j}\Pi^j - \alpha K_{jk}\Pi^j\Pi^k\right)\Pi_i + \beta^k{}_{,i}\Pi_k - \frac{1}{2}\alpha\gamma^{jk}{}_{,i}\Pi_j\Pi_k \tag{2.28a}$$

$$\frac{dx^i}{dt} = \alpha\Pi^i - \beta^i. \tag{2.28b}$$

By using the variable Π_i, we have reduced further the number of terms involved, eliminated time derivatives of the metric, as well as removed the small timestep behavior. Since we are evolving a normalized momentum, we have lost the ability to calculate p^0. If p^0 is necessary

it can be evolved separately, but for outgoing geodesics near black hole horizons $p^0 \sim e^t$. For such geodesics, we recommend evolving the quantity $\ln(\alpha p^0)$, giving

$$\frac{d\ln(\alpha p^0)}{dt} = -\alpha_{,i}\Pi^i + \alpha K_{ij}\Pi^i\Pi^j. \tag{2.29}$$

An alternative is to simply evolve $\ln(p^0)$, which has more terms. For geodesics evolved far from black hole horizons, p^0 can be evolved directly by noting $d\ln(p^0)/dt = (1/p^0)\ (dp^0/dt)$.

The evolution equations using Π_i are similar to those in Equation (28) of Vincent *et al.* [33]. In fact, the intermediate evolution variable Π_i is related to their variable V^i by the three-metric, such that $\Pi^i = V^i$. But our Equation (2.6) has a reduced number of both temporal and spatial derivatives of metric quantities compared to Vincent's Eq. (28).

2.B Spacetime interpolations

Each component of the metric is handled independently, so it is sufficient to consider the interpolation of a scalar A defined on a set of points split into separate subdomains and on a set of time slices. This is complicated by the fact that SpEC utilizes a dual-frame system [31, 36], where computations are performed in a reference frame called the grid frame. In the grid frame, the black holes are stationary with respect to the collocation points of the evolution, and a time-dependent mapping is maintained between this frame and the asymptotically inertial frame, which we call the inertial frame.

In the inertial frame, the grid points on which the scalar A is defined are moving with respect to time, as seen in Figure 2.B.1. As a consequence, the domain boundary that is stationary in the grid frame is also moving with time. Suppose we are interested in the value of A at the $\times$, located at $(x^i_{\rm I}, t)$ where $x^i_{\rm I}$ is the spatial location in the inertial frame, and we want to use 6 time slices to perform a $5^{\rm th}$ order time interpolation. If we choose to perform a spatial interpolation on each of the 6 time slices first, then perform a temporal interpolation to the time t, then we have two choices for how to spatially interpolate.

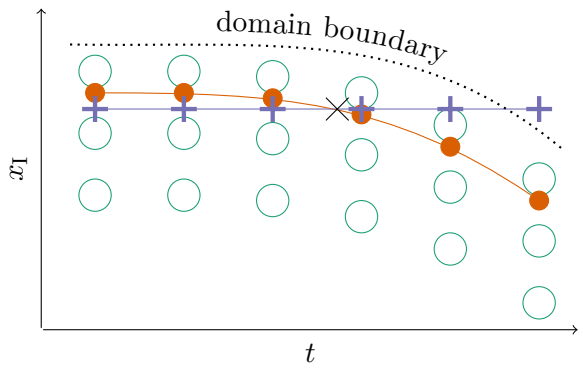

Figure 2.B.1: Spacetime interpolation to the black $\times$, as viewed in the inertial frame of SpEC. The green circles represent the grid points of the BBH simulation at the times where metric data was stored to disk. The dotted line corresponds to the domain boundary of the simulation. If we first perform a set of spatial interpolations, then interpolate the results in time, we have two choices for how to handle these interpolations. One choice is to interpolate to a constant location in the grid frame shown in orange, or a constant location in the inertial frame shown in purple. The grid frame interpolation is advantageous for multiple reasons.

The first choice, shown with pluses and a line in purple, is to spatially interpolate to $x^i_{\rm I}$ on each time slice, then interpolate in time. This method has two major drawbacks. The scalar A is, by construction, usually varying slower in time when viewed at a constant grid point $x^i_{\rm G}$ compared to a constant inertial point $x^i_{\rm I}$. The result is less accurate temporal interpolations along $x^i_{\rm I}$ which leads to decreased time step sizes. In addition, spatially interpolating to a constant point in the inertial frame could lead to attempting to spatially interpolate outside of the domain, as seen on the last time slice on the right side of the figure. Therefore, the preferred option is to interpolate to a constant grid frame point on each time slice, then interpolate in time, as shown with filled dots and a line in orange.

It is instructive to view this interpolation in the grid frame, as seen in Figure 2.B.2. In this frame, the locations of the domain boundary and the grid points are stationary in time. On each time slice, we perform a spatial interpolation to the orange points at $x^i_{\rm G} = M(x^i_{\rm I}, t)$, where t is the time to which we are interpolating and M is the time dependent mapping from the inertial frame to the grid frame. In this figure, we show another possibility where we first interpolate in time along each grid point in the subdomain to the pink pluses, then perform

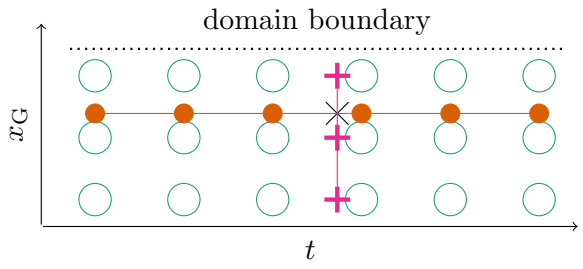

Figure 2.B.2: Spacetime interpolation to the black $\times$, as viewed in the grid frame of SpEC. The setup is similar to Figure 2.B.1, but we are observing in the grid frame. We demonstrate the additional choice between performing the spatial interpolations before or after temporal interpolations. Spatial before temporal is shown in orange, and temporal before spatial is shown in pink.

a spatial interpolation. If we count the number of operations required for either method, we find that interpolating in time then space takes $\mathcal{O}(N_{\mathrm{s}}N_t^2 + N_s^2)$ operations, where N_{s} is the number of spatial points in the subdomain and N_t is the number of time slices used in the interpolation. Interpolating in space then time takes $\mathcal{O}(N_t N_{\mathrm{s}}^2 + N_t^2)$ operations, which is typically larger than the number of operations when interpolating in time first, since $N_{\mathrm{s}} > N_t$ for our case.

Unfortunately, while interpolating in time before space requires fewer operations, in practice the error in the interpolated tensors is larger, resulting in the generator timestepper taking smaller steps. We therefore default to always performing a spectral spatial interpolation on each time slice to the grid point x^i_{G}, then interpolating in time with Lagrange polynomial interpolation.

The situation becomes more complicated when adaptive mesh refinement (AMR) during the original BBH evolution alters the grid frame. In general, the evolution grid has a different number of points after an AMR regrid, and the coordinates in the grid frame are not continuous across the regrid. In Figure 2.B.3, we see two AMR regrids denoted by vertical dashed lines at times $t_{1.5}$ and $t_{2.5}$. We start in the grid frame labeled G2, where the desired interpolation location (x^i_{I}, t) lives, following the same procedure of mapping to the grid frame location $x^i_{\mathrm{G2}} = M_2(x^i_{\mathrm{I}}, t)$, where M_2 is the mapping from the inertial frame to the

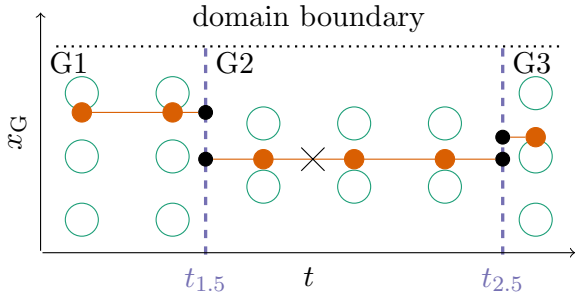

Figure 2.B.3: Spacetime interpolation to the black $\times$, as viewed in the grid frame of SpEC, showing spatial before temporal interpolation and constant grid location interpolation. The setup is similar to Figure 2.B.2, but we now have AMR. The vertical dashed purple lines correspond to AMR regrids, where the grid in general is quite different before and after the regrid. When we encounter a regrid, we must find the relationship between the regrids at the black dot locations by using the inertial frame which is continuous across regrids, as seen in Figure 2.B.4.

grid frame G2. We spatially interpolate to the grid point $x^i_{\rm G2}$ at all the times within the time interpolation stencil and in the frame G2. When a regrid occurs, we must determine how the two neighboring grid frames are related so we know to what grid location to interpolate. Specifically, we need to know what the corresponding grid frame locations in G1 and G3 are, that is, $x^i_{\rm G1}$ and $x^i_{\rm G3}$ respectively.

We make use of the inertial frame whose coordinates are continuous across the regrid to find the relationship between the grid frames. Consider the regrid at $t_{1.5}$. We map from the G2 grid frame location to the inertial frame via the G2 mapping $M_2^{-1}(x^i_{\rm G2}, t_{1.5})$, then map from the inertial frame to the G1 grid to find the corresponding grid location $x^i_{\rm G1}$. Therefore, the relationship between the grid locations is

$$x^i_{\rm G1} = M_1(M_2^{-1}(x^i_{\rm G2}, t_{1.5}), t_{1.5}). \tag{2.30}$$

This procedure is applied at every regrid in the range of times where temporal interpolation occurs. The result is a set of straight lines in the grid frame shown in Figure 2.B.3 along which we interpolate in time.

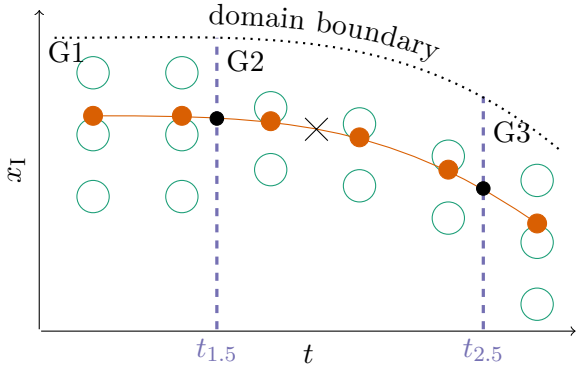

Figure 2.B.4: Spacetime interpolation to the black $\times$ as in Figure 2.B.3, but viewed in the inertial frame of SpEC. The line along which we are interpolating is continuous in the inertial frame, and the black dots on the boundary between regrids are used to find how the neighboring grid frames are related.

The corresponding inertial frame viewpoint is shown in Figure 2.B.4. Again we see that the domain boundary and grid points are in general at different locations in the inertial frame, but the line along which we are interpolating is continuous across the regrids unlike in the grid frame. The black dot at each regrid time is used as the anchor point to map between the neighboring grid frames in Equation (2.30). Specifically, the black dot along the first regrid satisfies

$$M_1^{-1}(x^i_{\mathrm{G1}}, t_{1.5}) = M_2^{-1}(x^i_{\mathrm{G2}}, t_{1.5}). \tag{2.31}$$

There is an additional complication to this procedure, albeit rare, that can occur when determining the relationship between neighboring grid frames in Equation (2.30). In Figure 2.B.5, we see part of the domain structure for a BBH simulation with parameters consistent with the Advanced LIGO event [1], specifically $m_1/m_2 = 1.25$ with dimensionless spin magnitudes $\chi_1 = 0.45$, $\chi_2 = 0.54$ in arbitrary directions. In red, we see a cutaway of the inspiral domain structure just before the domain topology changes for the ringdown, where there are two excision regions associated with individual apparent horizons of the black holes. At this time, SpEC finds a common apparent horizon encapsulating both of the inner apparent horizons, which triggers the evolution domain to change topology to

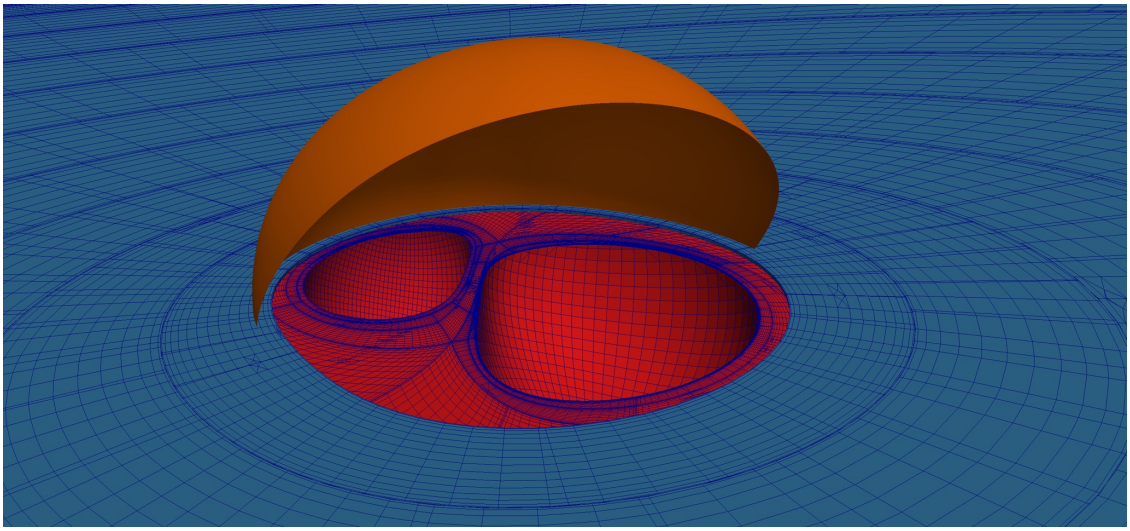

Figure 2.B.5: Portion of the event horizon surface, shown in orange, on top of the SpEC domain structure just before and after the grid change for the ringdown. In red, we see the evolution grid just before the ringdown grid change including the excision regions associated with the two inner apparent horizons. In blue, we see the evolution grid just after the ringdown grid change, with only one excision region associated with the common apparent horizon. Both the inner and common apparent horizons can be seen in panel (d) of Figure 3.1.

have just one excision region. The new domain structure after the regrid is shown in blue, so all the structure near the inner apparent horizons shown in red has been excised from the domain. Finally, in orange, we show a portion of the event horizon surface. Since the apparent horizon is never outside the event horizon, and the excision region by construction is always inside the apparent horizon, the event horizon surface always encapsulates the excision region completely.

Consider the transition between G2 to G3 in Figure 2.B.4, and assume that this transition is associated with the domain change from the red inspiral grid to the blue ringdown grid. If the point to which we want to interpolate resides in the red region after the regrid, then the point will be off the domain, causing the interpolation to fail. In SpEC, regrids can only cause grid locations to be removed from the evolution grid, not to enter the evolution grid. Therefore, we use a lopsided time interpolation stencil favoring earlier time slices to solve this issue. We first try a balanced stencil with $n/2$ times on either side of the desired interpolation point, and retry with $n/2+1$ times before the point and $n/2-1$ after if it fails,

and so forth.

While we have the ability to perform spacetime interpolations in multiple ways, the default is to interpolate first in space to a constant point in the grid frame on each time slice required for the time interpolation, then perform the time interpolation. The primary advantages to these choices are that the code handles interpolation requests accurately and without failure near domain boundaries and AMR regrids.

2.C Removing triangles from the collision detection algorithm

When tracing event horizon generators backwards through time, generators leave the EH surface when they meet other generators. These meeting points are classified as either caustics where neighboring generators meet or crossover points where non-neighboring generators meet. We detect crossover points by searching for EH surface self-intersections where in theory two generators cross, but in practice we only identify that a generator q intersected a triangle $\triangle abc$ between neighboring times t_0 and t_1 as described in Section 2.7. This collision implies there is some EH generator u (that we have not evolved) inside $\triangle abc$ that met with q between t_0 and t_1, so we flag q as leaving the horizon backwards through time.

Consider the setup in Figure 2.C.1 where we follow part of a null plane wave satisfying $t = z$ approximated by a set of generators in orange dots connected to form a set of triangles. Another null plane wave, not shown, satisfies $t = (x-y-z)/\sqrt{3}$ and is similarly approximated by a set of generators. On small scales, these two intersecting plane waves roughly approximate two intersecting portions of the EH surface. We want to search for intersections of these plane waves using only the generators of the plane waves we are evolving. We know analytically that the intersection of these waves in the plane of Figure 2.C.1 satisfies $t = (x-y)/(1+\sqrt{3})$ and so travels in the $(+x, -y)$ direction forwards in time (and travels faster than the speed of light). After the two waves intersect, the future generators shaded with blue-green will join the event horizon. At this particular time, a generator of the plane wave not shown in

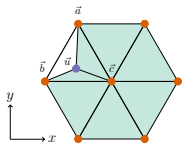

Figure 2.C.1: A portion of a null plane wave, with normal out of the page, approximated by a set of null generators shown as orange dots. This null plane wave and another null plane wave, not shown, connect to form a toy event horizon used to study the collision detection algorithm. The shaded blue-green triangles are filled with future generators of this toy event horizon, where a hypothetical generator of the EH shown as a purple dot, u, has just converted from a future generator to a true generator at this time.

this figure, q, intersects $\triangle abc$ at the location u, so a generator at u would join the horizon at this instant along with q.

As was done in Section 2.7, the algorithm is to follow both plane waves backwards through time to search for intersections where generators leave the surface. We need to identify for each generator we keep track of, shown as an orange dot, when the generator leaves the horizon. One way to handle the fact that the generator q intersected a hypothetical generator at u is to actually create a new generator at u and keep track of it. As shown in Figure 2.C.1, we would then classify $\triangle acu$ and $\triangle ucb$ as being filled with future generators, and $\triangle aub$ would still be part of the EH surface. We should therefore remove $\triangle acu$ and $\triangle ucb$ from

the collision detection algorithm, and leave $\triangle aub$ in the algorithm, because we only want to detect collisions between generators that are both on the EH.

This method would give a correct algorithm, but introduces some additional complications, so we seek a simpler algorithm. Without adding a generator, is it better to continue to include $\triangle abc$ in the algorithm or remove it from the algorithm? Both choices have some potential failure modes we need to consider. If we continue to include the triangle in the collision detection, then the potential failure mode occurs when some generator w intersects either $\triangle acu$ or $\triangle ucb$, and we proceed to incorrectly flag w as having left the EH backwards in time. The generator w should still be considered part of the EH surface because we only care about surface self-intersections between two generators that are both on the EH. However, in this setup of two colliding plane waves, there will never be such a generator w that is falsely flagged, because the plane wave to which w belongs has already passed by the triangles $\triangle acu$ and $\triangle ucb$. Therefore, including the full triangle $\triangle abc$ in the collision detection algorithm introduces no failure modes that are possible if the EH is sufficiently covered with generators.

The other option is to remove $\triangle abc$ from the algorithm. The potential failure mode here occurs when a generator w should have intersected some generator in $\triangle aub$ causing it to leave the horizon, but we incorrectly label w as still being a part of the EH surface. This failure mode can and does occur in both this toy model example and in realistic BBH event horizon simulations. Therefore, removing the triangle from the collision detection yields incorrect results, where some generators are falsely flagged as being on the EH.

To summarize, the method we use is to keep $\triangle abc$ in the collision detection algorithm until the entire triangle is filled with future generators, or equivalently when all three generators a, b, and c are all flagged as future generators of the EH. If all three generators that form the triangle are future generators, the triangle must be removed from the algorithm. This is because the approximation of two intersecting plane waves breaks down on large or long timescales, so it is possible for the triangle of future generators to wrap back toward the EH as we trace it backwards through time. If the triangle is never removed from the algorithm,

then we see some future generator triangles intersecting with generators on the EH surface, resulting in unphysical holes in the event horizon.

Bibliography

[1] B. P. Abbott et al. Observation of Gravitational Waves from a Binary Black Hole Merger. *Phys. Rev. Lett.*, 116(6):061102, 2016, 1602.03837.

[2] B. P. Abbott et al. Tests of general relativity with GW150914. 2016, 1602.03841.

[3] Larne Pekowsky, Richard O'Shaughnessy, Jim Healy, and Deirdre Shoemaker. Comparing gravitational waves from nonprecessing and precessing black hole binaries in the corotating frame. *Phys. Rev. D*, 88:024040, 2013, 1304.3176.

[4] http://www.black-holes.org/waveforms.

[5] P. Ajith, Michael Boyle, Duncan A. Brown, Bernd Brugmann, Luisa T. Buchman, et al. The NINJA-2 catalog of hybrid post-Newtonian/numerical-relativity waveforms for non-precessing black-hole binaries. *Class. Quantum Grav.*, 29(12):124001, 2012.

[6] Yosef Zlochower and Carlos O. Lousto. Modeling the remnant mass, spin, and recoil from unequal-mass, precessing black-hole binaries: The intermediate mass ratio regime. *Phys. Rev. D*, 92:024022, Jul 2015.

[7] Bernd Brügmann, José A. González, Mark Hannam, Sascha Husa, Ulrich Sperhake, and Wolfgang Tichy. Calibration of moving puncture simulations. *Phys. Rev. D*, 77(2):024027, 2008, gr-qc/0610128.

[8] Karan Jani, James Healy, James A. Clark, Lionel London, Pablo Laguna, and Deirdre Shoemaker. Georgia Tech Catalog of Gravitational Waveforms. 2016, 1605.03204.

[9] E. Poisson. *A Relativist's Toolkit: The Mathematics of Black-Hole Mechanics*. Cambridge University Press, 2004.

[10] R. Penrose. Structure of space–time. *pp 121-235 of Battelle Rencontres. DeWitt, Cecile M. (ed.). New York W. A. Benjamin, Inc.*, Jan 1968.

[11] Steven W. Hawking and G. F. R. Ellis. *The Large Scale Structure of Space-time*. Cambridge University Press, Cambridge, England, 1973.

[12] Robert M. Wald. *General Relativity*. University of Chicago Press, Chicago, IL, 1984.

[13] Peter Anninos, David Bernstein, Steven Brandt, Joseph Libson, Joan Massó, Edward Seidel, Larry Smarr, Wai-Mo Suen, and Paul Walker. Dynamics of apparent and event horizons. *Phys. Rev. Lett.*, 74:630–633, Jan 1995.

[14] Stuart L. Shapiro and Saul A. Teukolsky. Gravitational collapse to neutron stars and black holes: Computer generation of spherical spacetimes. *Astrophys. J.*, 235:199–215, 1980.

[15] S. A. Hughes, C. R. Keeton, P. Walker, K. T. Walsh, S. L. Shapiro, and S. A. Teukolsky. Finding black holes in numerical spacetimes. *Phys. Rev. D*, 49:4004, 1994.

[16] S. L. Shapiro, S. A. Teukolsky, and J. Winicour. Toroidal black holes and topological censorship. *Phys. Rev. D*, 52:6982, 1995.

[17] J. Libson, J. Massó, E. Seidel, W.-M. Suen, and P. Walker. Event horizons in numerical relativity: Methods and tests. *Phys. Rev.*, D53:4335–4350, 1996.

[18] Michael Cohen, Harald P. Pfeiffer, and Mark A. Scheel. Revisiting event horizon finders. *Class. Quantum Grav.*, 26:035005, 2009, arXiv:0809.2628.

[19] Michael I. Cohen, Jeffrey D. Kaplan, and Mark A. Scheel. Toroidal horizons in binary black hole inspirals. *Phys. Rev. D*, 85:024031, 2012, 1110.1668.

[20] Masaru Siino. Topology of event horizons. *Phys. Rev. D*, 58:104016, Oct 1998.

[21] Sascha Husa and Jeffrey Winicour. The asymmetric merger of black holes. *Phys. Rev. D*, 60(8):084019, Sep 1999, gr-qc/9905039.

[22] L. Lehner, N Bishop, R. Gomez, B Szilágyi, and J Winicour. Exact solutions for the intrinsic geometry of black hole coalescence. *Phys. Rev. D*, 60:044005, 1999, 9809034.

[23] Andy Bohn, Lawrence E. Kidder, and Saul A. Teukolsky. Toroidal Horizons in Binary Black Hole Mergers. 2016.

[24] Boris Delaunay. Sur la sphère vide. a la mémoire de georges voronoï. *Bulletin de l'Académie des Sciences de l'URSS. Classe des sciences mathématiques et na*, pages 793–800, 1934.

[25] W. H. Press, S. A. Teukolsky, W. T. Vetterling, and B. P. Flannery. *Numerical Recipes: The Art of Scientific Computing (3rd Ed.)*. Cambridge University Press, New York, 2007.

[26] Kip Thorne. Suggestion to the authors of [13, 17] that the locus of all event horizon generators forms at all times a smooth and sometimes self-intersecting surface.

[27] W. C. Thacker. Irregular grid finite-difference techniques: Simulations of oscillations in shallow circular basins. *J. Phys. Oceanogr.*, 7:284–292, 1977.

[28] R. Arnowitt, S. Deser, and Charles W. Misner. The dynamics of general relativity. In L. Witten, editor, *Gravitation: An Introduction to Current Research*, pages 227–265. Wiley, New York, 1962, gr-qc/0405109.

[29] http://www.black-holes.org/SpEC.html.

[30] Béla Szilágyi, Lee Lindblom, and Mark A. Scheel. Simulations of binary black hole mergers using spectral methods. *Phys. Rev. D*, 80:124010, 2009, 0909.3557.

[31] Daniel A. Hemberger, Mark A. Scheel, Lawrence E. Kidder, Béla Szilágyi, Geoffrey Lovelace, Nicholas W. Taylor, and Saul A. Teukolsky. Dynamical excision boundaries in spectral evolutions of binary black hole spacetimes. *Class. Quantum Grav.*, 30(11):115001, 2013, 1211.6079.

[32] Andy Bohn, William Throwe, François Hébert, Katherine Henriksson, Darius Bunandar, Mark A Scheel, and Nicholas W Taylor. What does a binary black hole merger look like? *Class. Quantum Grav.*, 32(6):065002, 2015.

[33] F.H. Vincent, E. Gourgoulhon, and J. Novak. 3+1 geodesic equation and images in numerical spacetimes. *Class. Quantum Grav.*, 29(24):245005, 2012.

[34] Thomas W. Baumgarte, Gregory B. Cook, Mark A. Scheel, Stuart L. Shapiro, and Saul A. Teukolsky. Implementing an apparent-horizon finder in three dimensions. *Phys. Rev. D*, 54(8):4849–4857, Oct 1996.

[35] Charles W. Misner, Kip S. Thorne, and John Archibald Wheeler. *Gravitation.* Freeman, New York, New York, 1973.

[36] Mark A. Scheel, Harald P. Pfeiffer, Lee Lindblom, Lawrence E. Kidder, Oliver Rinne, and Saul A. Teukolsky. Solving Einstein's equations with dual coordinate frames. *Phys. Rev. D*, 74:104006, 2006.

3 Toroidal Horizons in Binary Black Hole Mergers

Abstract

We find the first binary black hole event horizon with a toroidal topology. It had been predicted that generically the event horizons of merging black holes should briefly have a toroidal topology, but such a phase has never been seen prior to this work. In all previous binary black hole simulations, in the coordinate slicing used to evolve the black holes, the topology of the event horizon transitions directly from two spheres during the inspiral to a single sphere as the black holes merge. We present a coordinate transformation to a foliation of spacelike hypersurfaces that "cut a hole" through the event horizon surface, resulting in a toroidal event horizon. A torus could potentially provide a mechanism for violating topological censorship. However, these toroidal event horizons satisfy topological censorship by construction, because we can always trivially apply the inverse coordinate transformation to remove the topological feature.

Authors: Andy Bohn, Lawrence E. Kidder, Saul A. Teukolsky

Submitted to *Physical Review D*

3.1 Introduction

It is well established that stationary black hole spacetimes contain an event horizon with a spherical topology, assuming the dominant energy condition holds [1, 2, 3]. If the black

hole is allowed to be dynamical, Gannon [4] showed that smooth black hole event horizons could have either a spherical or a toroidal topology. Topological censorship places an upper bound on the lifetime of any topological structure such as a toroidal event horizon, where the torus must collapse faster than it would take light to traverse it [5, 6, 7]. Otherwise an observer would be able to probe the topological structure of the torus by passing a light ray through the hole. Equivalently, a different foliation of the spacetime can always be chosen such that the toroidal event horizon has a spherical topology [8, 9]. Numerical simulations of the collapse of a rotating distribution of matter showed that event horizons can indeed initially form with a short-lived toroidal topology that quickly transitions to a sphere [10, 11].

The situation with merging black holes is more complicated. Siino [9] and Husa and Winicour [12] predicted that the event horizon of a generic binary black hole system should briefly exhibit a toroidal topology during the merger. However, no toroidal event horizons have been found in numerical simulations of merging black holes, where the topology has only been seen to transition from two spheres during the inspiral to a single sphere after the merger.[1] Cohen *et al.* [14] found that the spatial cross section of the event horizon during merger has spherical topology, but the horizon structure suggested that a different spacetime foliation should reveal a torus. Simulations of three black holes [15] and eight black holes in a ring [16] similarly did not exhibit a toroidal event horizon.

For the results in this paper, we locate event horizons in binary black hole (BBH) mergers by utilizing a theorem stating that the event horizon is generated by null geodesics having no future end point [1, 18, 19], meaning they will never leave the EH surface in the future. The method is based on choosing a set of outgoing null geodesics that lie on the apparent horizon of the remnant black hole at the end of the BBH simulation when the horizon is nearly stationary [20], and integrating the geodesics backwards in time [10, 11, 14, 20, 21, 22, 23].

[1] We are specifically discussing the topology of slices of the event horizon on Cauchy surfaces as opposed to the global topology of the $2+1$-dimensional event horizon hypersurface. The topology of the event horizon has only been seen initially as the disjoint union of two spheres ($\mathcal{S}^2 \sqcup \mathcal{S}^2$) that transitions to a single sphere ($\mathcal{S}^2$) through an instantaneous state called the wedge sum of two spheres ($\mathcal{S}^2 \vee \mathcal{S}^2$) [13]. We will ignore the fine distinction between a disjoint union and a wedge sum and just consider the union hereafter.

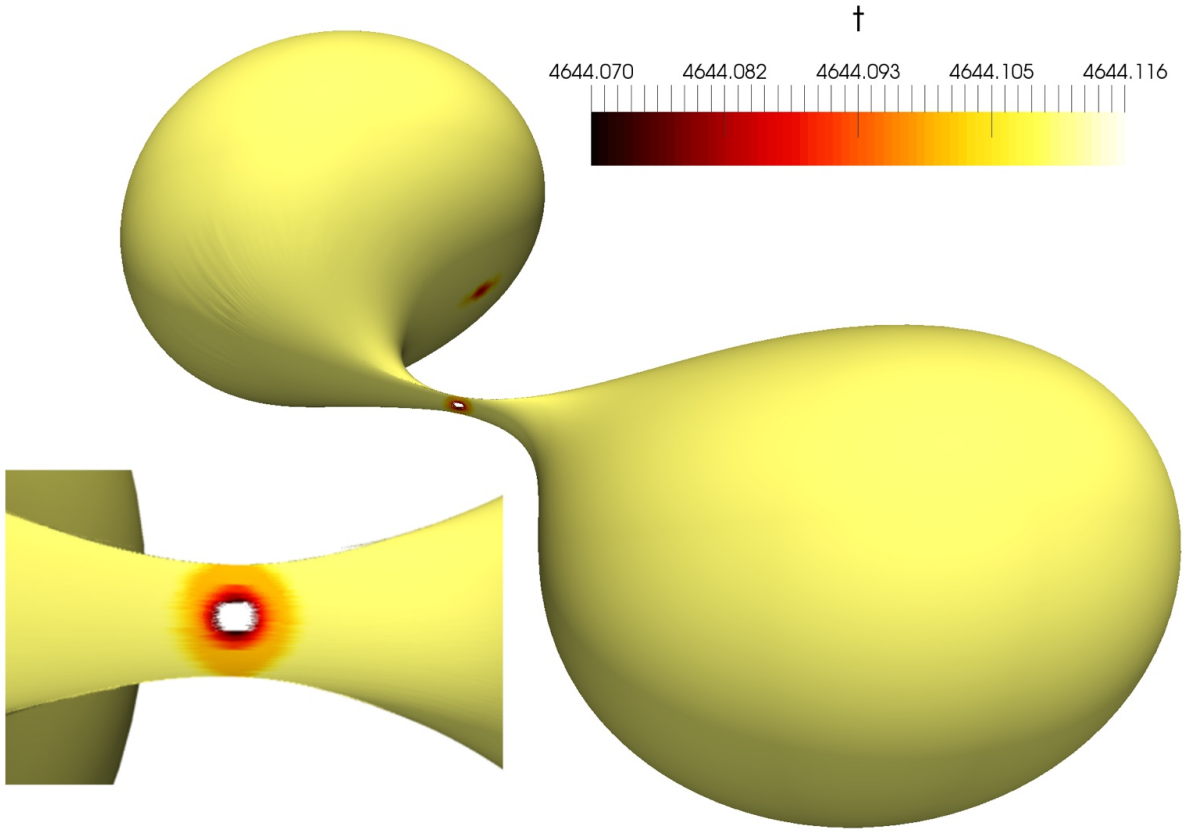

Figure 3.1: Event horizon with a toroidal topology, shown in a different time slicing than the one used in the SpEC simulation. The binary black hole simulation has a mass ratio of 1.25 and spin parameters consistent with the first BBH system Advanced LIGO detected [17]. The inset figure in the bottom left corner shows a zoomed in and slightly rotated viewpoint of the hole in the event horizon. The horizon is colored by SpEC simulation time t, which we will show in Section 3.2 should have smaller values near the hole in this slicing.

The convention that we will follow in this paper is to call these geodesics event horizon generators, although they are only very good approximations to the true generators [14]. Whereas generators of the horizon have no future endpoint, while tracing the generators backwards in time, some may "leave" the event horizon surface where they meet other generators of the horizon. These meeting points are important in the study of event horizon topologies and are called *caustics* where infinitesimally neighboring generators join together, and *crossover points* where non-neighboring generators cross paths [9, 11, 12, 14, 24]. After they leave the event horizon surface backwards in time, generators are known as *future*

generators of the horizon.

When viewing the event horizon forwards in time, future generators become generators of the event horizon after they join at either caustics or crossover points. Browdy *et al.* [25] found that the topology of the event horizon must be spherical once future event horizon generators cease joining the event horizon, which limits any potential toroidal topology to times when future generators are still joining the horizon. Therefore it is critical to accurately identify the time and location of caustics and crossover points.

In this paper, we find that the topology of the event horizon for binary black hole (BBH) systems transitions from two spheres ($2 \times \mathcal{S}^2$) to a single sphere ($\mathcal{S}^2$) in the gauge used to merge the binary with the Spectral Einstein Code (SpEC) [26, 27, 28, 29], in agreement with previous results [14]. However, the event horizon is a $2+1$-dimensional hypersurface where the topology of the event horizon depends on the foliation of the spacetime [8, 9]. When considering how future generators join the event horizon, the set of crossover points is known to live on a spacelike hypersurface that becomes asymptotically null as this hypersurface approaches a set of caustics [11]. Therefore there must exist a spacelike foliation that cuts a hole out of the spacelike surface of crossover points, resulting in a short-lived toroidal event horizon. We show explicitly that the event horizon topology can be toroidal ($\mathcal{T}^2$) in a spacelike foliation of the spacetime, as shown in Figure 3.1, by applying a coordinate transformation to the coordinate system used in SpEC to evolve the binary.

The organization of this paper is as follows: In Section 3.2 we present a coordinate transformation designed to find a new spacetime foliation where the event horizon has a toroidal topology. We begin in Section 3.3.1 by studying a toy model horizon of a spherical wavefront in flat spacetime, where there are no crossovers. In Section 3.3.2, we analyze a head-on BBH merger and find a future generator structure similar to the spherical wavefront model that prohibits the possibility of a toroidal event horizon in any spacelike foliation of the spacetime. However, in Section 3.3.3 we show a toy model horizon of an ellipsoidal[2]

[2]Here "ellipsoidal" refers to an oblate ellipsoid that is not a coordinate sphere.

wavefront in flat spacetime where the caustic and crossover distribution allows for a torodial reslicing. Utilizing what we learn with the ellipsoidal model, we are able to directly reslice an equal mass inspiral EH into a short-lived torus in Section 3.3.4. Finally, in Section 3.3.5, we show that a similar coordinate transformation of the EH can produce a "baby" event horizon that appears briefly during BBH mergers, before all three surfaces connect.

3.2 Reslicing the event horizon

The binary black hole event horizons we simulated for this work do not show a toroidal topology using the SpEC time coordinate. However, the event horizon is a $2+1$-dimensional hypersurface, and the simulation time coordinate describes only one possible spacelike foliation of the hypersurface. The generalized harmonic time slicing of our binary black hole simulations [30] may not be conducive to producing toroidal event horizons [14, 23]. We specify in this section a coordinate transformation from the coordinate system of the BBH evolution to a new coordinate system to explore the possibility of another time slicing yielding a toroidal event horizon.

In the companion [31] to this paper, we introduce a complete replacement for the previous event horizon finding code in SpEC [14, 23]. The overall method is the same as before, where we evolve a set of event horizon generators backwards in time to trace out the horizon surface. At each time, we connect the generators together to form a polygon approximating a smooth surface with the topology of a sphere that may be self-intersecting. This surface does not approximate the event horizon only, but the union of the true event horizon and the locus of the future generators [32]. The new event horizon finder is fully adaptive and so can resolve fine-scale features of the event horizon. This feature is crucial to demonstrating the existence of a toroidal topology.

To make the discussion concrete, consider a head-on equal mass binary black hole merger, shown in Figure 3.1. We see a spatial cross-section of apparent horizon surfaces shown blue or green, event horizon surfaces shown in orange, and the future generator surface shown

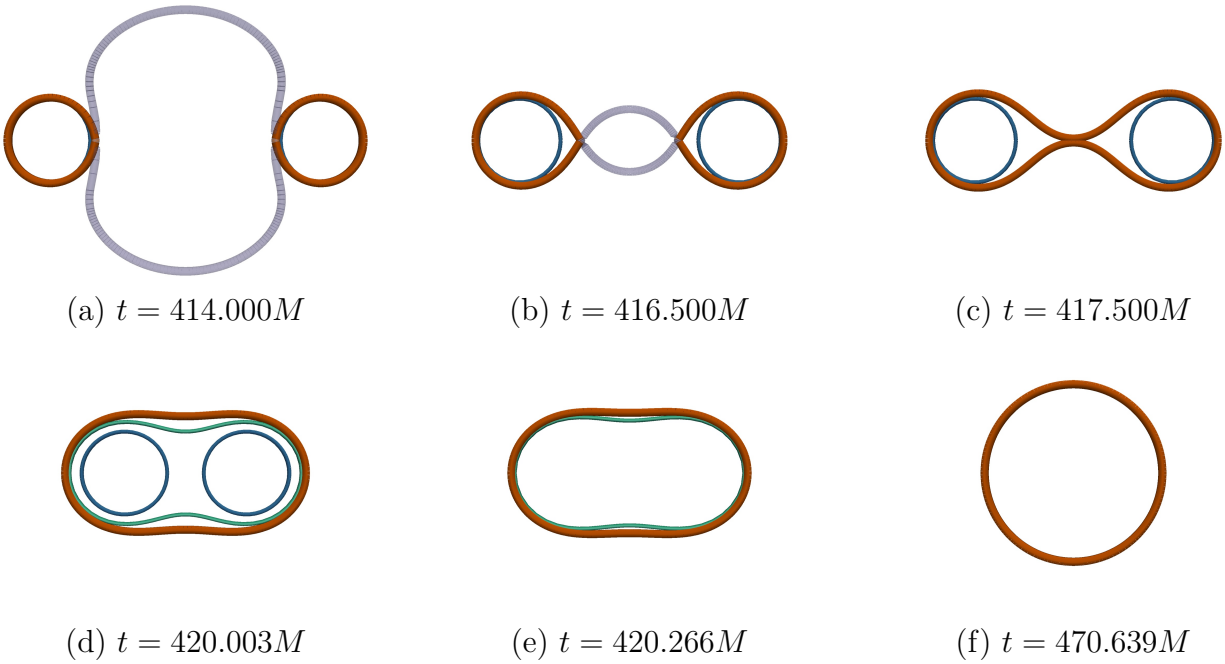

(a) $t = 414.000M$ (b) $t = 416.500M$ (c) $t = 417.500M$

(d) $t = 420.003M$ (e) $t = 420.266M$ (f) $t = 470.639M$

Figure 3.1: Cross-sections through apparent horizons and the locus of event horizon generators for a head-on BBH merger. Shown in translucent purple are future generators of the horizon that continuously merge onto the event horizon, shown in orange, until the merger in panel (c). Shown as blue curves in panels (a-d) are apparent horizons associated with the two individual black holes, and shown as a green curve in panels (d-f) is a common apparent horizon.

in translucent purple. In panel (a), sufficiently long before the merger, the event horizon surfaces lie almost on top of the blue apparent horizon surfaces, which are hardly visible at this time. The future generator surface is comprised of future generators that will join onto the event horizon surface in the future. When rotating this panel about the rotational axis of symmetry, the union of the event horizon surfaces and future generator surface forms a smooth $\mathcal{S}^2$. In panel (b), shortly before the merger, the future generator surface is shrinking because some of the future generators have joined the event horizon between this time and the time of the previous panel. We can see the difference between the AH and EH surfaces increases as we get closer to the merger. There are no more future generators in panel (c) since they have all joined the event horizon surface, and therefore the event horizon surface must be $\mathcal{S}^2$ [25].

In panel (d), a common apparent horizon shown in green has formed around the two

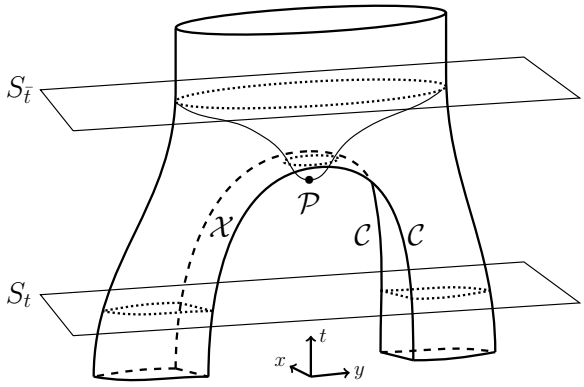

Figure 3.2: A $2+1$-dimensional "pair of pants" representation of slices of constant time S_t and $S_{\bar{t}}$ through a BBH event horizon. The hypersurface S_t is a slice of constant t when the event horizon topology is two spheres, such as panel (a) or panel (b) of Figure 3.1. $\mathcal{X}$ represents the spatial hypersurface of crossover points, which is surrounded on both sides by lines of caustics denoted by $\mathcal{C}$. The event horizon is toroidal on the spatial hypersurface $S_{\bar{t}}$, a slice of constant $\bar{t}$; the center of the hole in the torus is $\mathcal{P}$.

interior apparent horizons, and all three apparent horizons lie entirely on or within the event horizon, as they should. As time progresses to panels (e) and (f), we stop tracking the blue inner apparent horizons, the event horizon settles to a stationary state, and the common apparent horizon in green approaches the event horizon until the two surfaces eventually coincide. With this picture in mind, the method is to evolve generators backwards in time from panel (f) toward panel (a) which traces out the union of the event horizon surface with the future generator surface. Backwards in time, some generators "leave" the event horizon surface as seen in panels (b) and (a), so we must be able to identify which generators leave the surface and when they leave.

One of the shortcomings of our previous event horizon finder was the lack of flexibility to refine the distribution of event horizon generators in certain regions of interest. In the companion paper, we present a new method of distributing and maintaining a set of event horizon generators to address these issues. In particular, we now have the ability to study in much greater detail the region where future generators join the event horizon surface.

In Figure 3.2, we show a $2+1$ dimensional representation of a BBH event horizon through

merger. The slice S_t is a constant t slice through the event horizon at a time when the topology is two spheres, similar to panels (a) and (b) of Figure 3.1. At this time, event horizon generators are joining the event horizon through, in general, both crossover points and caustics. Connecting the crossover points together forms a spacelike hypersurface denoted as $\mathcal{X}$, and connecting the caustic points forms spacelike hypersurfaces denoted as $\mathcal{C}$ that form the boundary of the crossover region. Considering slices of constant t in this example, the event horizon topology is never toroidal. However, a different spacelike slice $S_{\bar{t}}$ could dip through $\mathcal{X}$ to form a toroidal event horizon with $\mathcal{P}$ a point in the middle of the hole. In essence, we are looking for a slice where generators in the crossover region are delayed near merger, similar to $S_{\bar{t}}$.

To accomplish this delay, we use a coordinate transformation of the form

$$\bar{x}^i = x^i \tag{3.1a}$$

$$\bar{t} = t + G(x^j, t), \tag{3.1b}$$

where $\bar{t}$ and $\bar{x}^i$ are the coordinates after the transformation and $G(x^j, t)$ is some smooth function of position and time. Equivalently, $t = \bar{t} - G(x^j, t)$, such that a slice of constant $\bar{t}$ is associated with a smaller t value where $G(x^j, t)$ is larger. Therefore, the value of $G(x^j, t)$ controls how delayed generators at (x^j, t) are in the constant $\bar{t}$ slicing. An example of an event horizon on a constant $\bar{t}$ slice is shown in Figure 3.1, where the surface is colored by the associated t value and generators near the hole in the event horizon correspond to earlier t values.

The transformation has the Jacobian matrix

$$\mathbf{J} = \frac{\partial(\bar{t}, \bar{x}^i)}{\partial(t, x^j)} = \begin{bmatrix} 1 + \partial_t G & \partial_j G \\ 0 & \delta^i{}_j \end{bmatrix}. \tag{3.2}$$

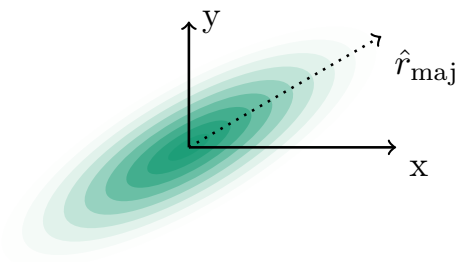

Figure 3.3: Representation of two spatial dimensions of the Gaussian function $G(t, x^j)$ from Equation (3.1b), where darker colored regions represent larger values of $G(t, x^j)$. $\hat{r}_{\mathrm{maj}}$ is an input parameter that specifies the major axis direction of the Gaussian. All directions in the plane perpendicular to $\hat{r}_{\mathrm{maj}}$ are treated equally.

The normal to surfaces of constant $\bar{t}$ is given by

$$\bar{n}_\mu = -\bar{\alpha}\nabla_\mu \bar{t}, \tag{3.3}$$

where $\bar{\alpha}$ is the lapse in the barred coordinates. We can solve for $\bar{\alpha}$ from the normalization of the normal, $\vec{n} \cdot \vec{n} = -1$, giving

$$\bar{\alpha}^2 = \frac{\alpha^2}{\left(1 + \partial_t G - \beta^k \partial_k G\right)^2 - \alpha^2 \gamma^{ij} (\partial_i G)(\partial_j G)}, \tag{3.4}$$

where β^k is the shift vector and γ^{ij} is the three metric. The denominator of Equation (3.4) must be greater than zero to obtain a foliation of the spacetime with spacelike hypersurfaces, since we know α^2 is greater than zero.

For the function $G(t, x^j)$, we choose a three-dimensional ellipsoidal Gaussian, with one dimension in time, one along a specified major axis, and the other in the minor plane perpendicular to the major axis. This gives 10 free parameters to be specified: the amplitude (A), the time center and time width (t_0 and σ_t), the spatial center ($\vec{r}_0$), the major axis direction ($\hat{r}_{\mathrm{maj}}$), and the major and minor widths (σ_{maj} and σ_{min}). A two-dimensional example is shown in Figure 3.3, where the time dimension has been omitted, and the plane perpendicular to

$\hat{r}_{\rm maj}$ has been projected down into one dimension. The function $G(t, x^j)$ has the form

$$\begin{aligned} G(t, x^j) = & \\ & A \exp\left[-\left(t - t_0\right)^2 / \left(2\sigma_t^2\right)\right] \\ & \times \exp\left[-[\hat{r}_{\rm maj} \cdot (\vec{x} - \vec{r}_0)]^2 / \left(2\sigma_{\rm maj}^2\right)\right] \\ & \times \exp\left[-\left((\vec{x} - \vec{r}_0)^2 - [\hat{r}_{\rm maj} \cdot (\vec{x} - \vec{r}_0)]^2\right) / \left(2\sigma_{\rm min}^2\right)\right], \end{aligned} \tag{3.5}$$

where the first exponential localizes the Gaussian to the time of merger, the second preferentially modifies geodesics along some major axis, and the third limits the range in the plane perpendicular to the major axis. The major axis is chosen in the thinnest direction of the small neck connecting the two black holes just after merger, which we will analyze in Section 3.3.4. This choice produces time slices that cut through the spacelike crossover surface arising during the merger, as illustrated in Figures 3.1 and 3.2. After finding Gaussian parameters that yield a toroidal event horizon on at least one constant $\bar{t}$ slice, it is sufficient to verify that the new lapse is positive and real using Equation (3.4).

To reslice the event horizon in practice, we first trace a set of generators to locate the EH in the generalized harmonic coordinate system used to merge the binary in SpEC, as detailed in the companion paper [31]. During the generator evolution, we record the generator locations at a set of times that are finely spaced as the event horizons merge and coarsely spaced after the merger. Using Equation (3.1b), we then calculate $\bar{t}$ for each generator at each of these times. We want the locations of the generators on constant $\bar{t}$ slices, and we accomplish this with a $3^{\rm rd}$-order Lagrange interpolation polynomial in $\bar{t}$. The spacetime location where an EH generator joins the horizon is a spacetime event, so we simply apply the coordinate transformation to determine when the generator joins the horizon in the barred coordinate system.

3.3 Discussion

Previous studies of merging event horizons infer the possibility of a toroidal event horizon by studying the distribution of caustics and crossover points during the merger. As discussed in Section 3.2, the set of crossover points is known to live on a spacelike hypersurface that becomes asymptotically null as the surface approaches a set of caustics [11]. There should therefore exist a spacelike foliation of the spacetime that cuts a hole out of the spacelike surface of crossover points, resulting in a short-lived toroidal event horizon. In this section, we are interested in explicitly finding such a reslicing where the event horizon has a toroidal topology.

It is useful to first study null hypersurfaces in flat space, where the distribution of caustics and crossover points is known analytically. We will use these wavefronts as model horizons and refer to them as "horizons" for convenience in the spherical model in Section 3.3.1 and in the ellipsoidal model in Section 3.3.3. These models were introduced in Shapiro *et al.* [11] and also studied in Siino [8].

All of the systems in this discussion section can be found on the SXS collaboration website [33] at the page [**?**].

3.3.1 Spherical model

We trace generators for a spherical wavefront backwards in time through the Minkowski spacetime until all the generators leave the horizon through a caustic or a crossover point. These points are identified using the same algorithms as used for binary black hole event horizons, described in the methods paper [31]. The initial data for this model horizon is a sphere of radius 1 at $t = 0$, shown in Figure 3.1, where the z-axis is an axis of rotation. Generators are placed on the sphere pointing perpendicular to the surface outward and evolved backwards in time through flat space, where the black dashed arrows denote some generators of the horizon and the dotted teal lines show the corresponding generator trajectories. The

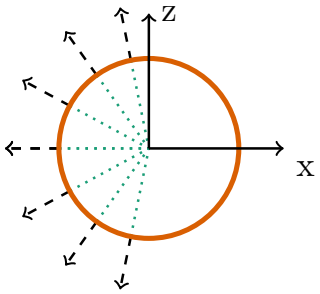

Figure 3.1: Initial data configuration for the spherical model horizon in flat space. The orange circle, when rotated about the z-axis, forms the sphere used as initial data for the generator tracing. Along this surface, we place null geodesics normal to the surface as described in the companion paper [31], illustrated as black dashed arrows. The green dashed lines show where the generators came from earlier in coordinate time, and that the trajectories all met at the origin at the same time in the past.

generators begin the simulation on the surface and we search for caustics or crossover points to determine if and when generators leave the horizon backwards in time.

Because of the symmetry of the system, all future generators must join onto the horizon at the same location and time through a caustic, since all the generators meet together at the origin. The code properly labels all of the generators as joining through caustics and we do not find a surface of crossover points, as expected. The lack of a crossover surface makes this model illustrative for the head-on merger of equal mass black holes as featured in the following section.

Since there is no crossover surface, which would form a spacelike hypersurface, we should not expect to be able to find a slicing of the spacetime that yields a toroidal surface, so this provides a good test of our reslicing algorithm. Using the coordinate transformation in Section 3.2 with a flat metric and σ_t set large enough to keep the transformation independent of time, the new lapse from Equation (3.4) simplifies to

$$\bar{\alpha}^2 = \frac{1}{1 - \delta^{ij}(\partial_i G)(\partial_j G)}. \tag{3.6}$$

We must therefore keep the spatial gradients of $G(x^j, t)$ small to maintain a spacelike foliation.

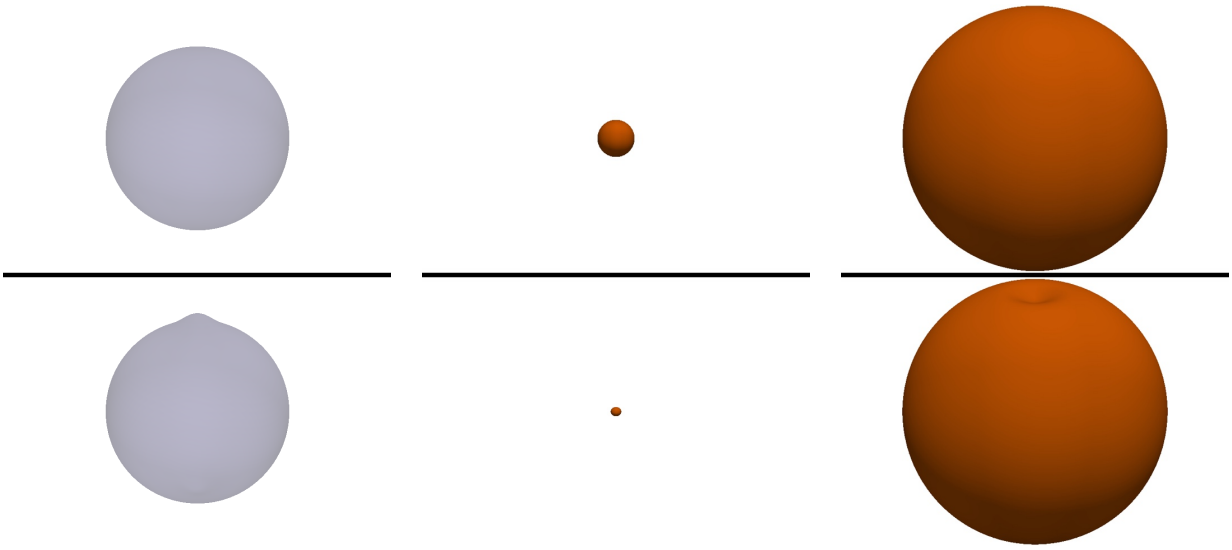

(a) $-1.351M$ (b) $-0.935M$ (c) $-0.550M$

Figure 3.2: Generator surface for the spherical horizon model in Section 3.3.1, shown in two different coordinate systems. The top row shows a slice of constant t coordinate, which is the original coordinate system of the spherical model, and the bottom row shows a slice of constant $\bar{t}$ coordinate after using the transformation in Equation (3.1b). Regions of the surface colored in translucent purple denote areas of future generators that are not currently part of the horizon surface, and orange denotes areas where generators are on the horizon surface. M is the unit of time in this coordinate system, where the speed of light is 1.

However, we know that any coordinate transformation will preserve events. In particular, the caustic event where all the generators meet at the origin of the coordinate system will be preserved, meaning all the generators will join the horizon at the same time in all foliations of the spacetime.

Figure 3.2 shows this surface in two foliations of the spacetime, where the top row shows the original slicing with spherical initial data, and the bottom row shows the resliced horizon. It is important to reiterate that we will show horizons going forwards in time from left to right, but the generator evolution is performed backwards in time from right to left in these figures. Therefore, the initial data for the spherical model is in the top row of the rightmost panel. The bottom row is an attempt at a coordinate transformation into a new slicing of the spacetime to look for a torus.

Going along the top row from left to right, all the generators are initially future generators

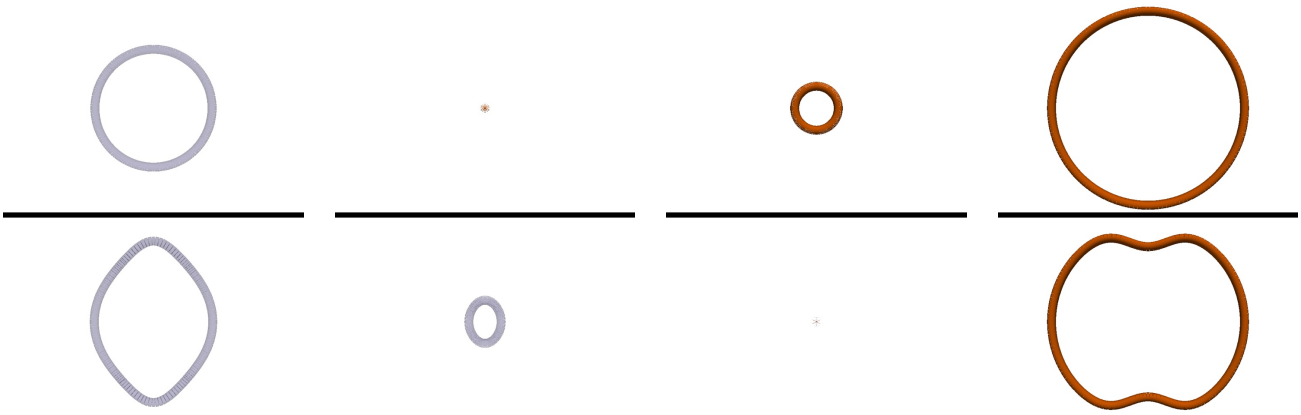

(a) $-1.065M$ (b) $-0.999M$ (c) $-0.952M$ (d) $-0.873M$

Figure 3.3: Zoomed in slices of the spherical horizon in flat space, covering a small duration of time near panel (b) in Figure 3.2. The full surface is generated by rotating these slices around the vertical direction of the figure. The color scheme and coordinate systems are the same as in Figure 3.2.

of the horizon, as indicated by the translucent purple color. As coordinate time progresses forward, all the generators meet together at a single point in time just before panel (b), where they join the surface through a caustic at the origin. The surface continues to expand linearly through panel (c) until reaching the unit sphere.

The bottom row paints a very similar picture, where we have applied the coordinate transformation in Equation (3.1b) to search for a toroidal topology. We tried a variety of parameters with similar results, but show the values from Case A of Table 3.1 for these figures. Just as in the original slicing, all the generators join at the same time through a caustic just before panel (b). The coordinate transformation changes the shape of the horizon, but leaves the topology unaffected.

It is instructive to simplify horizons by taking a slice through the surface. In Figure 3.3, we take a slice through the spherical model horizon along the major axis of the Gaussian coordinate transformation, such that a rotation of the slice produces the full surface in both coordinate systems. To analyze exactly how generators join the horizon, we have magnified the spatial and temporal scales relative to Figure 3.2. Note that the rows show slices of constant time in different coordinate systems, so we do not expect events such as the joining

Case	A	$\vec{r}_0$	t_0	σ_t	$\hat{r}_{\text{maj}}$	σ_{maj}	σ_{min}
A	$5 \times 10^{-2} M$	$\vec{0}$	0	∞	$\hat{z}$	$1M$	$5 \times 10^{-2} M$
B	$3 \times 10^{-2} M$	$\vec{0}$	$417.424M$	$1M$	$\hat{z}$	$1M$	$2 \times 10^{-2} M$
C	$5 \times 10^{-2} M$	$\vec{0}$	$7540.018M$	$3M$	$\frac{\sqrt{2}}{2}(-\hat{x} + \hat{y})$	$1M$	$2 \times 10^{-2} M$

Table 3.1: Sets of parameters supplied to the Gaussian coordinate transformation in Equation (3.1b), used in different circumstances throughout this paper. The unit M is the unit of the corresponding coordinate system, where it is the total mass of the black holes for BBH simulations.

of generators onto the horizon to align. In the top row, the generators join the horizon in panel (b) simultaneously at a single point, and similarly for the bottom row in panel (c).

Though the surfaces appear different in the two coordinate systems, we see clearly that the caustic event is preserved under coordinate transformation. Therefore the horizon of this model instantaneously transitions from not existing to having a spherical topology independent of the slicing as expected.

3.3.2 Equal mass head-on merger

The simplest binary black hole merger to study is the head-on merger of equal mass non-spinning black holes. The system we consider has black holes initially at rest centered at $\pm 25 M\hat{y}$, where M is the total mass of the black holes. This binary has rotational symmetry about the y-axis connecting the two black holes as well as a mirror symmetry about the xz-plane halfway between the black holes. The expectation for the topology of this event horizon is two spheres before the merger that transition to a single sphere, with no toroidal phase in any slicing of the spacetime [12, 24, 34].

Straightforward symmetry arguments show that the event horizon topology must be composed of only spheres, as we now show. In this system, the resultant black hole after the merger settles down to a static Schwarzschild horizon since there is no angular momentum in the system about the origin. The initial data for the event horizon simulation is therefore a spherically symmetric surface. Consider the event horizon generators at the intersection

between the EH and the $y = 0$ mirror plane, forming a ring. The generators on this ring should initially look exactly like those in the spherical model shown in Figure 3.1. These generators must remain in this plane for the entire simulation owing to the mirror symmetry. Furthermore, the spacetime is axisymmetric about the y-axis, and so the generators must respect this symmetry and remain in a circle in this coordinate system. We can see from these symmetries that the generators in the mirror plane must all join simultaneously through a caustic at the origin, identical to the spherical model horizon in Section 3.3.1. When considering planes where $y \neq 0$, the rotational symmetry still enforces that the intersection of the plane and the event horizon always remains circular, where all the generators in a circle similarly join the EH through a caustic along the y-axis. We can parameterize all the future generators into rings by where along the y-axis they join the EH. In any coordinate system, the generators in a given ring are either all future generators at a given time or all true generators of the EH. Because generators never cross after joining the EH surface, it is therefore impossible for a torus to form in any coordinate slicing of the head-on merger. Changing the number of $\mathcal{S}^2$ EH surfaces is however possible with certain coordinate transformations that change the relative times when neighboring rings join the EH, as we will see in Section 3.3.5.

Another way to state the argument is based on the lack of a crossover surface. The $2 + 1$-dimensional event horizon hypersurface is null everywhere except for where future generators join the EH through caustics or crossover points, where it is spacelike. Using coordinate transformations, we can only cut a hole through the event horizon hypersurface where it is spacelike, along the inseam of the pair of pants in Figure 3.2. We already argued that there are only caustics (and so no crossover points) in the coordinate system where the BBH system is axisymmetric, and that coordinate transformations preserve these caustics. The inseam of the pair of pants is thus 1-dimensional and composed of only caustics, and the rest of the event horizon hypersurface is null, therefore there is no 2-dimensional spacelike hypersurface through which to cut a hole in the EH.

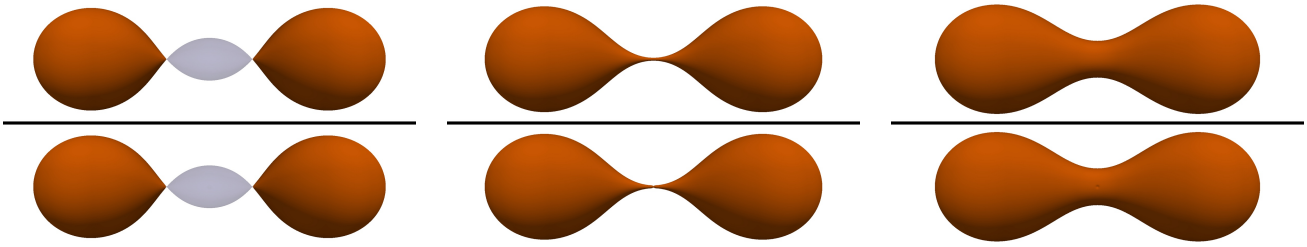

(a) 416.800M (b) 417.460M (c) 418.000M

Figure 3.4: Event horizon generator surfaces for the equal mass head-on binary. The t slicing in the top row is almost identical to the $\bar{t}$ slicing in the bottom row, because of the small size of the Gaussian parameters relative to the horizon scale.

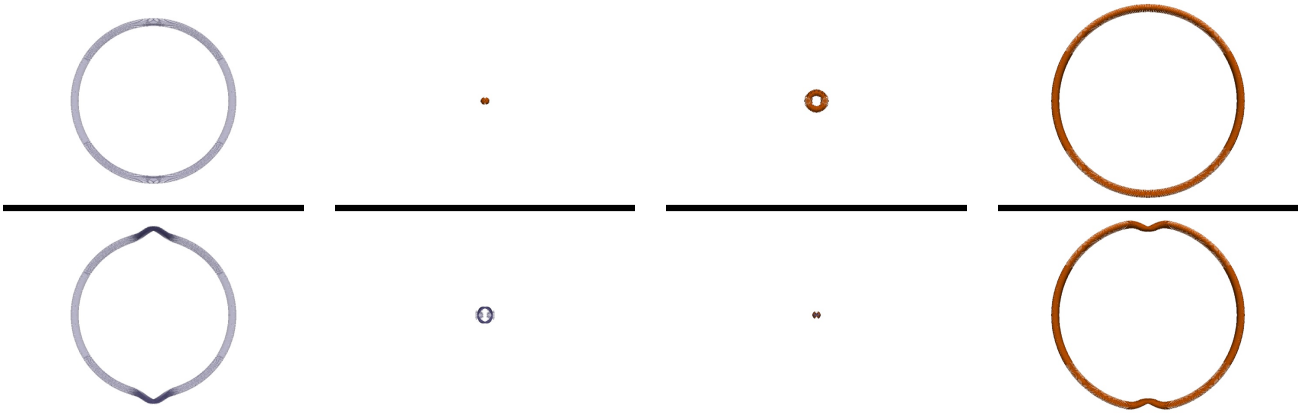

(a) 417.160M (b) 417.433M (c) 417.460M (d) 417.773M

Figure 3.5: Slices in the mirror symmetry plane of Figure 3.4, near the time the EHs merge. The generators join the EH simultaneously through a caustic in both coordinate systems.

Figure 3.4 shows the event horizon surface before, during, and after the black hole merger. The parameters of the coordinate transformation are labeled Case B in Table 3.1. The event horizon in these two coordinate systems looks virtually indistinguishable because the spatial scale of the coordinate transformation is small compared to the scale of the figure. Topologically, both coordinate systems are identical. We have one spherical surface for each event horizon ($2 \times \mathcal{S}^2$) in panel (a). After all the future generators join the EH, the horizon transitions into a single $\mathcal{S}^2$ shown in panel (b) and remains that way.

Figure 3.5 shows spatial slices through the mirror symmetry plane. The top row shows the event horizon in the slicing used for the SpEC BBH spacetime evolution and the bottom row the transformed slicing. These slices look similar to slices of the spherical model shown

in Figure 3.3, where the t coordinate slice in the top row remains a circle and generators on the circle join the horizon simultaneously through a caustic.

Just as in the spherical model, we cannot alter the relative timing of when the generators join the horizon in this slice, since these generators meet at a single event in spacetime, and coordinate transformations preserve events. We perform a reslicing anyway to illustrate the point and to test our code. In the bottom row of Figure 3.5, we see small scale deformations along the top and bottom of the ring. Because of the coordinate transformation in Equation (3.1b), generators in regions where $G(x^i, t)$ is relatively large are delayed in the $\bar{t}$ slicing, causing the small bumps in panels (a) and (d). The caustic event where generators join the horizon occurs in panel (c), showing that the caustic is preserved by the coordinate transformation. No hole in this event horizon could possibly exist because of the lack of a crossover surface.

Independent of the slicing of the spacetime, the head-on binary starts as a set of spheres and transitions to a single sphere. These results are consistent with the findings in [12, 24, 34], as well as the spherical model in Section 3.3.1. The highest resolution of the SpEC BBH evolution was used for these figures, but the topological structure is the same in all three resolution levels of the SpEC evolution.

3.3.3 Ellipsoidal model

The prediction of Siino [9] and Husa and Winicour [12] is that toroidal event horizons should appear in generic BBH mergers, where there is no axis of symmetry. We analyze in this section an ellipsoidal wavefront, identical to the oblate spheroid model in [8, 11], that provides a more generic caustic and crossover distribution than the spherical wavefront model in Section 3.3.1. The appearance of both caustics and crossovers makes this model illustrative for generic BBH mergers, such as the equal mass inspiral featured in the following section.

The initial data for the generator evolution is similar to the spherical model, but we place

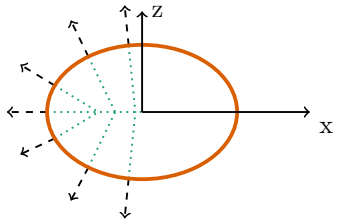

Figure 3.6: Initial data configuration for the ellipsoidal model horizon in flat space. Similar to Figure 3.1, but the initial data surface is an ellipsoid rather than a sphere. The green dashed lines show where the generators came from earlier in coordinate time, and that the trajectories met at different locations in the past.

generators normal to the ellipsoid

$$\frac{x^2 + y^2}{2} + z^2 = 1, \tag{3.7}$$

shown in Figure 3.6. Figure 3.7 shows this ellipsoidal horizon on a few time slices using the same color scheme and layout as Figure 3.2. In agreement with Shapiro *et al.* [11], the first generators to join the horizon join at the origin through crossover points in the top row of panel (c). The horizon is smooth everywhere, apart from a one-dimensional ring around the outside of the horizon where generators continue to join through crossover points. If we connect these crossover events to form a surface, we obtain a two-dimensional spacelike hypersurface in the equatorial plane (the xy-plane). Much later, the last future generators join the horizon along the outside ring in the equatorial plane, forming a one-dimensional ring of caustic events. This slicing therefore shows only a spherical topology.

The bottom row of Figure 3.7 shows the horizon after the coordinate transformation in Equation (3.1b) with parameters identical to those used in the spherical model (case A of Table 3.1). While applying coordinate transformations will ensure that spacetime events such as caustic or crossover points are preserved, the relative time between neighboring caustic or crossover points can be altered. This coordinate transformation is sufficient to obtain a horizon that initially appears with a toroidal topology as shown in the bottom row of panel (c). The horizon is smooth apart from two one-dimensional rings where crossover

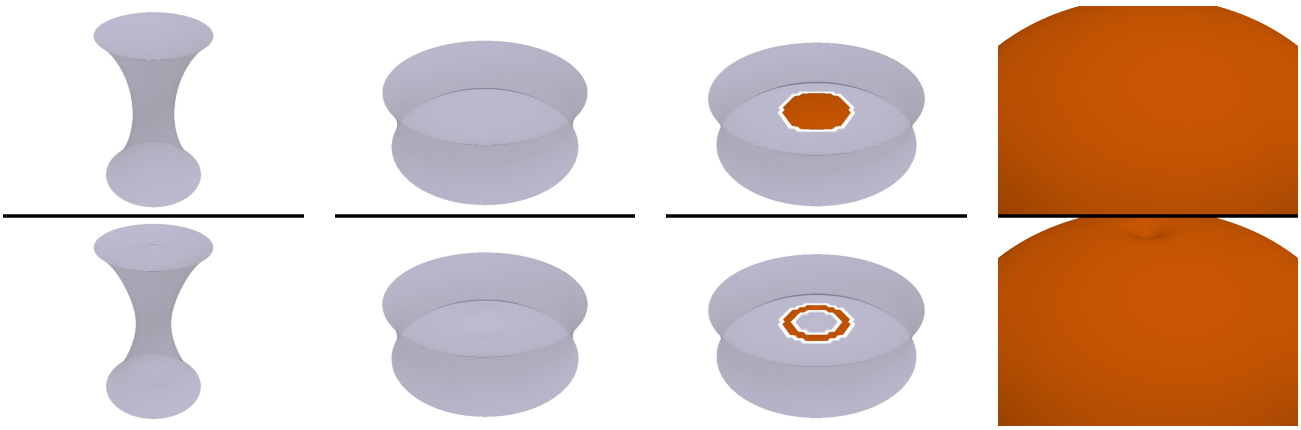

(a) $-1.307M$ (b) $-1.038M$ (c) $-0.988M$ (d) $-0.571M$

Figure 3.7: Similar to Figure 3.2, but with an ellipsoidal horizon used as initial data. The figures are zoomed in to show the small scale features that arise as generators join the horizon.

generators continue to join the surface. One ring is on the outside of the torus and the other is on the inside. Shortly after the torus forms, the hole in the horizon closes, leaving the same spherical topology as seen in the top row of panel (c).

As we did for the spherical model, in Figure 3.8 we take a slice through the horizon along the z-axis to learn why it was possible to apply a coordinate transformation and obtain a torus. The spatial and temporal scales are magnified in this figure compared to Figure 3.7 to showcase how the generators join the surface in both coordinate systems.

Panel (a) of Figure 3.8 shows a slice of future generators with a quite different shape compared to what is seen in the spherical model. In the top row of panel (b), generators begin to join the horizon through crossover points, where generators from the top half of the slice meet the bottom half. The horizon instantaneously appears as an $\mathcal{S}^2$. In the $\bar{t}$ slicing of the bottom row, the generators in the middle of the slice are delayed relative to their neighbors because of the positive Gaussian in the coordinate transformation. The delay is sufficient to cause the first generators that join the horizon to be spatially separated on the slice as seen in panel (c). After rotating about the vertical axis of symmetry, the surface initially appears with a toroidal topology. Finally, in the bottom row of panel (d), the interior region has closed to yield an $\mathcal{S}^2$ topology. We have thus found a coordinate transformation

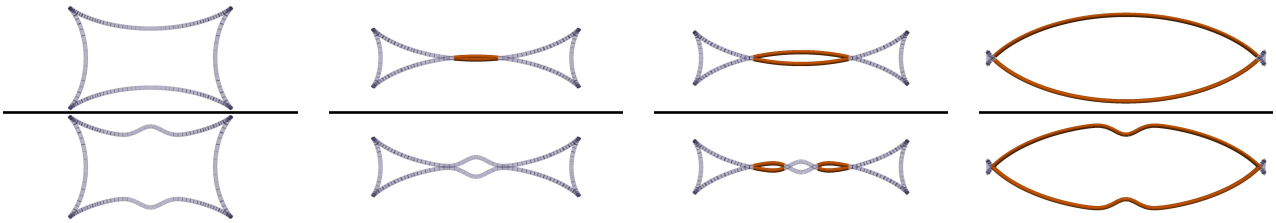

(a) $-1.131M$ (b) $-0.998M$ (c) $-0.978M$ (d) $-0.811M$

Figure 3.8: Zoomed in slices of the ellipsoidal horizon shown in Figure 3.7, covering a small duration of time near panel (c). The setup is identical to Figure 3.3.

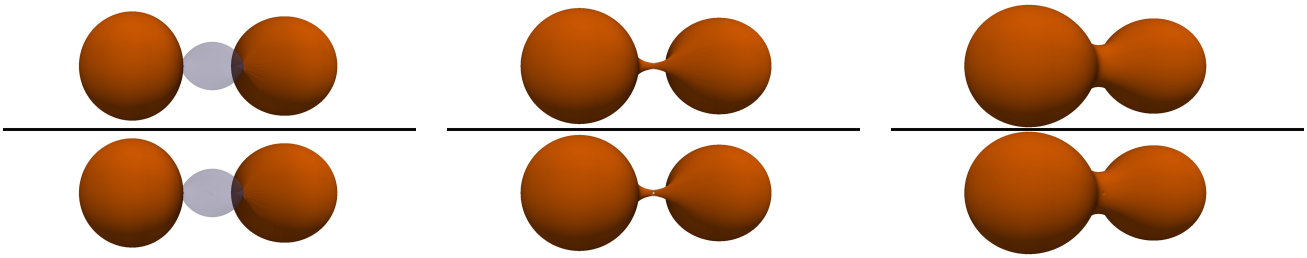

(a) $7539.011M$ (b) $7539.947M$ (c) $7540.786M$

Figure 3.9: EH generator surface for the equal mass inspiral, with the orbital angular momentum of the system pointing upward. A slice of the neck will be analyzed in more detail in Figure 3.11 and a close-up is seen in Figure 3.12.

that cuts a hole out of the spacelike crossover surface along the inseam.

3.3.4 Equal mass inspiral

The primary reason that the equal mass head-on merger did not yield a toroidal event horizon is the rotational symmetry of the system causing all the future generators to join the horizon through caustics. A binary black hole system in a quasi-circular orbit removes this rotational symmetry. We expect to see a more generic distribution of caustics and crossover points similar to the ellipsoidal model, enabling us to reslice the EH into a torus. For simplicity, we analyze a pair of non-spinning black holes, initially in a quasi-circular orbit with a separation of $17M$.

We show the event horizon surfaces in Figure 3.9, where the camera is in the orbital plane and the orbital angular momentum of the system is pointing up. The coordinate transformation uses parameters with the label Case C in Table 3.1, and the amplitude is yet

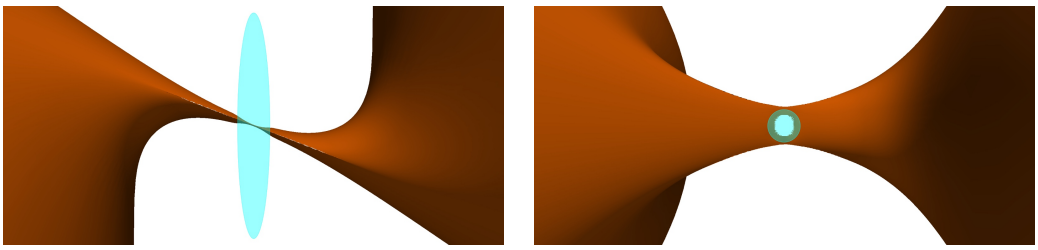

(a) $\hat{r}_{\rm maj}$ pointing upward (b) $\hat{r}_{\rm maj}$ pointing out of the page

Figure 3.10: At $\bar{t} = 7539.943M$, visualizing the Gaussian ellipse on top of the equal mass inspiral surface shown in the barred coordinate system. In panel (a), $\hat{r}_{\rm maj}$ is pointing upward and is pointing out of the page in panel (b). The minor axis width $\sigma_{\rm min}$ is on the same spatial scale as the width of the neck causing a pinching of the neck in panel (a) and causing a hole in the horizon surface to appear in panel (b).

again quite small compared to the figure size. The time and space centers, t_0 and $\vec{r}_0$, are chosen to coincide with the location where the event horizons first meet. In this BBH, the neck joining the event horizons has an elliptical shape, similar to what was seen in the slices of the ellipsoidal model horizon. We learned from the ellipsoidal model that the direction of the major axis $\hat{r}_{\rm maj}$ should be chosen roughly along the direction in which the crossover generators were traveling as they joined the horizon. The final parameter that is important to tune is the width of the Gaussian perpendicular to $\hat{r}_{\rm maj}$, $\sigma_{\rm min}$, such that it is smaller than the width of the neck connecting the horizons.

Figure 3.10 shows a cartoon illustration of this coordinate transformation overlaid on the event horizon in barred coordinate system. The camera viewpoints are chosen such that in panel (a), $\hat{r}_{\rm maj}$ is pointing up, and in panel (b), $\hat{r}_{\rm maj}$ is pointing into the page. The major axis Gaussian width $\sigma_{\rm maj}$ is not shown to scale in this figure, but the precise value of $\sigma_{\rm maj}$ has little effect on the coordinate transformation once it is sufficiently large. In panel (a) the effect of the coordinate transformation is only to pinch the neck in the $\bar{t}$ coordinate system in the region where the Gaussian is different than zero. The minor axis Gaussian width $\sigma_{\rm min}$ has most of the control over the size of the hole, where a smaller width causes a smaller (and thus harder to resolve numerically) hole. Smaller values of $\sigma_{\rm min}$ also result in sharper gradients of the function G, which can cause the new lapse in Equation (3.4) to become

imaginary. However, a minor axis width that is too large gives a shallower gradient of the function $\bar{t} = t + G(x^i, t)$, which could result in the lack of a toroidal horizon.

The torus is illuminated more clearly by taking spatial cuts through the EH surface in both coordinate systems as shown in Figure 3.11. The vertical direction in the figure is parallel to $\hat{r}_{\rm maj}$. The slices in this figure bear a remarkable resemblance to the ellipsoidal model slices in Figure 3.8, suggesting that the future generators join the horizon in a similar manner. In panel (b), the first generators to join the EH in the constant t slicing join through crossover points. We are able to delay these generators such that the first generators to join the horizon in the constant $\bar{t}$ slicing are spatially separated in the slice in panel (c). As time progresses forward, generators continue to join at the interfaces between future generators and event horizon regions in the $\bar{t}$ slicing. Finally in panel (d), the two pieces of the horizon connect after all the remaining generators in the gap join the horizon.

Figure 3.12 shows up close what the hole in the horizon looks like. The top and bottom rows are constant t and constant $\bar{t}$ slices. We are showing both the full generator surface as well as the same spatial slice as seen in panel (c) of Figure 3.11. The constant $\bar{t}$ slice shows clearly that there is a hole in the event horizon surface, so the EH has a toroidal topology. For the hole in the horizon, the EH surface pinches off along a one-dimensional non-smooth ring where event horizon generators will continue to join through crossover points. The left and right edges of the event horizon surface shown in orange are also not smooth, where generators continue to join through crossover points. The final generators to join the event horizon surface do so through caustic events, just as seen in the ellipsoidal model (Figure 3.8). This torus is seen in all three refinement levels of the SpEC BBH evolution.

The coordinate transformation used does not guarantee that constant $\bar{t}$ hypersurfaces are spacelike. We therefore must check that the new lapse $\bar{\alpha}$ is well behaved by evaluating Equation (3.4) in the region where $\bar{t}$ differs from t, that is, where $G(x^i, t)$ is non-negligible. We construct a grid of points centered about $\vec{r}_0$ and t_0 to evaluate the new lapse in the range

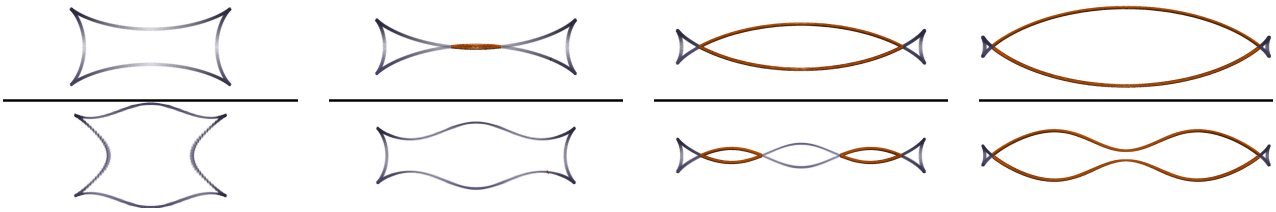

(a) 7539.891M (b) 7539.918M (c) 7539.948M (d) 7540.971M

Figure 3.11: Slices of the equal mass inspiral during the merger of Figure 3.9, where the vertical direction in the figure is parallel to $\hat{r}_{\rm maj}$, and the slice is taken through the hole in the EH. The slices have the same character as those in Figure 3.8.

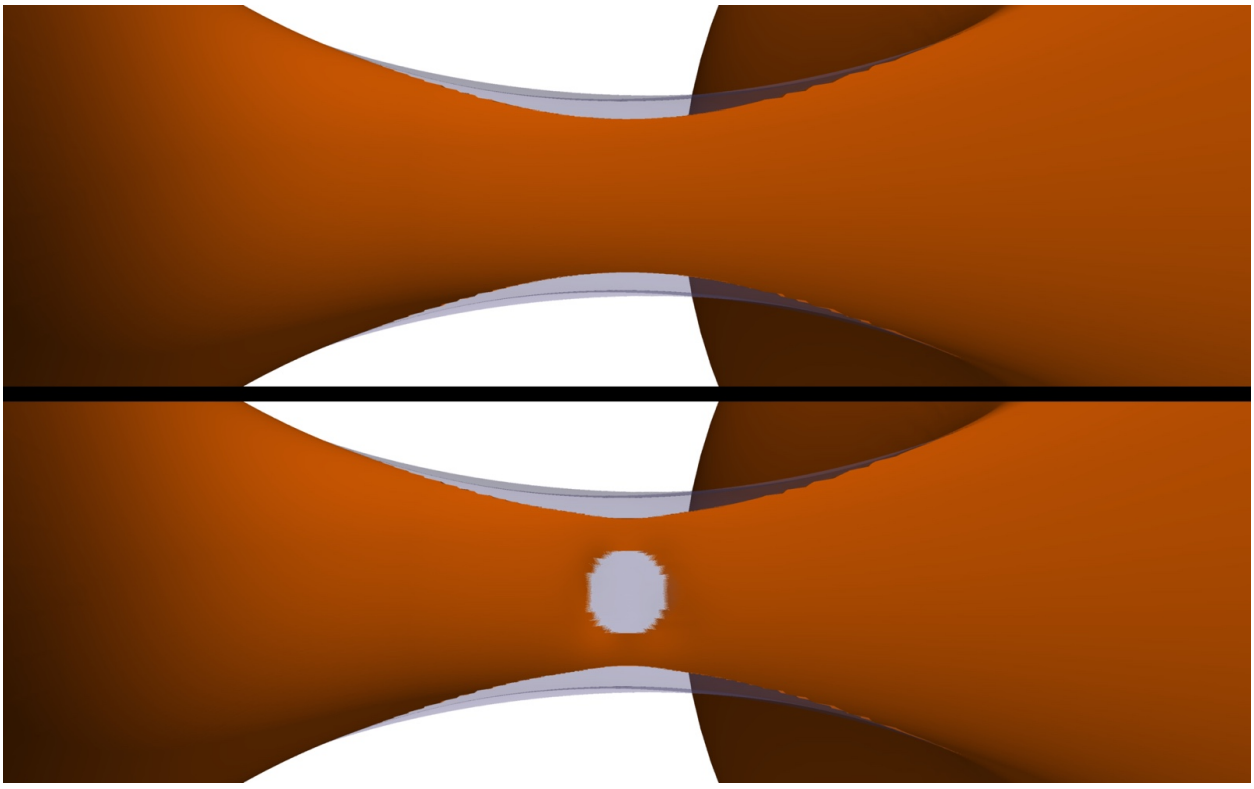

Figure 3.12: Zoomed in figure of the hole in the horizon. The full event horizon generator surface including future generators are shown at time 7539.948M corresponding to panel (c) of Figure 3.11. This toroidal event horizon and the other systems in the discussion section Section 3.3 at the webpage [**?**].

of

$$t = t_0 \pm 4\sigma_t \tag{3.8a}$$

$$\vec{x} = \vec{r_0} \pm 4\sigma_{\rm maj}\hat{r}_{\rm maj} \pm 4\sigma_{\rm min}\hat{r}_{\rm min1} \pm 4\sigma_{\rm min}\hat{r}_{\rm min2}, \tag{3.8b}$$

where $\hat{r}_{\rm min1}$ and $\hat{r}_{\rm min2}$ are unit vectors perpendicular to each other and perpendicular to $\hat{r}_{\rm maj}$. Beyond this range, the Gaussian function is vanishingly small ($G(x^i, t) < e^{-8} = \mathcal{O}(10^{-4})$) for our purposes.

We use a grid of points with $N_{\rm pts}$ points distributed in each dimension of the four-dimensional space defined by Equation (3.8b) to calculate the new lapse $\bar{\alpha}$ and check that it is real. Because the new lapse is a function of the metric in the SpEC coordinate system, we must interpolate the metric $g_{\mu\nu}$ to the location in space and time where $\bar{\alpha}$ is to be calculated. These interpolations are performed the same way as is done during the generator evolution, described in the companion paper [31].

Figure 3.13 shows the lapse squared in both the SpEC coordinate system (α^2) and in the new coordinate system ($\bar{\alpha}^2$) using a grid with 74^4 evenly distributed points over the Gaussian. At each of the 74 times, we calculate the square of the lapse on 74^3 spatial points and plot the maximum and minimum found in both coordinate systems. This plot shows that the constant $\bar{t}$ hypersurfaces are indeed spacelike, because $\bar{\alpha}^2$ is positive at all times. It should be noted that we could not check the lapse at all points on this wide grid, since some of the points live off the SpEC evolution domain because of the excision region inside the black holes; However, these locations are guaranteed to be inside the event horizon and so do not affect the event horizon. All other points in the SpEC domain and in the space defined by Equation (3.8b) contribute to Figure 3.13. The large spike in the minimum lapse squared in both coordinate systems is an expected feature from how the excision surfaces in SpEC change during the BBH merger phase.

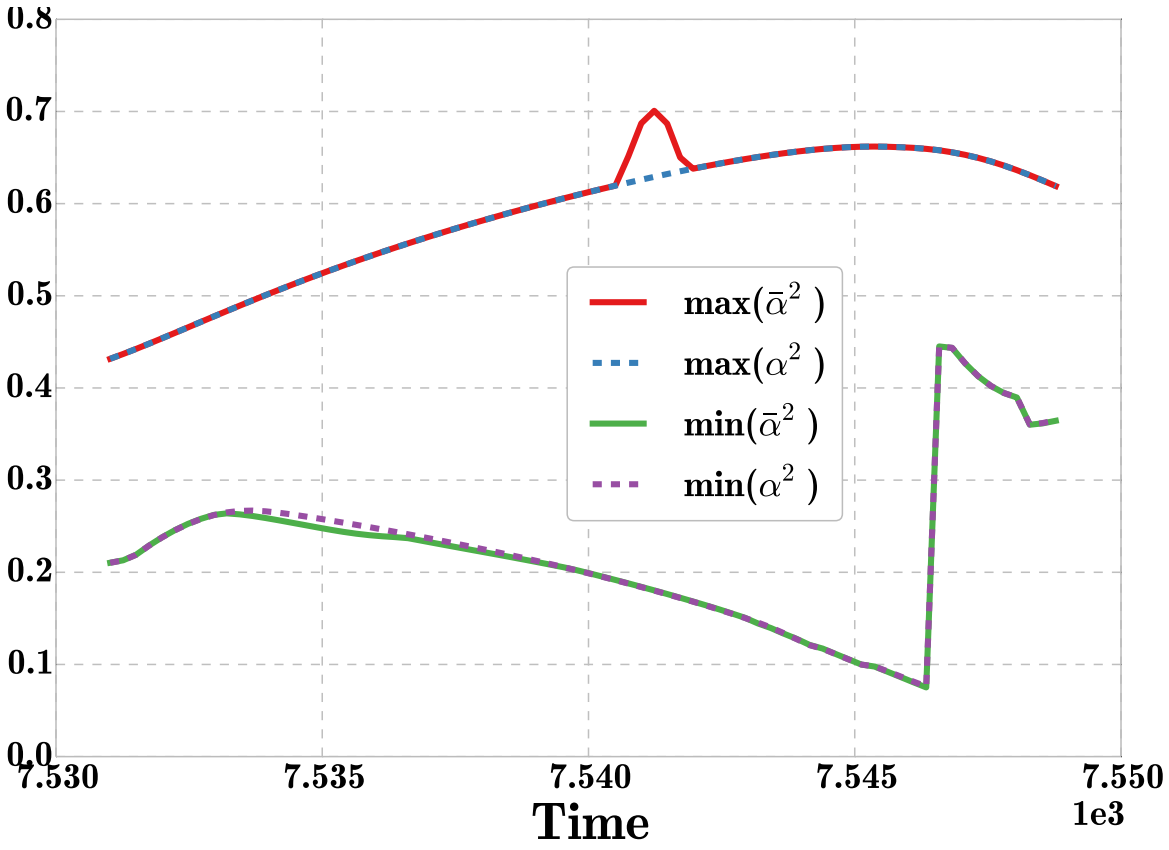

Figure 3.13: Confirmation that the lapse is well behaved for both the t and the $\bar{t}$ coordinate systems. The minimum and maximum values of α^2 are plotted as a function of time. Note that the large jump in the minimum lapse squared is caused by the domain regrid as SpEC transitions into the ringdown, and the coordinate transformation has no effect on the jump.

3.3.5 Baby event horizons

To obtain toroidal event horizons, we used a positive amplitude Gaussian in our coordinate transformation in Equation (3.1b) to delay generators in a small region around where the event horizons merge. We now consider the effect of a negative amplitude Gaussian that will advance generators in a small region.

The head-on BBH event horizon from Section 3.3.2 has all the future generators joining through caustics that form a one-dimensional spacelike line along the inseam of the pair of pants diagram. If we advance generators in a small region near this line, we can push the time slice across this spacelike line in a small region. The event horizon on the new time

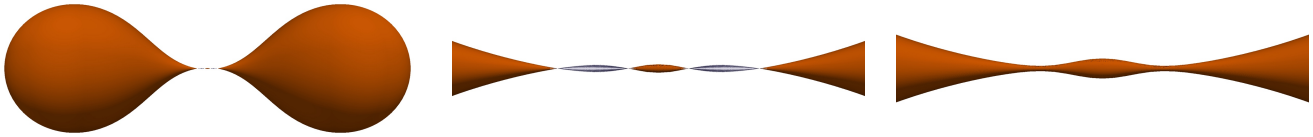

(a) $\bar{t} = 417.407M$: Zoomed out (b) $\bar{t} = 417.407M$ (c) $\bar{t} = 417.422M$

Figure 3.14: Event horizon of a head-on equal mass BBH merger, after performing the coordinate transformation with Case B of Table 3.1, but with a negative amplitude. Panel (a) is a zoomed out view of panel (b), where the topology of the event horizon is three spheres $3 \times \mathcal{S}^2$, before merging into one sphere in panel (c). This baby event horizon and the other systems in the discussion section Section 3.3 at the webpage [**?**].

slice would have the topology of three spheres $3 \times \mathcal{S}^2$ instead of $2 \times \mathcal{S}^2$ before the merger. In theory, we could make our time slicing cross the spacelike line of caustics as many times as we would like to create a topology of $n \times \mathcal{S}^2$, a possibility proved by Siino [9] in corollary III.8. This is directly demonstrated in Figure 3.14. We have also created an additional "baby" event horizon in more generic mergers such as the binary in Figure 3.1, where there are not only caustics but also crossover points.

Similarly, when we can reslice an event horizon to produce a torus with one hole, we can reslice into a torus with n holes. The crossover surface is spacelike, so we can construct a slicing that intersects this crossover surface an arbitrary number of times.

3.4 Conclusions

Siino [9] and Husa and Winicour [12] expected that merging black hole event horizons should generically have a brief toroidal topology. While simulations of rotating collapsing matter have shown event horizons that appear initially with a toroidal topology, the toroidal BBH event horizon has remained hidden during numerical simulations. While the $2+1$-dimensional event horizon hypersurface itself does not depend on the spacetime foliation, the choice of spacetime foliation does affect the topology of the EH on the slice. For the case of the inspiral and merger of two equal mass non-spinning black holes, we find the event horizon topology transitions directly from two spheres to one sphere in the SpEC coordinate slicing.

However, we show directly that a toroidal event horizon is possible through the use of a specially constructed coordinate transformation. The topology of the event horizon in the new coordinate system transitions from two spheres to a short-lived torus before transitioning finally to one sphere. No event horizons of merging black holes prior to this paper have yielded a toroidal topology [14, 15, 16, 23].

We believe that our reslicing method can be applied to the merger of any black holes with sufficient asymmetry (*i.e.*, not including a head-on merger of black holes where the symmetry prevents the possibility of a torus). Previous work has numerically found a surface of crossover points during the merger, where generators meet non-neighboring generators as they join the EH surface. Because this surface of crossover points is spacelike, we can apply our coordinate transformation to "cut a hole" through the crossover surface, while keeping the hypersurfaces of constant time spacelike. We therefore agree with Siino [9] and Husa and Winicour [12] that merging black holes should, in general, briefly have a toroidal event horizon topology, with the caveat that the torus may only exist in some foliations of the spacetime. It is interesting that Siino and Husa and Winicour predict tori generically, and expect slicings where there is no torus to be an exception to the rule. It is therefore somewhat surprising that in the time slicing used in SpEC and all other numerical codes, it appears that slicings with a toroidal event horizon are the exception to the rule.

As for topological censorship, because we are explicitly converting a spherical event horizon into a toroidal event horizon with our coordinate transformation, we are satisfying topological censorship by construction. That is, we can trivially reslice the event horizon back into a spherical topology, removing the topological torus, implying that the hole in the event horizon closes faster than the speed of light. Therefore a photon that appears to probe the topology of the spacetime by passing through the hole in the EH in one foliation of the spacetime will simply pass between the event horizons before they merge in another foliation. We note that while it is true one can always reslice a topological-censorship-satisfying torus into a sphere, the reverse is not always true.

Bibliography

[1] Steven W. Hawking and G. F. R. Ellis. *The Large Scale Structure of Space-time*. Cambridge University Press, Cambridge, England, 1973.

[2] S. W. Hawking. Black holes in general relativity. *Commun. Math. Phys.*, 25(2):152, 1972.

[3] Piotr T Chrusciel and Robert M Wald. On the topology of stationary black holes. *Class. Quantum Grav.*, 11(12):L147, 1994.

[4] Dennis Gannon. On the topology of spacelike hypersurfaces, singularities, and black holes. *Gen. Relativ. Gravit.*, 7(2):219, 1976.

[5] John L. Friedman, Kristin Schleich, and Donald M. Witt. Topological censorship. *Phys. Rev. Lett.*, 71(10):1486–1489, 1993. Erratum: [35].

[6] Gregory J Galloway. On the topology of the domain of outer communication. *Class. Quantum Grav.*, 12(10):L99, 1995.

[7] Ted Jacobson and Shankar Venkataramani. Topology of event horizons and topological censorship. *Class. Quantum Grav.*, 12(4):1055, 1995.

[8] Masaru Siino. Topological appearance of event horizon: What is the topology of the event horizon that we can see? *Progress of Theoretical Physics*, 99(1):1–32, 1998.

[9] Masaru Siino. Topology of event horizons. *Phys. Rev. D*, 58:104016, Oct 1998.

[10] S. A. Hughes, C. R. Keeton, P. Walker, K. T. Walsh, S. L. Shapiro, and S. A. Teukolsky. Finding black holes in numerical spacetimes. *Phys. Rev. D*, 49:4004, 1994.

[11] S. L. Shapiro, S. A. Teukolsky, and J. Winicour. Toroidal black holes and topological censorship. *Phys. Rev. D*, 52:6982, 1995.

[12] Sascha Husa and Jeffrey Winicour. The asymmetric merger of black holes. *Phys. Rev. D*, 60(8):084019, Sep 1999, gr-qc/9905039.

[13] Allen Hatcher. *Algebraic Topology*. Cambridge University Press, New York, NY, first edition, December 2001.

[14] Michael I. Cohen, Jeffrey D. Kaplan, and Mark A. Scheel. Toroidal horizons in binary black hole inspirals. *Phys. Rev. D*, 85:024031, 2012, 1110.1668.

[15] Peter Diener. A new general purpose event horizon finder for 3D numerical spacetimes. *Class. Quantum Grav.*, 20:4901–4917, 2003.

[16] M. Ponce, C. Lousto, and Y. Zlochower. Seeking for toroidal event horizons from initially stationary BH configurations. *Class. Quantum Grav.*, 28(14):145027–+, July 2011, 1008.2761.

[17] B. P. Abbott et al. Observation of Gravitational Waves from a Binary Black Hole Merger. *Phys. Rev. Lett.*, 116(6):061102, 2016, 1602.03837.

[18] R. Penrose. Structure of space–time. *pp 121-235 of Battelle Rencontres. DeWitt, Cecile M. (ed.). New York W. A. Benjamin, Inc.*, Jan 1968.

[19] Robert M. Wald. *General Relativity*. University of Chicago Press, Chicago, IL, 1984.

[20] Peter Anninos, David Bernstein, Steven Brandt, Joseph Libson, Joan Massó, Edward Seidel, Larry Smarr, Wai-Mo Suen, and Paul Walker. Dynamics of apparent and event horizons. *Phys. Rev. Lett.*, 74:630–633, Jan 1995.

[21] Stuart L. Shapiro and Saul A. Teukolsky. Gravitational collapse to neutron stars and black holes: Computer generation of spherical spacetimes. *Astrophys. J.*, 235:199–215, 1980.

[22] J. Libson, J. Massó, E. Seidel, W.-M. Suen, and P. Walker. Event horizons in numerical relativity: Methods and tests. *Phys. Rev.*, D53:4335–4350, 1996.

[23] Michael Cohen, Harald P. Pfeiffer, and Mark A. Scheel. Revisiting event horizon finders. *Class. Quantum Grav.*, 26:035005, 2009, arXiv:0809.2628.

[24] L. Lehner, N Bishop, R. Gomez, B Szilágyi, and J Winicour. Exact solutions for the intrinsic geometry of black hole coalescence. *Phys. Rev. D*, 60:044005, 1999, 9809034.

[25] S. Browdy and G. Galloway. Topological censorship and the topology of black holes. *J. Math. Phys. 36, 4952*, April 1995.

[26] http://www.black-holes.org/SpEC.html.

[27] Béla Szilágyi, Lee Lindblom, and Mark A. Scheel. Simulations of binary black hole mergers using spectral methods. *Phys. Rev. D*, 80:124010, 2009, 0909.3557.

[28] Daniel A. Hemberger, Mark A. Scheel, Lawrence E. Kidder, Béla Szilágyi, Geoffrey Lovelace, Nicholas W. Taylor, and Saul A. Teukolsky. Dynamical excision boundaries in spectral evolutions of binary black hole spacetimes. *Class. Quantum Grav.*, 30(11):115001, 2013, 1211.6079.

[29] http://www.black-holes.org/waveforms.

[30] Lee Lindblom, Mark A. Scheel, Lawrence E. Kidder, Robert Owen, and Oliver Rinne. A new generalized harmonic evolution system. *Class. Quantum Grav.*, 23:447, August 2006, gr-qc/0512093.

[31] Andy Bohn, Lawrence E. Kidder, and Saul A. Teukolsky. A Parallel Adaptive Event Horizon Finder for Numerical Relativity. 2016.

[32] Kip Thorne. Suggestion to the authors of [20, 22] that the locus of all event horizon generators forms at all times a smooth and sometimes self-intersecting surface.

[33] Simulating eXtreme Spacetimes. http://www.black-holes.org/.

[34] J Massó, E Seidel, W-M Suen, and P Walker. Event horizons in numerical relativity. II. analyzing the horizon. *Phys. Rev. D*, 59:064015, 1999.

[35] John L. Friedman, Kristin Schleich, and Donald M. Witt. Topological censorship[phys. rev. lett. 71, 1486 (1993)]. *Phys. Rev. Lett.*, 75:1872–1872, Aug 1995.

4 Event horizons on slices of constant affine parameter

In this section, we present unpublished and unfinished work toward the goal of locating a toroidal event horizon in merging black black hole binaries. In private communication with Winicour, he suggested that viewing the event horizon on slices of constant affine parameter might produce a toroidal topology. As discussed in Section 3.2, we need to delay event horizon generators that join the event horizon during the merger in order to see a short-lived torus. From simple approximations of p^0 for ingoing and outgoing geodesics near a Schwarzschild black hole, as well as from numerical data in a BBH simulation, we see that the future generators are in fact delayed, but the delay is larger than expected, and does not produce smooth event horizons.

We present the status of this work and the methodology here.

4.1 Event horizons on slices of constant affine parameter

We can straightforwardly find the $2+1$-dimensional event horizon surface on spacelike hypersurfaces of constant SpEC coordinate time, t. There is no evidence that the topology of the surface is ever toroidal for any BBH event horizon we have located to date, in the generalized harmonic slicing used in SpEC [1, 2]. This does not imply that there is no slicing of the event horizon where the topology of the surface is toroidal, but only that toroidal topologies are at best rare in the gauge used in SpEC when the black holes merge. The main

text of this paper presents a coordinate transformation that can be applied to the SpEC coordinates that can yield a short-lived toroidal topology during the merger. Are there, in some sense, more general coordinates where the event horizon more often than not visits a toroidal topology during BBH mergers as predicted by Husa and Winicour [3]?

Winicour [4] has suggested that viewing the event horizon on slices of constant affine parameter might produce a toroidal topology. Each generator of the event horizon can be reparametrized by an affine parameter by evolving

$$\frac{d^2t}{d\lambda^2} = \frac{dp^0}{d\lambda} = p^0 \frac{dp^0}{dt} = -\Gamma^0{}_{\nu\tau} p^\nu p^\tau \tag{4.1}$$

with the definition $p^\mu = dx^\mu/d\lambda$, where λ is an affine parameter. One immediate complication is that there is not a unique affine parametrization of a geodesic trajectory, since $\lambda \to a\lambda + b$ is also an affine parameter for any constants a and b. Ignoring this temporarily, we solve for an affine parametrization for each generator by splitting Equation (4.1) into two first order differential equations

$$\frac{dp^0}{dt} = -\frac{1}{p^0}\Gamma^0{}_{\nu\tau} p^\nu p^\tau \tag{4.2a}$$

$$\frac{d\lambda}{dt} = \frac{1}{p^0}. \tag{4.2b}$$

Unfortunately, in the BBH coordinate systems of interest, these evolution equations produce exponential solutions, leading to small timesteps. Consider an event horizon generator on the surface of a Schwarszchild black hole event horizon in the Kerr-Schild coordinate system. The time dependence of this generator goes as

$$p^0 = C_1 \exp\left(-t/4\right) \tag{4.3a}$$

$$\lambda = 4C_1 \exp\left(t/4\right) + C_2, \tag{4.3b}$$

for integration constants C_1 and C_2. These quantities are similarly exponential for coordinate systems used in SpEC as well.

This suggests evolving the logarithm of these coordinates, giving the evolution equations

$$\frac{d\ln p^0}{dt} = -\frac{\alpha_{,t}}{\alpha} + \alpha_{,i}\left(\frac{\beta^i}{\alpha} - 2\Pi^i\right) + \alpha K_{ij}\Pi^i\Pi^j \tag{4.4a}$$

$$\frac{d\ln \lambda}{dt} = \exp\left[-\ln p^0 - \ln\lambda\right], \tag{4.4b}$$

where the Christoffel symbols from Equation (4.2) have been expanded, simplified, and put in terms of our momentum variable Π^i and the ADM decomposition variables. This results in fast evolutions that are sufficiently accurate compared to the values obtained from Equation (4.3).

While the BBH evolution must be performed forwards in time, and the generator evolution $(q^i,\, \Pi_j)$ should be performed backwards in time, we can choose which directions in time to evolve $\ln p^0$ and $\ln\lambda$. The $\ln\lambda$ initial data is the primary concern for choosing evolution direction, because of the integration constants in Equation (4.3). We have more control over the constant C_2 by choosing the initial data for forwards in time evolution, so we evolve $\ln\lambda$ in that direction. This leaves the choice of direction of time for the $\ln p^0$ evolution. We note that the forwards in time evolution for $\ln\lambda$ does not require any metric data, but the $\ln p^0$ evolution equation is a function of the metric. For this reason, we evolve $\ln p^0$ backwards in time along with the generator location evolution. Finally, since the $\ln\lambda$ evolution equation requires $\ln p^0$ values at arbitrary times, we perform a Lagrange polynomial interpolation using a set of saved $\ln p^0$ values.

Once the $\ln\lambda$ evolution is completed, we use the freedom of the rescaling of the affine parameter to make all generators agree at late times when the event horizon is static. If we take a Taylor expansion of Equation (4.3) with respect to t, the affine parameter goes as $\lambda \sim t$, so the SpEC coordinate time acts like an affine parameter on short time scales. This allows us to enforce that all generators agree on λ as well as $\partial_t\lambda$ after the horizon has settled

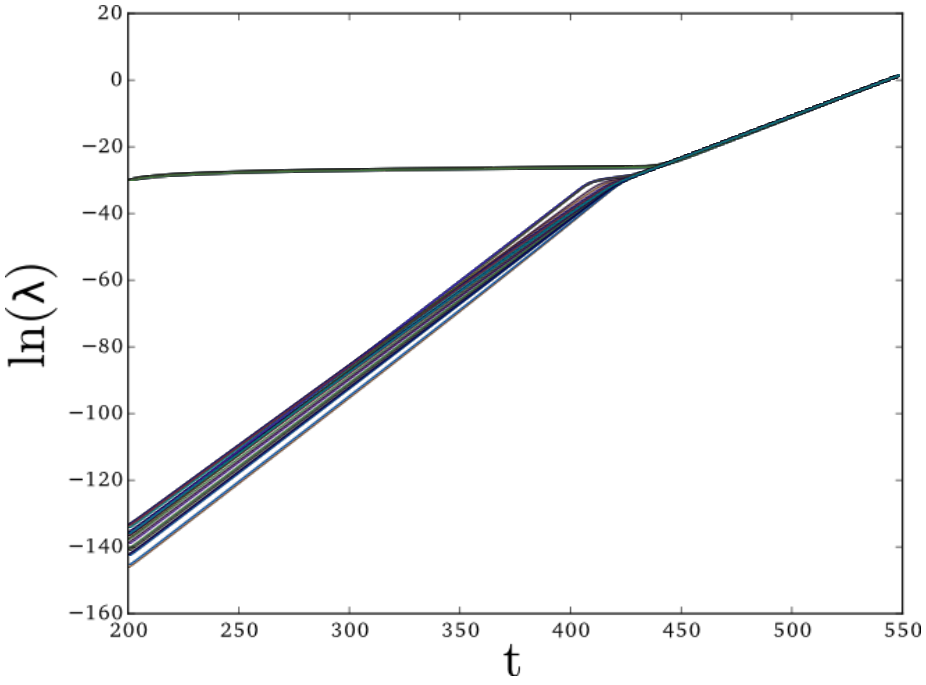

Figure 4.1: $\ln\lambda$ for a random set of event horizon generators in the equal mass head-on BBH simulation. We see two clear sets of trajectories, one set of generators that stay on the horizon for the event horizon simulation and follow an exponential time dependence, and another for those generators that leave the horizon and follow a linear time dependence.

to a constant, using $\lambda \to a\lambda + b$.

Figure 4.1 shows $\ln\lambda$ for a set of generators versus SpEC simulation time t for an equal mass non-spinning head-on binary. At early times, we see two distinct types of generators. We have a group of generators that are generators of the horizon, and so follow the exponential time dependence as expected in Equation (4.3). The other set of generators are future generators of the horizon, and have not yet joined onto the horizon. We expect $\lambda \sim t$ for these generators as they head toward the black holes. Near the merger at $t \approx 417$, future generators join the event horizon and transition to the exponential time dependence expected for generators on the surface. At late times, all the generators follow the same exponential time dependence as expected for a Schwarzschild black hole. However, it is not clear why all the future generators have the same $\ln\lambda$ value when they join the horizon. We expected to see a continuum of affine parameters when generators join the horizon, since

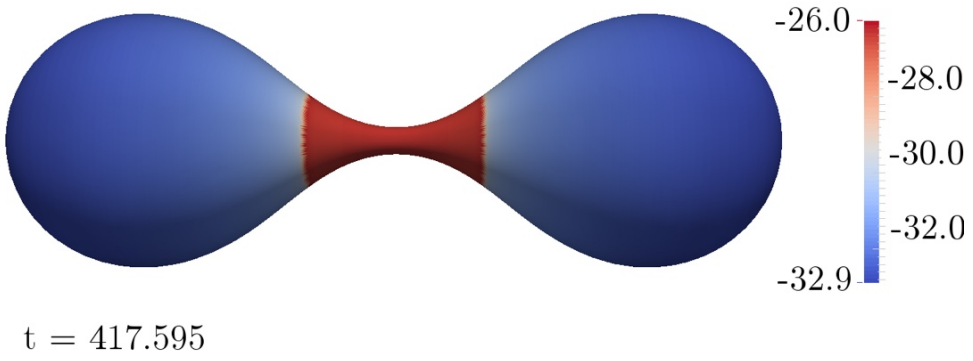

Figure 4.2: Constant SpEC coordinate time slice of the equal mass head-on BBH event horizon colored by $\ln\lambda$, at a time shortly after the merger of the event horizons. We see that the affine parameter in the neck of the horizon is larger relative to generators elsewhere on the horizon.

future generators are continually joining the surface as early as the beginning of the event horizon simulation. Otherwise, we expected that future generators would be associated with larger affine parameter values than event horizon generators to have a chance to see a toroidal event horizon in an affine slicing.

Figure 4.2 shows the event horizon surface in a constant t slice, colored by $\ln\lambda$. This is equivalent to taking a vertical slice through the plot in Figure 4.1. Near the neck of the horizon, we see that the affine parameter is larger compared to the rest of the surface. When reslicing this to constant $\ln\lambda$ values, equivalent to taking horizontal slices through the plot in Figure 4.1, this would have the effect of causing the generators in the neck of the horizon to join the event horizon surface later relative to the rest of the horizon. This is the correct idea, but the red region is larger than expected and does not transition as smoothly as expected across the surface of the event horizon.

It is not obvious that a constant affine parameter slicing across the entire event horizon is a well posed concept. We do see some evidence that this idea is promising, but could not

make progress beyond what is shown here.

Bibliography

[1] Michael I. Cohen, Jeffrey D. Kaplan, and Mark A. Scheel. Toroidal horizons in binary black hole inspirals. *Phys. Rev. D*, 85:024031, 2012, 1110.1668.

[2] Michael Cohen, Harald P. Pfeiffer, and Mark A. Scheel. Revisiting event horizon finders. *Class. Quantum Grav.*, 26:035005, 2009, arXiv:0809.2628.

[3] Sascha Husa and Jeffrey Winicour. The asymmetric merger of black holes. *Phys. Rev. D*, 60(8):084019, Sep 1999, gr-qc/9905039.

[4] Jeffrey Winicour. private communication, 2014.

Part II

Extreme gravitational lensing

5 What does a binary black hole merger look like?

Abstract

We present a method of calculating the strong-field gravitational lensing caused by many analytic and numerical spacetimes. We use this procedure to calculate the distortion caused by isolated black holes and by numerically evolved black hole binaries. We produce both demonstrative images illustrating details of the spatial distortion and realistic images of collections of stars taking both lensing amplification and redshift into account. On large scales the lensing from inspiraling binaries resembles that of single black holes, but on small scales the resulting images show complex and in some cases self-similar structure across different angular scales.

Authors: Andy Bohn, William Throwe, François Hébert, Katherine Henriksson, Darius Bunandar, Mark A. Scheel, Nicholas W. Taylor

Published in *Classical and Quantum Gravity*, Volume 32, Number 6, on February 23rd, 2015.

5.1 Introduction

Black holes are the most compact gravitating objects in the universe, with such strong gravitational fields that not even light can escape them. In the vicinity of a black hole, light rays can be very strongly deflected from a straight-line path, sometimes orbiting around the

black hole before continuing on their way. It is now well-known that the bending of light by massive objects like galaxy clusters can create brightness amplification [1], deformed images, or even multiple images [2] of background objects such as quasars. These signatures have so far only been directly observed in cases where the deflection of light is very slight, up to approximately 11 arc seconds [3, 4]. However, here we are interested in the lensing effects associated with much more extreme bending of light near single or binary black holes, where the deflection angle is unbounded.

The lensing effects near general-relativistic bodies were first studied in the 1970s, with Cunningham and Bardeen [5] looking at a star on an orbit in a Kerr spacetime, and Luminet [6] studying an accretion disk around a Schwarzschild black hole. More recently, open-source codes such as GYOTO [7] and GeoViS [8] have produced images of lensing in the neighborhood of various compact objects. While the lensing caused by an isolated black hole has been understood analytically, the case of lensing by a binary black hole (BBH) is much more challenging because of the difficulty of solving for the geometry of the spacetime. With some arguably unrealistic assumptions (e.g., two maximally charged black holes in static equilibrium), analytic solutions can be found and subsequently used for lensing [8, 9, 10, 11, 12, 13].

For astrophysically relevant binaries, however, we must instead rely on numerical solutions. Solving these binary spacetimes numerically to high accuracy has been possible for the last decade (see [15, 16] for a review), motivated by the need to provide gravitational-wave templates used by experiments such as LIGO, VIRGO, and KAGRA to make detections. By using the spacetimes computed in such simulations, we gain the ability to solve for the lensing effects in BBH systems.

In this paper, we focus on the question of what an observer in the vicinity of a BBH would actually *see* as the black holes orbit, spiral inward, and merge, with an example shown in figure 5.1. This is in contrast to most BBH visualizations, in which the positions or horizons of the two black holes are simply shown as a function of time in some coordinate system. We

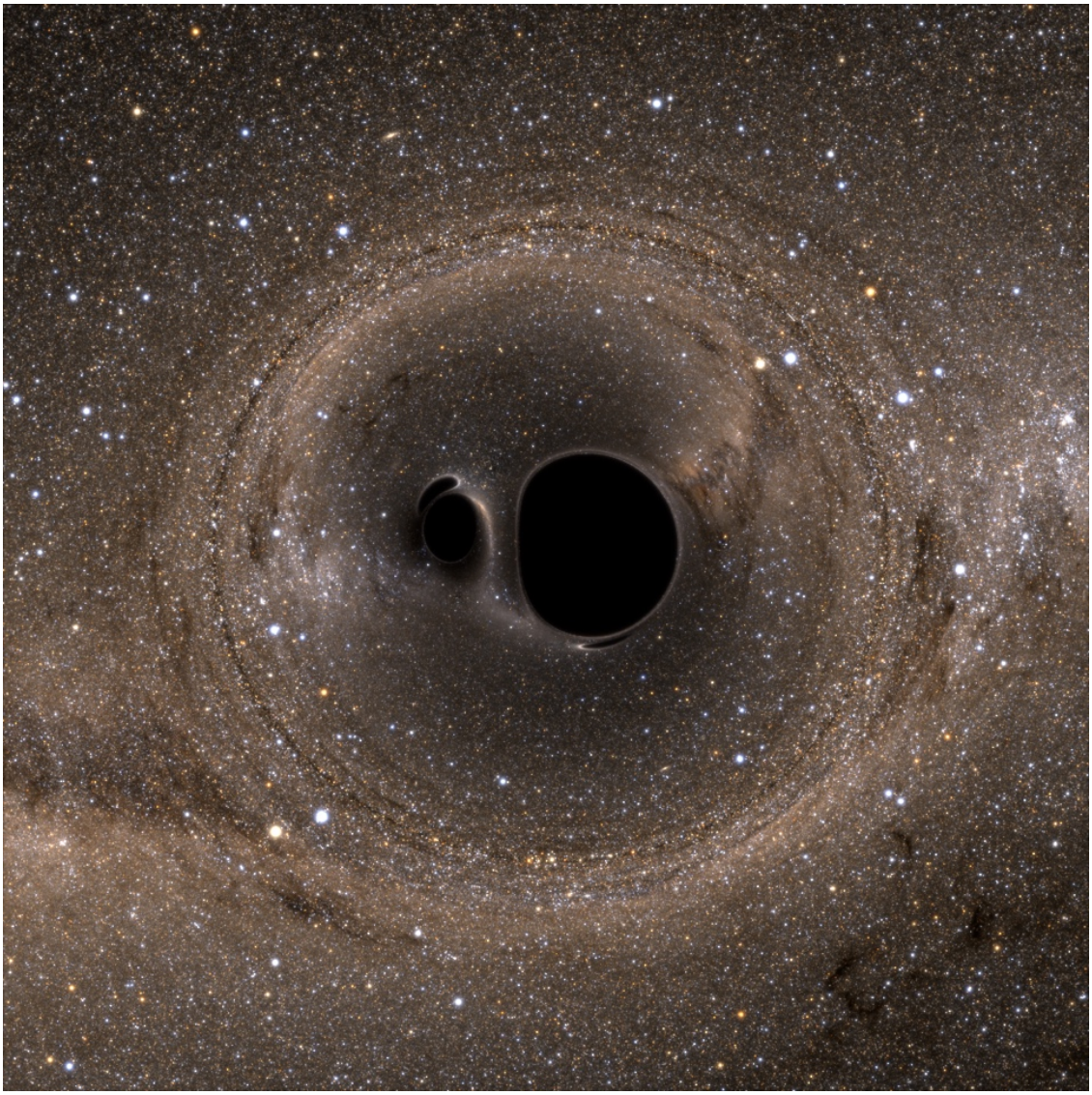

Figure 5.1: A pair of black holes that are about to merge, with the Milky Way visible in the background. Supplementary images and movies can be found at [14].

instead compute the paths of light rays that enter the observer's eye or camera to find what would actually be seen. Furthermore, this path must be computed in the fully time-dependent spacetime, as the orbital velocities for a black-hole binary are typically large enough that the system cannot be approximated as time-independent during the time taken by the photons to travel across it.

Because the black holes themselves do not emit light (we ignore Hawking radiation, which is significant only for microscopic black holes), the observer would see nothing unless there is

some additional light source. For illustrative purposes, we will take an artificial background "painted on" at infinity (figure 5.2) as the light source for most of our examples; this will allow us to study in detail where each light ray originates.

We begin by describing the problem setup and the methods that we use to generate lensing images in section 5.2. In section 5.3 we show images of lensing by single and binary black holes, and we then conclude in section 5.4.

5.2 Methods

We set up the problem with our black hole(s) near the center of our chosen coordinate system. While any physical system representable by a spacetime metric can be used, we specialize in this paper to single and binary black holes. The observer (henceforth taken to be a camera) can be located anywhere in the space and is typically chosen to look towards the origin. A sphere with our light source encloses the black hole(s) and camera, infinitely far away.

To recreate the image taken by the camera in this configuration, we must find the properties of the light that arrives at each point on the camera's image plane. A naïve approach would be to trace all possible light rays (i.e., null geodesics) emanating from the light source to determine which rays reach the camera and from what directions they arrive, but this is computationally infeasible. A more efficient approach is to reverse the problem by tracing light rays away from the camera and *backwards* in time (the computer graphics community calls this a ray-casting algorithm). This method identifies the origin of any light ray that illuminates the camera, from which we infer the color and intensity of the corresponding photons as detected by the camera. When black holes are present, some of the null geodesics traced backwards in time from the camera may approach arbitrarily close to an event horizon as $t \to -\infty$; these geodesics correspond to dark image regions.

In what follows we describe how the light rays are traced from the camera using the geodesic language from general relativity. We show how we initialize these geodesics based on camera parameters such as position and viewing angle. Finally, we show how the origin of

each light ray is determined and describe how the simulated image is constructed.

5.2.1 Geodesic tracing

Our code can trace geodesics independently through either numerical or analytic metric data. It is common for numerical simulations to use the $3+1$ decomposition [17], so we express the metric in the form

$$ds^2 = -\alpha^2 dt^2 + \gamma_{ij}(dx^i + \beta^i dt)(dx^j + \beta^j dt), \tag{5.1}$$

where α is the lapse function, β^i is the shift vector, and γ_{ij} is the spatial metric.[1] We obtain numerical data from simulations performed using the Spectral Einstein Code (SpEC) [18, 19, 20, 21, 22]. The geodesics are traced by evolving a solution to the geodesic equation

$$\frac{d^2x^\lambda}{d\tau^2} + \Gamma^\lambda{}_{\mu\nu}\frac{dx^\mu}{d\tau}\frac{dx^\nu}{d\tau} = 0, \tag{5.2}$$

where x^λ is the four-position of the geodesic, τ is an affine parameter, and $\Gamma^\lambda{}_{\mu\nu}$ are the Christoffel symbols describing the effective force caused by spacetime curvature.

To facilitate the numerical geodesic evolution, we split this second-order differential equation into two first-order differential equations using an intermediate, momentum-like variable such as $p^\lambda = dx^\lambda/d\tau$. As we have some freedom in the definition of this momentum variable, we look for one that helps to minimize computational time and numerical errors when evolving through spacetimes with black holes.

We initially explored using the variable $p_\lambda = g_{\lambda\kappa}p^\kappa$ from Hughes *et al.* [23], along with converting the evolution equations from affine parameter τ to the coordinate time t of SpEC evolutions through the use of $p^0 = dt/d\tau$. Although the resulting evolution equations are concise and have no time derivatives of metric variables, the variables p^0 and p_i grow exponentially near black hole horizons in typical coordinate systems used by SpEC simulations. This forces our time-stepper to take prohibitively small steps in order to achieve the desired

[1] Our convention is that Greek indices, as in x^λ, denote temporal or spatial components, while Latin indices, as in x^i, denote only spatial components.

accuracy.

We therefore choose a momentum variable slightly different than p_λ to mitigate this time-stepping problem. Null geodesics satisfy $p \cdot p = 0$, which can be rewritten as $p^0 = \alpha^{-1}(\gamma^{ij} p_i p_j)^{1/2}$ using the metric (5.1). This expression shows that p^0 and p_i scale similarly, so we can eliminate the exponential behavior of these variables by evolving the ratio. Our intermediate variable thus becomes

$$\Pi_i \equiv \frac{p_i}{\alpha p^0} = \frac{p_i}{\sqrt{\gamma^{jk} p_j p_k}}, \tag{5.3}$$

where we also divide by α to reduce the number of terms in the resulting evolution equations. Using Π_i and the $3+1$ decomposition (5.1), we can express the geodesic equation (5.2) in the form

$$\begin{aligned} \frac{d\Pi_i}{dt} =& -\alpha_{,i} + (\alpha_{,j}\Pi^j - \alpha K_{jk}\Pi^j\Pi^k)\Pi_i \\ &+ \beta^k{}_{,i}\Pi_k - \frac{1}{2}\alpha\gamma^{jk}{}_{,i}\Pi_j\Pi_k, \\ \frac{dx^i}{dt} =& \alpha\Pi^i - \beta^i, \end{aligned} \tag{5.4}$$

where K_{jk} is the extrinsic curvature (see, e.g., [17]) and Π^i is defined via the inverse spatial metric as $\Pi^i \equiv \gamma^{ij}\Pi_j$. Note that the geodesic equation consists of four second-order equations, yet we only have three pairs of coupled first-order equations in (5.4). Because we are evolving a normalized momentum (5.3), we have lost information about p^0 during evolution. Compared to Hughes *et al.* [23], we have introduced a time derivative of the three-metric inside K_{jk}, but we have significantly sped up the evolution near black holes by removing the exponential growth of p^0 and p_i.

The equations in (5.4) are similar to those in (28) of Vincent *et al.* [24]. In fact our intermediate evolution variable Π_i is related to their variable V^i by the three-metric, such that $\Pi^i = V^i$. But our (5.4) has a reduced number of both temporal and spatial derivatives of metric quantities compared to Vincent's (28).

During the backwards-in-time geodesic evolution, many geodesics are traced until they are far from the strong-field region, but some are traced until they encounter a black hole. These latter geodesics slowly converge towards the black hole's event horizon, but as they can in principle be evolved indefinitely, we need some way of identifying them in finite time. We do this by monitoring p^0 for each geodesic, which (as discussed above) grows large near black hole horizons. Since our evolution equations (5.4) do not evolve p^0, we must evolve another equation to keep track of it. However, we would still like to avoid the exponential growth of p^0 near the horizon. This can be accomplished by evolving the logarithm of p^0. As was done in (5.3), we multiply p^0 by the lapse to reduce the number of terms in the resulting equation, which gives the evolution variable $\ln(\alpha p^0)$. This leads to the evolution equation

$$\frac{d\ln(\alpha p^0)}{dt} = -\alpha_{,i}\Pi^i + \alpha K_{ij}\Pi^i\Pi^j. \tag{5.5}$$

When p^0 becomes too large, signaling a large energy, we flag the geodesic as originating from the black hole and we stop evolving it.

The remaining geodesics are those that originate from infinity, so we need to determine the (θ,ϕ) location at infinity where they come from. In section 5.2.3, we will need the gravitational redshift z of each photon, which can be calculated from the ratio of the photon's energy at the two ends of its trajectory via

$$1 + z = \frac{E_\infty}{E_{\text{camera}}}, \tag{5.6}$$

where E_∞ is the photon's energy at infinity, and E_{camera} is the photon's energy as measured by the camera. Therefore we will need to compute the energy that each photon would have at infinity. In practice, these geodesics are traced backwards in time until they reach a large distance R from the black hole(s), chosen so that the metric at R is equal to the flat space metric within about a percent error. We use the approximation that the metric is exactly flat for $r > R$. Under this approximation, the geodesic's direction and p^0 at infinity are the same as at R. The direction is used to calculate a (θ,ϕ) location on the sky, while p^0 is the

photon's energy at infinity, E_∞.

5.2.2 Initial data

Here we outline how we initialize our geodesic evolution variables. Because the geodesics are traced away from the camera, backwards in time, we initialize each geodesic's evolution variables to their values at the camera. We have seven variables to set: three each for the initial position and momentum in (5.4), and one for the initial redshift in (5.5).

The initial position for every geodesic is simply the camera's position. The initial momentum, however, is different for each geodesic and is dependent on the angle at which it enters the camera. We express the momenta in terms of an orthonormal tetrad defined as

e_0 The camera's four-velocity, a timelike vector. For stationary cameras $e_0 \propto (1, 0, 0, 0)$;

e_1 The direction in which the camera is pointing;

e_2 The "upward" direction for the camera;

e_3 The "rightward" direction for the camera.

The four-vectors e_1, e_2, and e_3 are all spacelike, and their orientations in the camera's reference frame are illustrated in figure 5.1.

In order to specify this tetrad, we give guesses for the vectors e_0, e_1, and e_2, with the condition that the guessed time components of e_1 and e_2 must be zero. We then apply the Gram-Schmidt process to the sequence e_0, e_1, and e_2 to transform these vectors into an orthonormal set. The final vector, e_3, is found by calculating the generalized cross product of the other three; explicitly,

$$e_{3\rho} = \epsilon_{\lambda\mu\nu\rho} e_0{}^{\lambda} e_1{}^{\mu} e_2{}^{\nu}, \tag{5.7}$$

where $\epsilon_{\lambda\mu\nu\rho}$ is the Levi-Civita tensor (see [25, p. 202] for more details).

Given the four orthonormal unit vectors, we can construct a null vector ξ tangent to the geodesic that enters the camera from a given direction. The vector ξ will be proportional

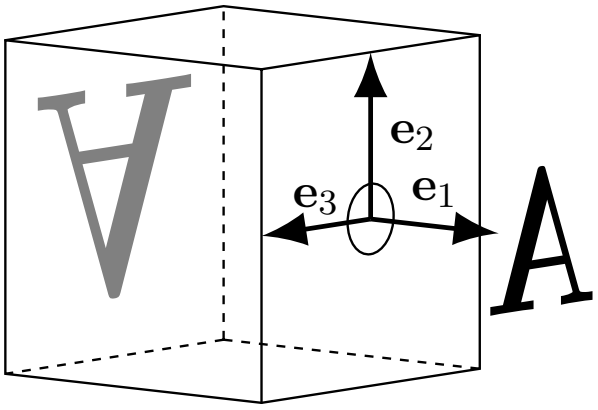

Figure 5.1: Illustration of a pinhole camera in its rest frame with the three vectors e_1, e_2, and e_3 that describe its orientation. The inverted letter "A" demonstrates the optical properties of the camera, which we correct for in the images we generate.

to the four-momentum of a photon following the geodesic; that is, $p = q\xi$ for some positive constant q. We define ξ by

$$\begin{aligned}\xi^{\lambda}{}_{(a,b)} = C{e_0}^{\lambda} - {e_1}^{\lambda} - [(2b-1)\tan(\alpha_v/2)]{e_2}^{\lambda} \\ - [(2a-1)\tan(\alpha_h/2)]{e_3}^{\lambda},\end{aligned} \tag{5.8}$$

where $a, b \in [0, 1]$ give the ray's arrival direction in terms of fractions of the image's horizontal and vertical lengths, respectively, and α_v, α_h are the angular sizes of the camera aperture (field of view angles) in the vertical and horizontal directions. For the sign convention chosen in (5.8), $(a, b) = (0, 0)$ corresponds to a photon seen at the bottom left corner of the image. We find C by requiring that ξ is null, i.e., $\xi \cdot \xi = 0$:

$$C = \sqrt{1 + (2b-1)^2\tan^2(\alpha_v/2) + (2a-1)^2\tan^2(\alpha_h/2)}. \tag{5.9}$$

We then use the metric to lower the index on ξ, and we compute the initial value of our evolution variable Π_i using $\Pi_i = p_i/(\alpha p^0) = \xi_i/(\alpha\xi^0)$. Note that Π_i is independent of the proportionality constant q relating ξ and the actual photon momentum p; physically, this is because the photon trajectory is independent of the photon energy. The only place where q enters is in the initial value of αp^0 in (5.5). We fix the value of q by demanding that the

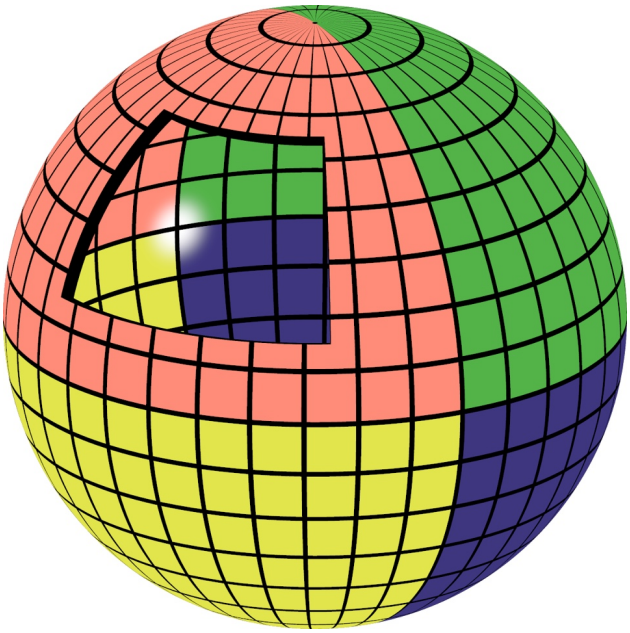

Figure 5.2: An illustration of our artificial background grid "painted on" a sphere at infinity. This background is used for all the images with a grid in this paper. In the figure, we cut a window out of the sphere to show the inside. In addition to four colors differentiating the regions of the sphere, we include a white reference spot in the direction in which the camera is pointing.

energy of the photon in the frame of the camera be unity when the photon strikes the camera, so $E_{\text{camera}} = 1$ in (5.6).

5.2.3 Image generation

We create our image of the physical system by dividing the image plane into rectangular regions corresponding to the pixels of the output image and assigning an appropriate color to each region. Because each region has an extended size, there is no single source point we can look at to obtain its color, so we must adopt some prescription for assigning a single color to each pixel. We use two different prescriptions, based on the nature of the light source illuminating the system.

For extended sources, such as the artificial grid in figure 5.2, we use a subpixel sampling method. On each pixel we construct an evenly spaced grid of points, and at each of these points we determine where incident light rays originate, either from one of the holes or a

location at infinity. We assign a color to each grid point based on that of the corresponding source point; the color of the pixel is then the average of these. We find that a grid of 4×4 sample points gives sufficiently smooth images without too much computational cost. For these images, we neglect the effects of redshift and focus on the spatial distortions.

To create more astronomically relevant images, we wish to use a collection of point sources (i.e., stars) as our illumination. In this case we cannot determine a pixel's color using sampling, but must instead sum the contributions from all the point sources contributing light there. For our list of sources, we use about 3.4×10^8 stars from the Two Micron All Sky Survey (2MASS) [26]. To simplify computations, we approximate each star as a thermal source with temperature and brightness determined by fitting to the photometric information in the catalog. When we calculate the contribution of each star to the light arriving at the camera, we must account not only for its properties as a light source, but also for the effects of the spacetime curvature encountered by the photon. These effects come in two forms. First, the observed energies of photons at the camera will be modified by redshift effects, changing sources' apparent brightnesses and temperatures. Second, the spatial convergence or divergence of nearby geodesics produces an overall adjustment to each source's apparent brightness without affecting its spectrum. Both of these effects are discussed in detail in Mollerach and Roulet [27]. After we have drawn the entire image in this manner, we convolve it with a blurring function to make the stars more visible. This has the effect of transforming each star into a fuzzy circle with size dependent on its brightness.

The result of this scheme can be seen in figure 5.1, which shows the BBH image from figure 5.8 in front of a background of stars. Note that by generating our starfield images from a catalog of point sources, we obtain a substantially more realistic image than would be generated by applying the lensing deformation to a raster image of the unlensed Milky Way stars. In such a raster image, each star is usually represented (whether as a result of camera optics or software rendering) as a blurred circle whose area depends on the star's brightness. These circles are typically hundreds of arc seconds wide, and therefore lensing distortions

applied to the image tend to produce stars that appear as smeared ellipses. In contrast, the angular sizes of real stars are many orders of magnitude smaller, so we expect them to remain as unresolved points under all but the most extreme lensing magnifications. These unresolved points can then be rendered as previously described, giving stars that better portray what an observer would actually see (as in figure 5.1). The difference between these methods lies in the non-commutativity between the lensing deformations and the blurring of each star. A minor shortcoming of our method arises at Einstein rings (discussed in section 5.3.1), where the magnification diverges. There a star could in principle (though with very low probability) appear as an extended object, but in our treatment it would remain point-like. On the other hand, blurring first and then lensing is almost guaranteed to produce unphysical extended streaks at the Einstein ring.

5.3 Results

Before applying our lensing code to binary black hole systems, we generate images of simpler analytic spacetimes. These serve both to provide checks that our images are consistent with earlier work, and also to illustrate general features of lensing around black holes that will appear again in BBH images. We then proceed to show two different configurations of BBH mergers.

To help visualize the lensing, we divide our light source at infinity into colored quadrants with a superimposed grid. An external view of this sphere is shown in figure 5.2. In addition to the colored sections, our light source has a bright reference spot in the direction towards which we point our camera. This spot will prove useful in illustrating an important feature of black hole lensing called an Einstein ring.

5.3.1 Analytic spacetimes

In figure 5.1, we compare a flat space image with the images obtained by lensing our light source through Schwarzschild and Kerr black hole spacetimes. The top row from left to right

shows flat Minkowski space and a Schwarzschild black hole. These spacetimes are spherically symmetric, so viewing them from different angles produces the same lensing effects. The bottom row shows a Kerr black hole, where in the left frame the spin vector is pointing out of the page and in the right frame it is pointing up. Here the spin breaks the spherical symmetry of the spacetime, leading to different lensing effects from different viewing directions.

In Minkowski space in the top left image we expect no deflection of light, which is what we observe. The camera sees an upright image of the portion of the grid near the white dot. The bowing of the grid lines is an expected geometric effect of viewing a latitude-longitude grid.

In the top right image, we see the lensing effects of a non-spinning black hole. The black circle in the center of the image is called the shadow of the black hole, where the hole prevents any light from reaching the camera. Alternatively, a shadow is a region of the image where geodesics are traced backwards in time from the camera to a black hole. Another prominent feature is that the white dot on our grid at infinity has been lensed into a large ring, called an Einstein ring [28]. Light from the point situated directly on the opposite side of the black hole, the antipodal point, will by symmetry be lensed into a ring around the black hole as observed by our camera. Regions inside the Einstein ring correspond to photons that are deflected by larger angles than are the Einstein ring photons; this results in an inverted image of the reference grid inside the Einstein ring. A second Einstein ring can be seen near the shadow, corresponding to light from a source behind the camera wrapping around the hole on its way to the camera. In fact, photons can wind an arbitrarily large number of times around the black hole, resulting in an infinite number of Einstein rings.

The bottom row of figure 5.1 shows a single black hole with a large dimensionless spin of $\chi = 0.95$. As in the Schwarzschild case, there is an Einstein ring around the black hole shadow as well as image inversion inside the Einstein ring. However, for the case of a Kerr spacetime, the light coming from the Einstein ring does not originate from a single point directly behind the black hole, but from a small region (unless the camera is pointing directly

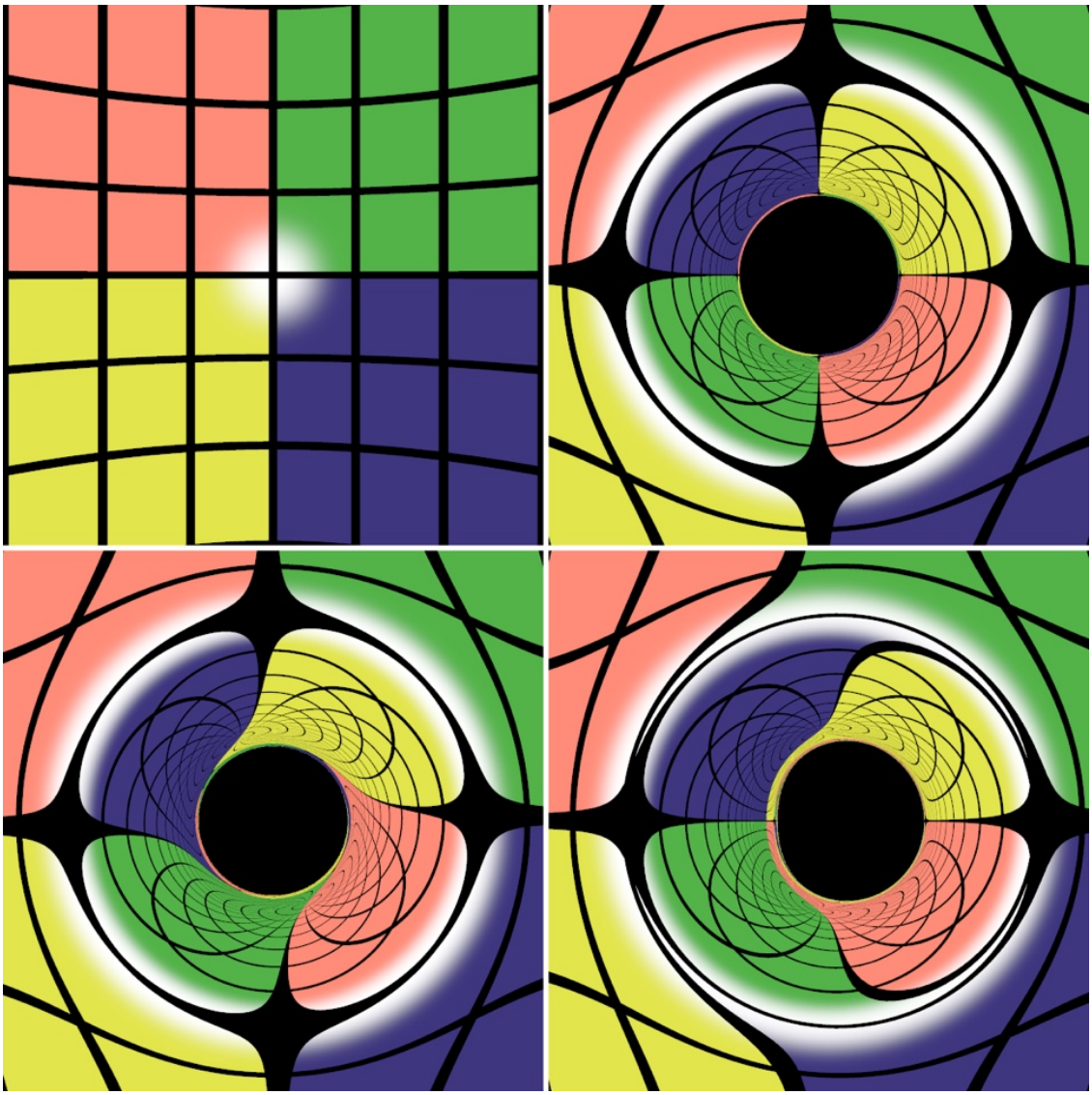

Figure 5.1: Lensing caused by various analytic spacetimes. For all panels, we use figure 5.2 as a background, oriented such that the camera is pointed at the white reference dot. The camera has a 60° field of view and is at a distance of 15 Schwarzschild radii from the origin measured using Kerr-Schild coordinates [25]. The top row shows Minkowski and Schwarzschild spacetimes. The bottom row shows two views of the Kerr spacetime, with dimensionless spin $\chi = 0.95$, viewed with the camera pointing parallel to the spin axis of the black hole (bottom left) and perpendicular to the spin axis (bottom right).

along the spin axis). The spin of the black hole causes frame dragging, where space is dragged in the direction of the rotation [29, 30]. In the bottom left image, the spin axis of the black hole is pointing out of the page, so space is dragged in a counterclockwise motion. The effect of the frame dragging on the photon trajectories produces an image in which the grid itself appears to be dragged by the spin, as is evident when compared to the non-spinning black hole in the top right image. The strength of frame dragging increases closer to the black hole, which can also be inferred from the deformation of the background grid.

Frame dragging manifests differently in the bottom right image, where the spin axis is pointing up. The direction of frame dragging is out of the page on the left of the shadow of the black hole and into the page on the right. A photon traveling in the direction of the frame dragging can orbit closer to the black hole without being captured than a photon traveling opposite the frame dragging direction, resulting in an asymmetrical shadow about the spin axis. This causes the shadow to appear offset relative to the shadow of a Schwarzschild hole.

5.3.2 Binary black hole spacetimes

Astrophysical black hole binaries are expected to radiate energy via gravitational waves, leading to a long inspiral followed by a merger, and finally a ringdown to a steady-state single black hole. Lensing by a final, steady-state black hole will look like the single black holes already seen in figure 5.1. However, the situation becomes more interesting when viewing these systems before merger. The first images we will present show an equal-mass BBH with non-spinning black holes—one of the simplest binary inspiral spacetimes to analyze—shortly before merger. The simulation we use is case 1 of Taylor *et al.* [31].

Figure 5.2 shows the image of our reference grid in the presence of this BBH, where the camera is situated such that the orbital angular momentum is pointing out of the page. This image bears a striking resemblance to the bottom left frame of figure 5.1, excluding the details near the shadows. This shows that, away from the shadows, the spacetime looks similar to a single rotating black hole, where the lensing is dominated by the mass monopole with

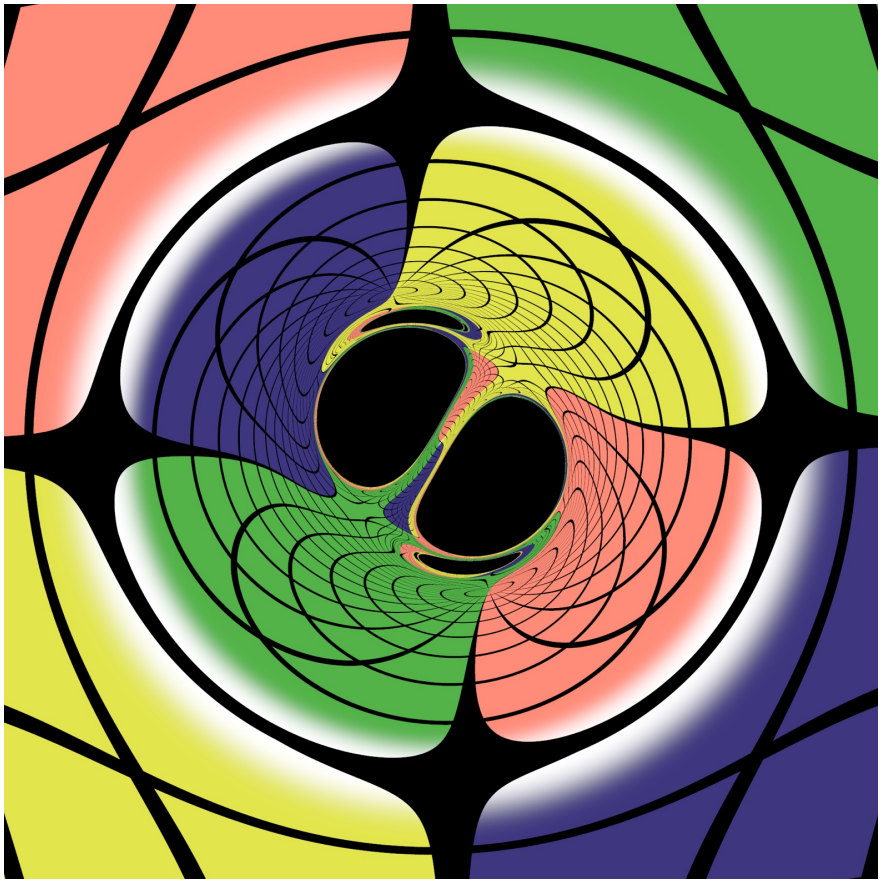

Figure 5.2: A BBH system of equal-mass black holes with no spin, viewed near merger with the orbital angular momentum out of the page.

corrections caused by the angular momentum of the system. In the single-hole case, the spin is responsible for frame dragging, whereas here the orbital angular momentum is responsible.

Focusing on the inner portion of the image, we observe that the binary lensing is markedly different from the Schwarzschild or Kerr cases. Figure 5.3 shows a cropped version of figure 5.2, emphasizing the structure of the shadows. As might be expected, there are two prominent shadows visible, each associated with one of the two black holes. We also see a narrow secondary shadow (an "eyebrow" [13]) close to the outside of each primary shadow. These secondary shadows correspond to one black hole (BH) casting a shadow which is lensed by the other BH on the way to the camera. Equivalently, they are image regions where geodesics are traced backwards from the camera to a BH, but bend around at least one BH on the way there. The first pair of eyebrows is evident in figure 5.3; however, we can resolve a pair of

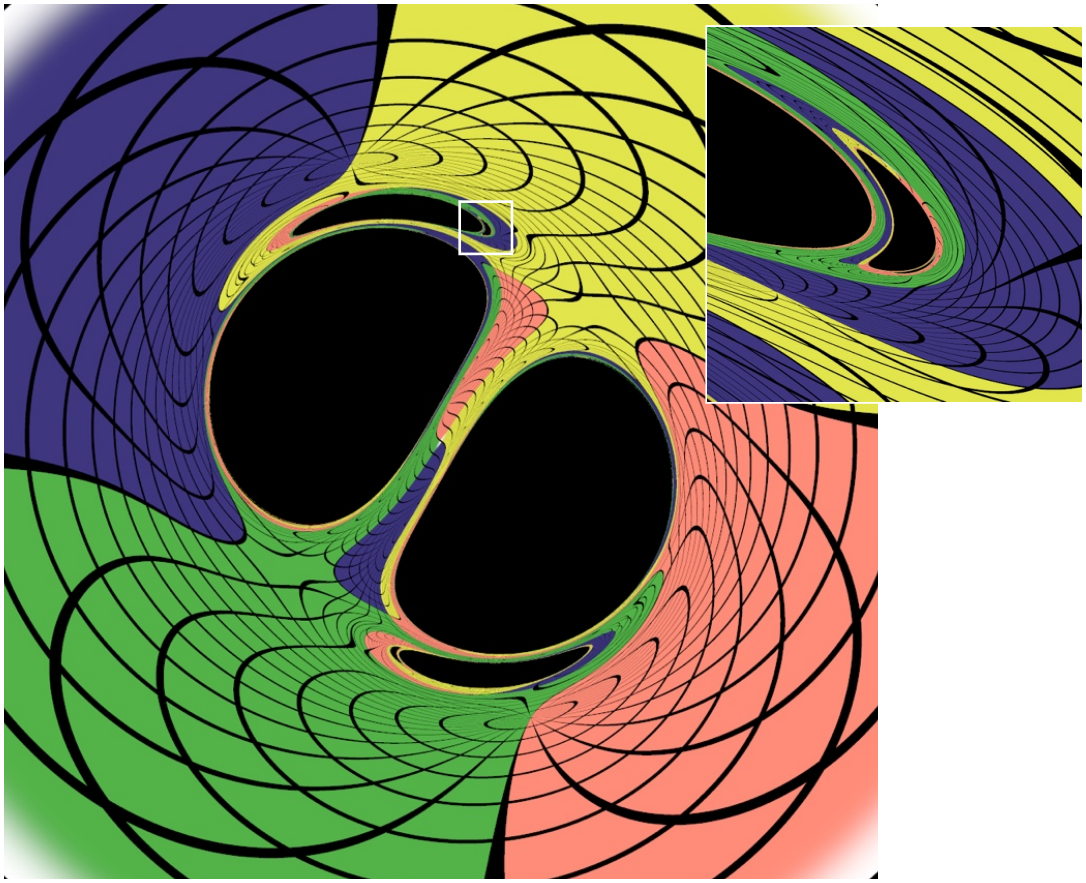

Figure 5.3: A cropped version of figure 5.2 in order to show more detail near the black hole shadows. A small portion of the image (outlined) is enlarged and inset, where a smaller eyebrow is clearly visible.

smaller eyebrows, shown in the inset.

We show another view of the same system in figure 5.4. Here the camera is looking at the system edge on, such that the orbital angular momentum is pointing up. We see again an overall similarity with the corresponding orientation of Kerr spacetime (the bottom-right frame of figure 5.1), indicating the dominant effects of the mass and angular momentum in these images. We can see a primary shadow for each black hole, but in this configuration one black hole is located roughly behind the other and as a result its shadow gets lensed into a dark ring. Extending along the right side of this ring we see a long thin eyebrow, which is shown in the inset, along with another, smaller, eyebrow.

To illustrate how photon trajectories behave near shadows, we plot trajectories of a few

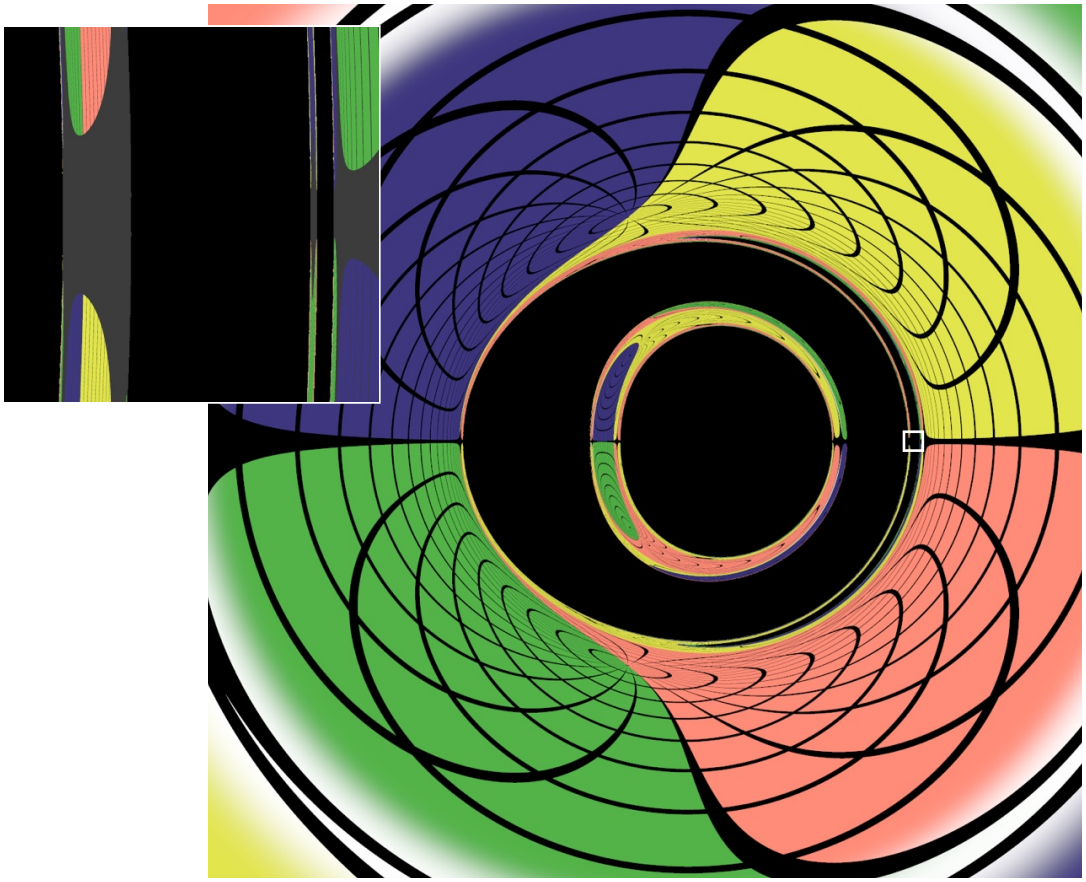

Figure 5.4: The same system as figure 5.3, viewed such that the orbital angular momentum of the system is pointing up. Note that the grid lines in the inset are shown in gray here to distinguish them from the black hole shadows.

geodesics on the horizontal line passing through the middle of figure 5.4 near the eyebrow. Figure 5.5 shows four snapshots of these trajectories in time, with their current locations in each frame denoted by large dots. It is easiest to consider these trajectories as we evolve them, out of the camera and backwards in time, to see where they came from. In frames A–C, we see the trajectories under consideration start close together then diverge significantly, demonstrating how nearby pixels on the image can correspond to vastly different physical locations. In frame D we see the entire trajectories. A few extend to infinity, but most terminate on the black holes; these are denoted by solid lines and dotted lines, respectively. Only the trajectories extending to infinity result in a photon reaching the camera; those that reach the hole on the right of frame D correspond to the primary ring-like shadow in

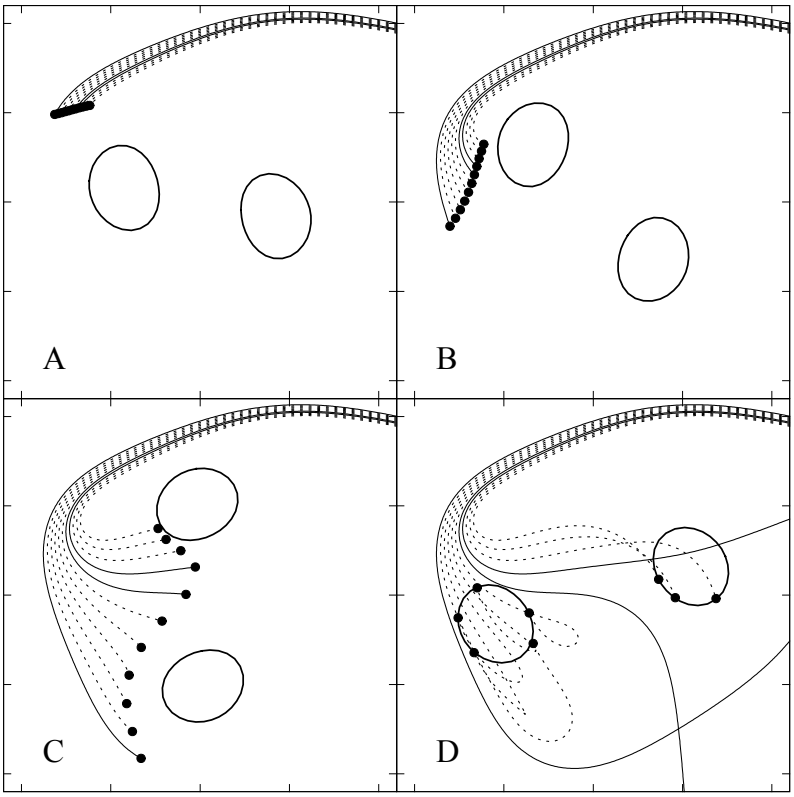

Figure 5.5: Geodesic trajectories plotted in relation to the black hole event horizons during the lensing evolution for figure 5.4. Each frame shows a snapshot in time, with the dots representing the current positions of the geodesics, and the lines indicating the trajectories from the camera. The solid and dashed lines indicate whether the geodesics originate from infinity or from a black hole, respectively.

figure 5.4, while those that reach the left hole correspond to the larger eyebrow visible on the right side of figure 5.4. Note that the black holes are orbiting rapidly, so they move significantly while the photons pass through the system.

We can also uniquely identify which black hole casts each shadow, which enables us to show in figure 5.6 the origin of the photons along the horizontal line across the center of figure 5.4. We arbitrarily label the large shadow in the middle of figure 5.4 as BH 2, and the ring-like shadow as BH 1. Regions where photons reach the camera from infinity are labeled ∞. The top plot in figure 5.6 shows the origin of the photons that reach the camera along the entire middle horizontal line in figure 5.4. We see that each transition from ∞ to

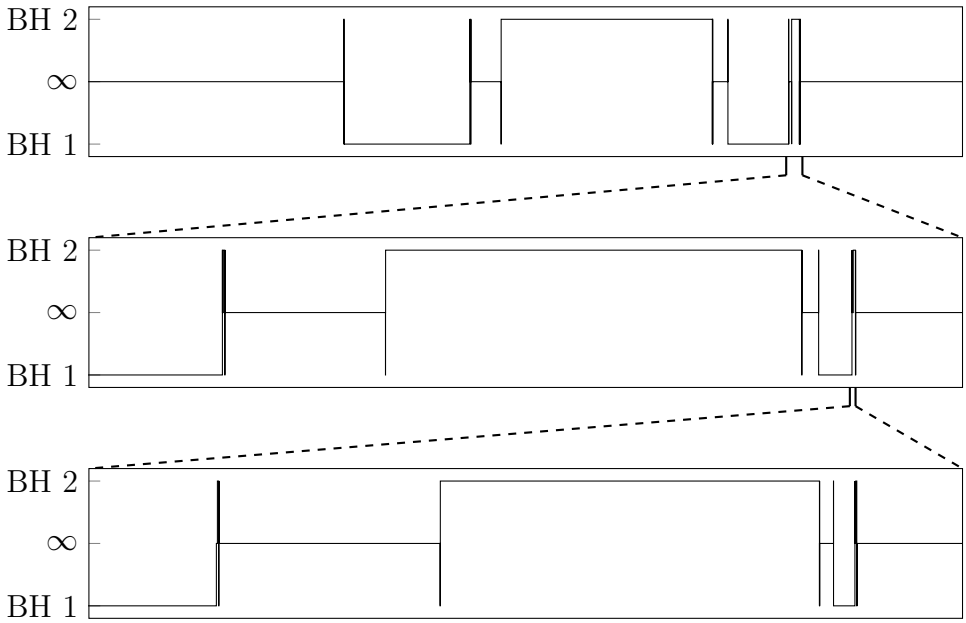

Figure 5.6: Plots identifying the origins of photons along the horizontal line through the center of figure 5.4. Photons coming from infinity are labeled ∞, and the shadows are labeled either BH 1 or BH 2. The first plot corresponds to the main portion of figure 5.4. The second plot focuses on the zoomed square in the inset of figure 5.4, showing a small feature of the first plot. The third plot zooms to a similar feature of the second plot. This figure demonstrates a striking self-similarity of the lensing structure of a binary black hole system.

either of the BHs includes transitions to the other BH. Even though we cannot resolve them numerically, each vertical line in principle contains infinitely many transitions. To illustrate this idea, the second plot in figure 5.6 investigates the group of shadows indicated by the zoomed inset of figure 5.4. Here we find a structure which resembles the first plot. The third plot in figure 5.6 zooms to a similar group of shadows on the right side of the second plot to again reveal the same structure. This figure clearly shows evidence of self-similarity in the structure of BBH lensing, where the smaller length scales explore more photon orbits through the system. Furthermore, the structure of shadows in BBH lensing is more complex than figures 5.3 and 5.4 appear to suggest. The shadows these images focus on are merely some of the largest visible shadows, associated with simpler geodesic orbits around the binary.

If we consider this equal-mass BBH earlier in the inspiral when its separation is large, the black holes are only weakly interacting. Therefore most camera viewpoints of this binary

will yield images with two primary shadows, one for each black hole. Each shadow will be similar to an isolated Schwarzschild or Kerr shadow but with the addition of small eyebrows. However, when the binary is viewed edge-on and the black holes are nearly aligned with the camera, we see an interesting image.

Figure 5.7 shows the equal-mass binary in this configuration, hundreds of orbits before merger. Just as in figure 5.4, the more distant black hole is lensed into a ring-like shadow; however, the ring is thinner here, primarily because of the large separation of the binary. The angular momentum causes the lensed grid outside the shadows to strongly resemble lensing by a Kerr black hole rather than lensing by a Schwarzschild black hole. In addition to the usual primary Einstein ring, another ring is visible between these shadows. Both of these rings correspond to the same source of light, which is in front of the camera and behind the BBH. The second Einstein ring is caused by photons following an "S"-shaped trajectory through the system.

The second binary system we consider is a fully generic black hole binary with a mass ratio of $m_1/m_2 = 3$ and black hole spins of $\chi_1 = 0.7$ and $\chi_2 = 0.3$ in arbitrary directions. This is case 4 of Taylor *et al.* [31]. In figure 5.8 we see a top view of this system, in analogy with what is presented in figure 5.3. Away from the shadows, the lensing is similar to a single black hole with spin, as was seen with the equal-mass binary images. This appears to be a generic feature of lensing from orbiting BBHs. We can clearly see that the symmetry present in the equal-mass system is gone. The unequal masses evidently change the relative sizes of not only the primary shadows, but all additional shadows as well. The inset in figure 5.8 zooms to show two successively smaller eyebrows near the small black hole's primary shadow. However, the effects of the black holes' spins are not at all clear from this viewpoint.

In figure 5.9 we see the same binary as in figure 5.8, viewed with the orbital angular momentum pointing upward, in analogy with figure 5.4. We again see that, away from the shadows, the system looks like a Kerr black hole. The unequal mass ratio is apparent here, with the smaller black hole lensing the shadow of the larger black hole into a partial ring. If

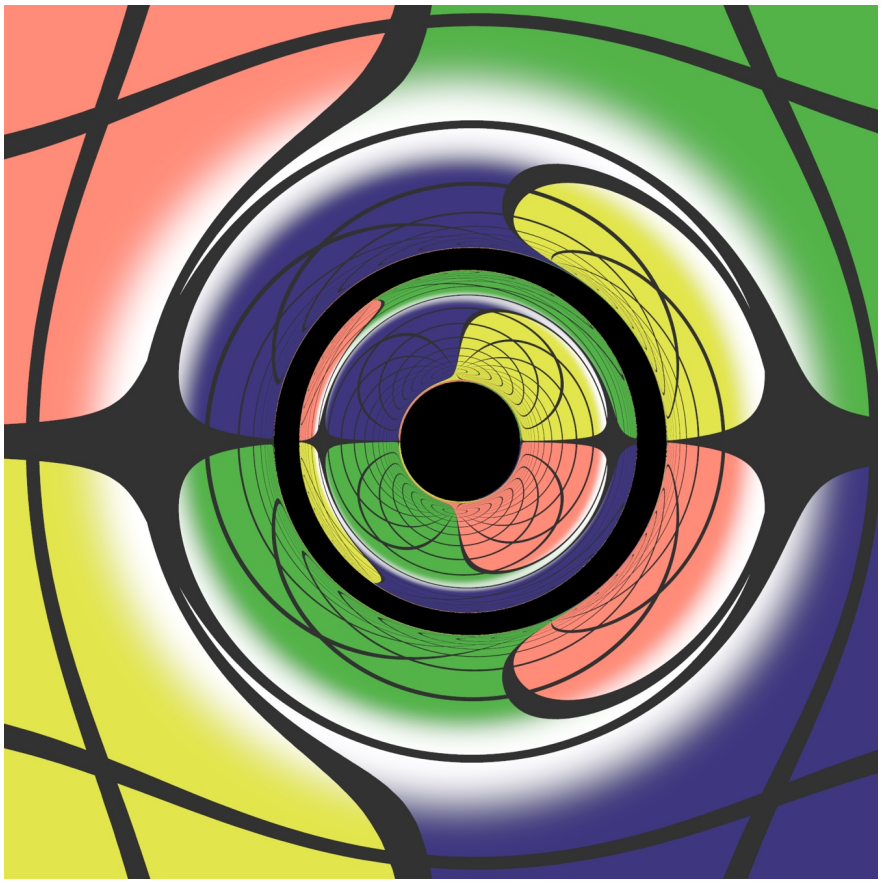

Figure 5.7: A BBH system of equal-mass black holes with no spin, viewed hundreds of orbits before merger, with the orbital angular momentum pointing up. The distance from the camera to the closer black hole in this figure is the same as in figure 5.4. Note that the grid lines are shown in gray here to distinguish them from the black hole shadows.

it were not for the black hole spins, the lensing by the binary would be symmetric, giving either a ring-like shadow similar to figure 5.4 or a shadow and a very thick eyebrow. In this particular BBH, the effect of the individual black hole spins on the image depends strongly on the camera position.

5.4 Conclusions

In this paper, we present the first images of gravitational lensing by astrophysically relevant binary black holes, thereby providing a realistic representation of what an observer near such a system would actually see. To accomplish this, we have developed a new set of equations

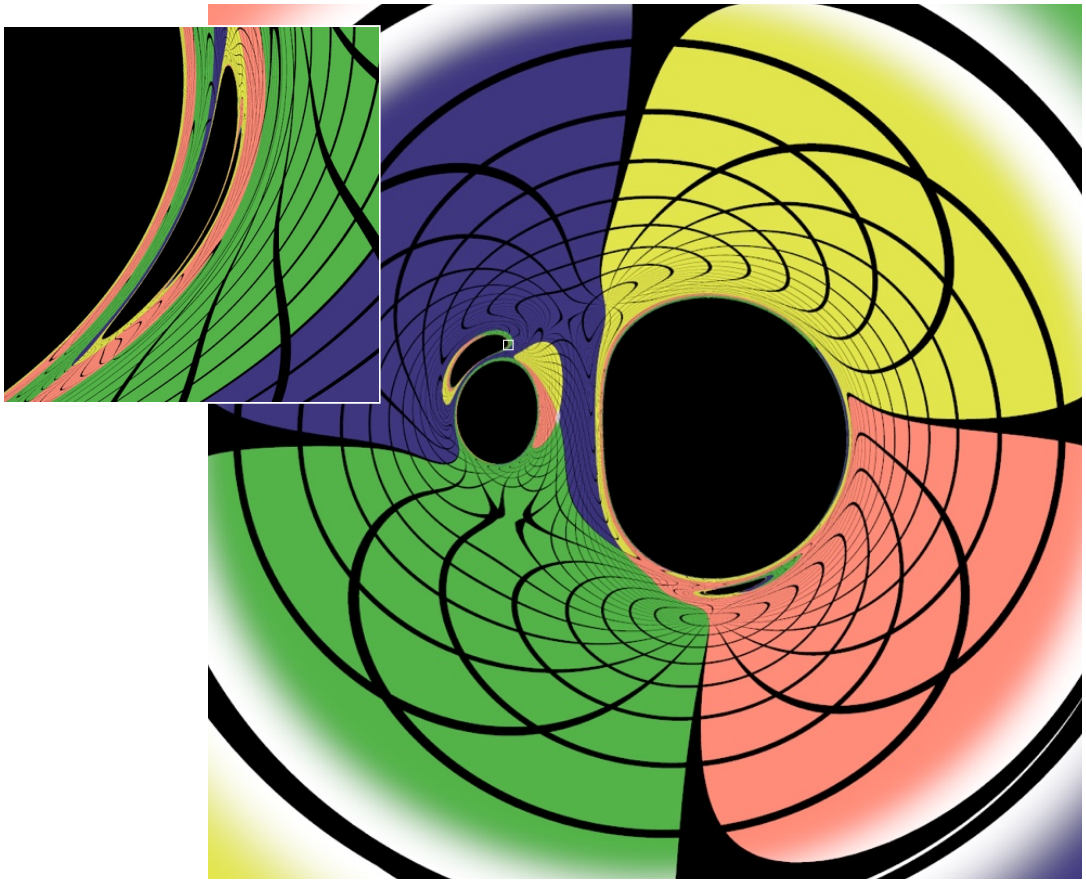

Figure 5.8: A view of a binary inspiral of mass ratio $m_1/m_2 = 3$ near merger, with the orbital angular momentum approximately pointing out of the page. The black hole spins are $\chi_1 = 0.7$ and $\chi_2 = 0.3$ in arbitrary directions. This figure is analogous to figure 5.3. As in previous figures, a small portion of the image is enlarged and inset, displaying additional eyebrows.

that evolve photons efficiently near black hole horizons. Our images show there is a primary shadow—a region where the black hole prevents light from reaching the camera—for each black hole, as well as multiple secondary shadows (or eyebrows).

We have found that, early in the inspiral, images of a BBH look similar to two separate Kerr black hole shadows, unless viewed when the holes are nearly collinear with the camera. Shortly before the merger, all camera angles yield interesting images of not just one shadow for each black hole, but a handful of smaller visible shadows. We showed for an equal-mass binary viewed edge-on that the lensing structure exhibits self-similarity on smaller scales, corresponding to photons taking an increasing number of orbits through the system. Lensing

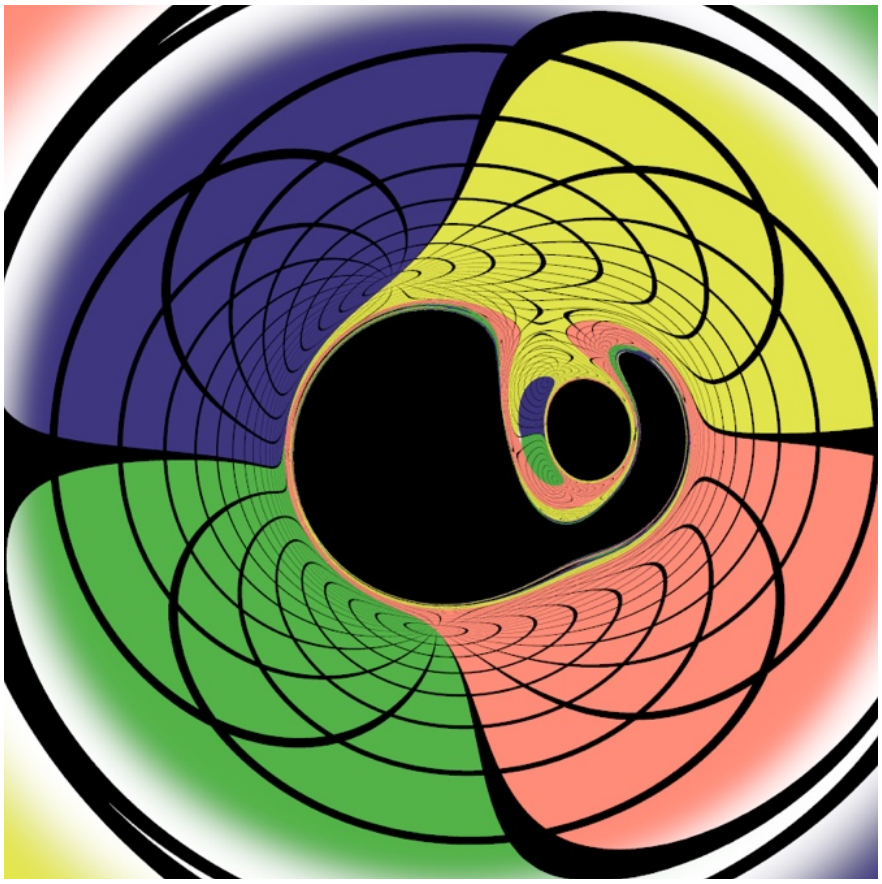

Figure 5.9: Another view of the BBH in figure 5.8, but with orbital angular momentum pointing up. The camera parameters are otherwise identical. This figure is analogous to figure 5.4; however, because of the asymmetry from the black hole spins, the larger black hole's shadow is not lensed completely around the small black hole.

by a fully generic BBH illustrated that the spin of black holes in a binary can have a clear effect on the lensed shadows.

We chose not to classify eyebrows and shadows into a hierarchy in this paper. In the inset of figure 5.3, for instance, identifying the largest eyebrow as the primary eyebrow and the next largest as the secondary eyebrow feels very natural, but the exact definition of such a hierarchy is not immediately clear. For example, simply specifying a geodesic winding number around each black hole is likely not to be sufficient. In addition to the trajectories not lying in a plane, the order that a geodesic orbits the black holes does not commute. Furthermore, the black holes are moving at comparable speeds to the geodesics. For these reasons, we leave the task of classifying shadows as future work.

We have also shown in this paper that, away from the shadows, an image of a binary black hole system looks like that of an isolated black hole. Thus it is necessary to resolve individual shadows in order to discern the unique visual characteristics present in such images, which places limits on our ability to observe them.

For systems involving matter, however, the combination of the lensing effects of strong gravity with the disruption and distortion of radiation-emitting matter might yield a unique optical signature. Generating lensed images of black hole-neutron star and neutron star-neutron star mergers is an avenue of future investigation. The techniques presented here would allow us to produce detailed visualizations of these mergers; integrating over such images, we could predict the optical signature of an unresolved system.

Bibliography

[1] Sjur Refsdal. The gravitational lens effect. *Mon. Not. Roy. Astr. Soc.*, 128(4):295–306, 1964.

[2] R. D. Blandford and R. Narayan. Cosmological applications of gravitational lensing. *Annual Review of Astronomy and Astrophysics*, 30(1):311–358, 1992.

[3] Naohisa Inada, Masamune Oguri, Bartosz Pindor, Joseph F Hennawi, Kuenley Chiu, Wei Zheng, Shin-Ichi Ichikawa, Michael D Gregg, Robert H Becker, Yasushi Suto, et al. A gravitationally lensed quasar with quadruple images separated by 14.62 arcseconds. *Nature*, 426(6968):810–812, 2003.

[4] Naohisa Inada, Masamune Oguri, Tomoki Morokuma, Mamoru Doi, Naoki Yasuda, Robert H. Becker, Gordon T. Richards, Christopher S. Kochanek, Issha Kayo, Kohki Konishi, Hiroyuki Utsunomiya, Min-Su Shin, Michael A. Strauss, Erin S. Sheldon, Donald G. York, Joseph F. Hennawi, Donald P. Schneider, Xinyu Dai, and Masataka Fukugita. SDSS J1029+2623: A gravitationally lensed quasar with an image separation of $22''.5$. *Astrophys. J. Lett.*, 653(2):L97, 2006.

[5] C. T. Cunningham and J. M. Bardeen. The Optical Appearance of a Star Orbiting an Extreme Kerr Black Hole. *Astrophys. J. Lett.*, 173:L137, May 1972.

[6] J.-P. Luminet. Image of a spherical black hole with thin accretion disk. *Astron. Astrophys.*, 75:228–235, May 1979.

[7] F.H. Vincent, T. Paumard, E. Gourgoulhon, and G. Perrin. GYOTO: a new general relativistic ray-tracing code. *Class. Quantum Grav.*, 28:225011, 2011, 1109.4769.

[8] Thomas Müller. GeoViS—Relativistic ray tracing in four-dimensional spacetimes. *Comput. Phys. Commun.*, 185(8):2301 – 2308, 2014.

[9] Sudhansu Datta Majumdar. A class of exact solutions of Einstein's field equations. *Phys. Rev.*, 72:390–398, Sep 1947.

[10] Achilles Papapetrou. A static solution of the equations of the gravitational field for an arbitrary charge-distribution. *Proc. Roy. Irish Acad.*, A 51:191–204, 1947.

[11] David Kastor and Jennie Traschen. Cosmological multi-black-hole solutions. *Phys. Rev. D*, 47:5370–5375, Jun 1993.

[12] Daisuke Nitta, Takeshi Chiba, and Naoshi Sugiyama. Shadows of colliding black holes. *Phys. Rev. D*, 84:063008, Sep 2011.

[13] Akifumi Yumoto, Daisuke Nitta, Takeshi Chiba, and Naoshi Sugiyama. Shadows of multi-black holes: Analytic exploration. *Phys. Rev. D*, 86:103001, Nov 2012.

[14] http://www.black-holes.org/lensing.

[15] Joan Centrella, John G. Baker, Bernard J. Kelly, and James R. van Meter. Black-hole binaries, gravitational waves, and numerical relativity. *Rev. Mod. Phys.*, 82:3069, 2010, 1010.5260.

[16] Harald P. Pfeiffer. Numerical simulations of compact object binaries. *Class. Quantum Grav.*, 29:124004, 2012, 1203.5166.

[17] R. Arnowitt, S. Deser, and Charles W. Misner. The dynamics of general relativity. In L. Witten, editor, *Gravitation: An Introduction to Current Research*, pages 227–265. Wiley, New York, 1962, gr-qc/0405109.

[18] http://www.black-holes.org/SpEC.html.

[19] Simulating eXtreme Spacetimes. http://www.black-holes.org/.

[20] Béla Szilágyi, Lee Lindblom, and Mark A. Scheel. Simulations of binary black hole mergers using spectral methods. *Phys. Rev. D*, 80:124010, 2009, 0909.3557.

[21] Daniel A. Hemberger, Mark A. Scheel, Lawrence E. Kidder, Béla Szilágyi, Geoffrey Lovelace, Nicholas W. Taylor, and Saul A. Teukolsky. Dynamical excision boundaries in spectral evolutions of binary black hole spacetimes. *Class. Quantum Grav.*, 30(11):115001, 2013, 1211.6079.

[22] http://www.black-holes.org/waveforms.

[23] S. A. Hughes, C. R. Keeton, P. Walker, K. T. Walsh, S. L. Shapiro, and S. A. Teukolsky. Finding black holes in numerical spacetimes. *Phys. Rev. D*, 49:4004, 1994.

[24] F.H. Vincent, E. Gourgoulhon, and J. Novak. 3+1 geodesic equation and images in numerical spacetimes. *Class. Quantum Grav.*, 29(24):245005, 2012.

[25] Charles W. Misner, Kip S. Thorne, and John Archibald Wheeler. *Gravitation*. Freeman, New York, New York, 1973.

[26] M. F. Skrutskie, R. M. Cutri, R. Stiening, M. D. Weinberg, S. Schneider, J. M. Carpenter, C. Beichman, R. Capps, T. Chester, J. Elias, J. Huchra, J. Liebert, C. Lonsdale, D. G. Monet, S. Price, P. Seitzer, T. Jarrett, J. D. Kirkpatrick, J. E. Gizis, E. Howard, T. Evans, J. Fowler, L. Fullmer, R. Hurt, R. Light, E. L. Kopan, K. A. Marsh, H. L. McCallon, R. Tam, S. Van Dyk, and S. Wheelock. The two micron all sky survey (2MASS). *The Astronomical Journal*, 131(2):1163, 2006.

[27] Silvia Mollerach and Esteban Roulet. *Gravitational Lensing and Microlensing*. World Scientific, 2002.

[28] Albert Einstein. Lens-like action of a star by the deviation of light in the gravitational field. *Science*, 84(2188):506–507, 1936.

[29] H. Thirring. Über die Wirkung rotierender ferner Massen in der Einsteinschen Gravitationstheorie. *Physikalische Zeitschrift*, 19:33, 1918.

[30] H. Thirring. Berichtigung zu meiner Arbeit: "Über die Wirkung rotierender Massen in der Einsteinschen Gravitationstheorie". *Physikalische Zeitschrift*, 22:29, 1921.

[31] Nicholas W. Taylor, Michael Boyle, Christian Reisswig, Mark A. Scheel, Tony Chu, Lawrence E. Kidder, and Béla Szilágyi. Comparing gravitational waveform extrapolation to Cauchy-characteristic extraction in binary black hole simulations. *Phys. Rev. D*, 88:124010, Dec 2013, 1309.3605.

6 Miscellaneous gravitational lensing projects

The gravitational lensing code described in Chapter 5 can handle a wide range of systems in addition to merging black holes. We have investigated the Majumdar-Papapetrou static binary black hole solution [1], the Alcubierre warp drive metric [2], cosmic string lensing, and other systems. We present here a subset of various gravitational lensing projects over the past few years.

6.1 GW150914 Press Conference

In September 2015, the Advanced LIGO interferometers detected the gravitational radiation from a pair of merging black holes [3]. I was not a member of the LIGO Science Collaboration (LSC) at the time of the detection. As preparations began for the press conference scheduled for February 2016, the LSC decided to invite me into the collaboration in December 2015 to prepare a gravitational lensing video that would headline the event.

Geoffrey Lovelace and his students had already run a binary black hole simulation with parameters consistent with the detected binary. Using this binary, I spent the month of January testing camera parameters star field parameters, and managing simulations for a 30 second video at 30 frames per second resulting in 900 frames, each requiring an individual raytracing. No new technology beyond our gravitational lensing paper [4] was required for these simulations, yet our simulation pipeline requires significant manual labor and babysitting for large videos at this time.

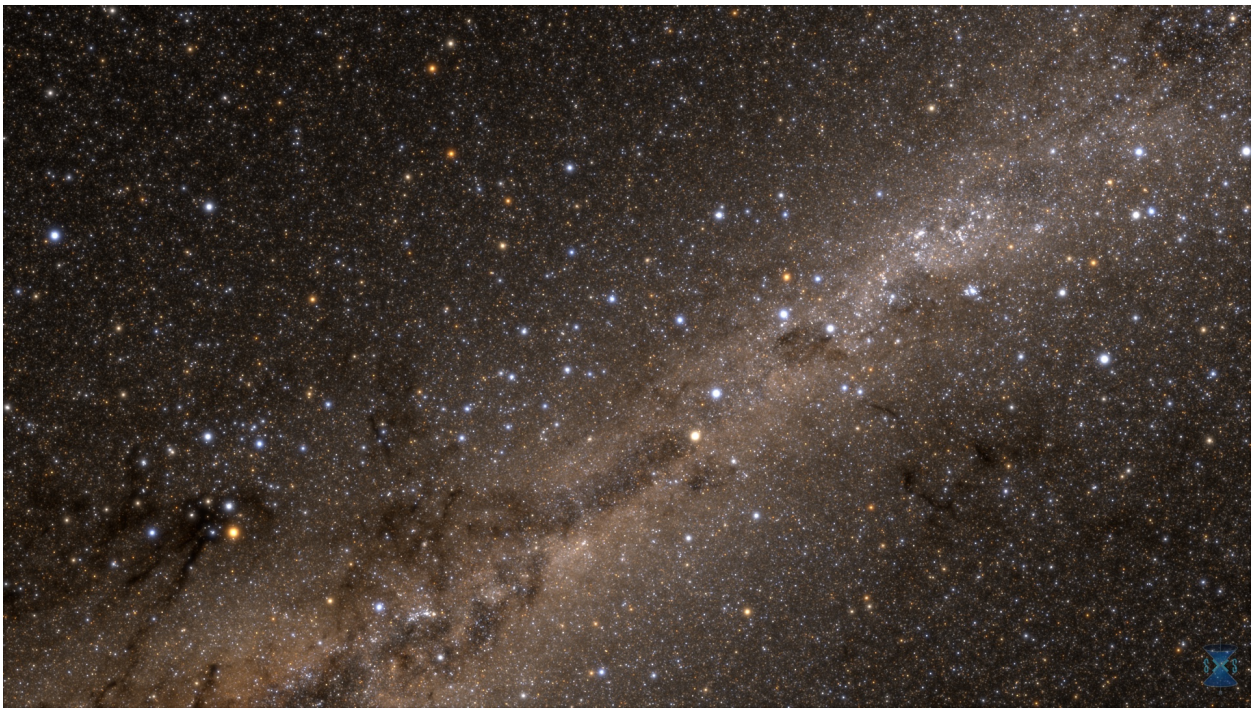

Figure 6.1: Simulated Milky Way starfield with no light deflection. This camera direction and these starfield parameters were used for the lensing of the binary LIGO detected, GW150914, shown in Figure 6.2.

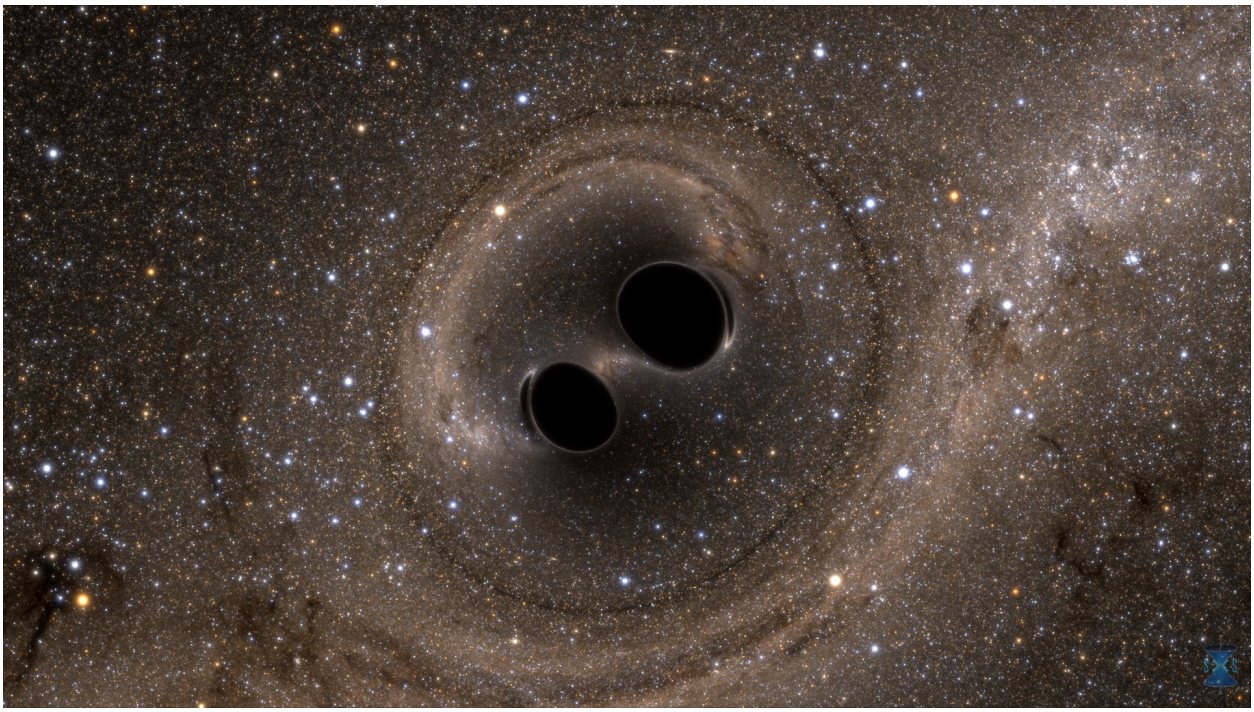

Figure 6.2: Simulation with parameters consistent with the binary black hole merger detected by LIGO. Figure 6.1 shows an image of what the starfield looks like without the black hole binary. This image shows what the binary might have looked like for a close up observer.

Figure 6.1 shows a simulated starfield, with the camera pointing toward the Milky Way galaxy. Many details of the star rendering code are not published yet, but the rest of the raytracing code is presented in Bohn *et al.* [4]. Adding the binary, we obtain Figure 6.2.

Unlike most gravitational lensing images with stars, we use a large star catalog as a background instead of an image. By generating our starfield images from a catalog of point sources, we obtain a substantially more realistic image than would be generated by applying the lensing deformation to a raster image of the unlensed Milky Way stars. In such a raster image, each star is usually represented (whether as a result of camera optics or software rendering) as a blurred circle whose area depends on the star's brightness. These circles are typically hundreds of arc seconds wide, and therefore lensing distortions applied to the image tend to produce stars that appear as smeared ellipses. In contrast, the angular sizes of real stars are many orders of magnitude smaller, so we expect them to remain as unresolved points under all but the most extreme lensing magnifications. These unresolved points can then be rendered as previously described, giving stars that better portray what an observer would actually see. The difference between these methods lies in the non-commutativity between the lensing deformations and the blurring of each star.

The full 30 second video can be viewed in the LIGO press conference, a full resolution video on the our collaboration's webpage [5] at `http://www.black-holes.org/videos/bbh_gw/creditsmovie.mp4`, or on the Youtube channel for the Simulating eXtreme Spacetimes collaboration [6].

6.2 Accretion disks around black holes

Authors: Andy Bohn, William Throwe, François Hébert

After the movie Interstellar featured a magnificent accretion disk around a rotating black hole, we decided to test how scientifically accurate the accretion disk lensing truly was. In Interstellar, there is a planet orbiting the super-massive black hole Gargantua such that one hour on the planet is seven years back on Earth. Kip Thorne found a way to accomplish such

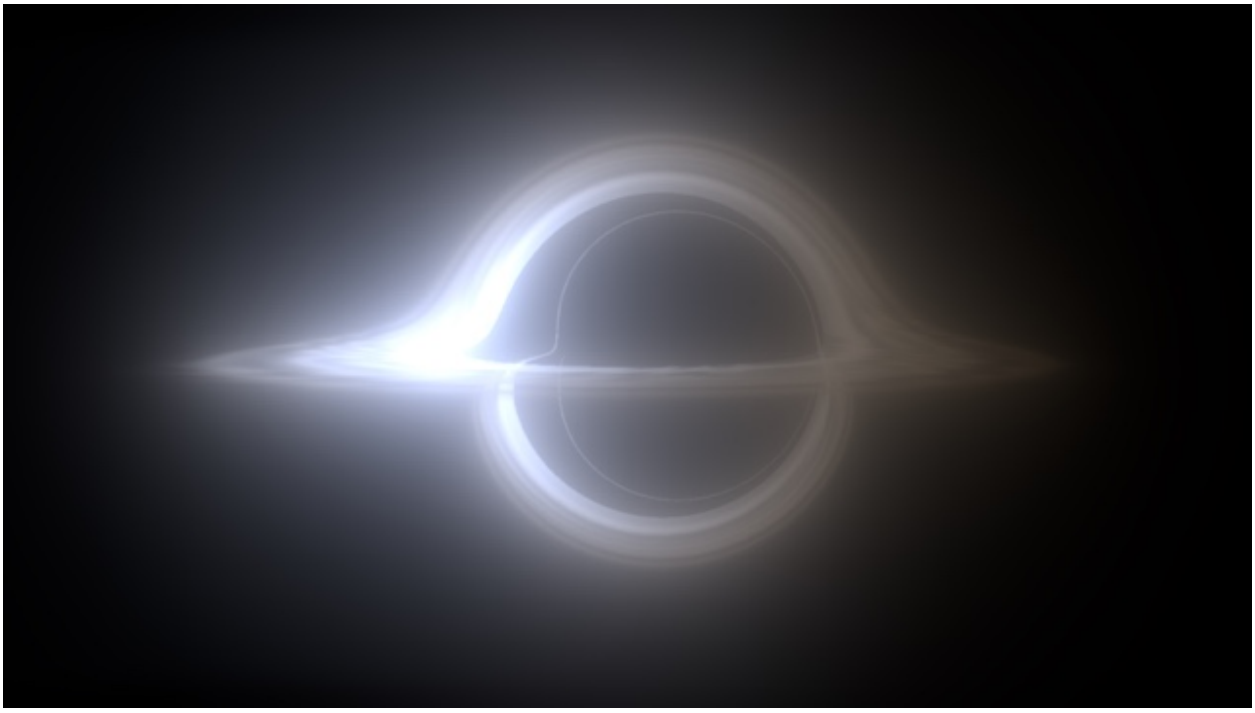

Figure 6.1: Accretion disk around a maximally spinning black hole.

an incredible time dilation by making Gargantua have nearly maximal spin [7]. Normally the innermost stable circular orbit (ISCO) for a non-spinning black hole is at a radius of $6M$, where M is the mass of the black hole. Inside this radius, there are no stable orbits around the black hole, so the object would eventually fall into the black hole. However, the ISCO for a prograde orbit around a maximally spinning black hole falls down to $1M$, allowing the planet to orbit much closer to the black hole Gargantua. The mass of the black hole is irrelevant for the lensing, since all the imagery scales with the total mass.

Figure 6.1 shows our accretion disk around a maximally spinning black hole. The accretion disk is infinitesimally thin and is not gravitating, so the spacetime is simply Kerr where the metric is analytic. Our accretion disk is in the equatorial plane of the black hole, $5M < r < 17M$. The temperature in the disk follows a standard profile $T(r) \propto r^{-3/4}$. The matter is assumed to follow circular orbits around the black hole with an equatorial orbital velocity. To make the disk more interesting, we added arbitrary density and temperature variations through the disk.

There are a few major difference between our disk and the Interstellar disk. Because the disk is orbiting the black hole, the photons from the left and the right side of the disk are significantly Doppler shifted, causing the left side to appear bright blue and the right side to appear dim and red. We have not drawn any stars in our image, because the light from stars would be completely drowned out by the bright accretion disk. Finally, the maximal spin on the black hole causes the left edge of the black hole shadow to correctly look flat in our image. The producers of Interstellar decided to reduce the spin of the black hole for the imagery to hide this flat edge and avoid additional confusion for the audience [7].

In both disks, we see the disk appear to wrap above and below the black hole. Photons emitted from the disk on the far side of the black hole are deflected by the black hole and bent toward the camera, causing the disk to appear to wrap over the black hole. Similarly, the disk appears to wrap below the black hole. Additionally, we can see what appears to be an inner ring around the black hole shadow, from photons that partially orbit the black hole before arriving at the camera.

While tracing rays backwards in time from the camera, we constantly search for collisions between the ray and the disk. Because the disk is partially transparent, we construct the image through layers. We first trace rays that collide with the disk only if they intersect the disk from above. We perform another tracing of rays that collide with the disk only if they intersect the disk from below. We need to handle the cases where photons do an orbit around the black hole and so forth. In the imaging step, we layer all these partially transparent disks together to get a physically realistic image.

Figure 6.2 shows the same system, but with a dimensionless black hole spin of 0.6, matching the black hole used in Interstellar. Compared to Figure 6.1, it is clear that the black hole shadow is more round on the left side.

In the future, we would like to create more physically accurate lensing with problems involving matter. We will use numerically evolved matter sources, such as neutron stars, accretion disks around black holes, and various binary systems.

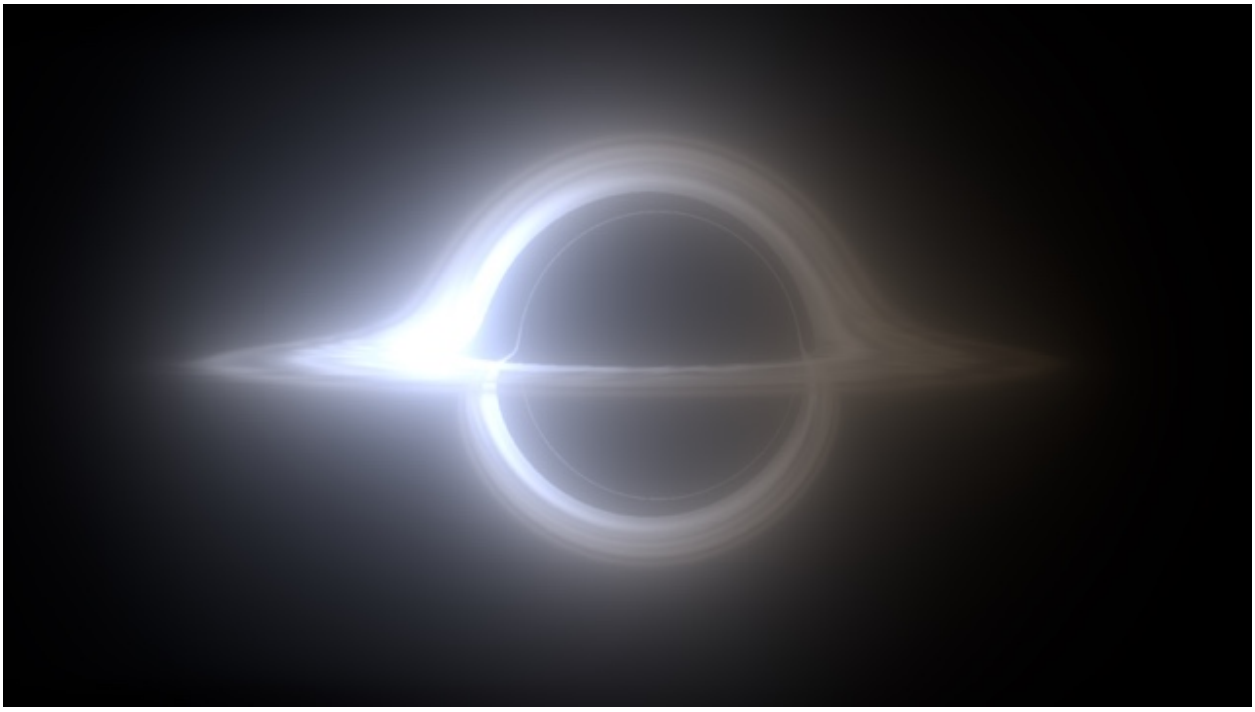

Figure 6.2: Accretion disk around a dimensionless spin 0.6 black hole, matching the black hole spin used for the Interstellar imagery.

Bibliography

[1] Sudhansu Datta Majumdar. A class of exact solutions of Einstein's field equations. *Phys. Rev.*, 72:390–398, Sep 1947.

[2] Miguel Alcubierre. The warp drive: hyper-fast travel within general relativity. *Classical and Quantum Gravity*, 11(5):L73, 1994.

[3] B. P. Abbott et al. Observation of Gravitational Waves from a Binary Black Hole Merger. *Phys. Rev. Lett.*, 116(6):061102, 2016, 1602.03837.

[4] Andy Bohn, William Throwe, François Hébert, Katherine Henriksson, Darius Bunandar, Mark A Scheel, and Nicholas W Taylor. What does a binary black hole merger look like? *Class. Quantum Grav.*, 32(6):065002, 2015.

[5] Simulating eXtreme Spacetimes. http://www.black-holes.org/.

[6] SXS Collaboration youtube channel. https://www.youtube.com/user/SXSCollaboration.

[7] K. Thorne and C. Nolan. *The Science of Interstellar*. W. W. Norton, 2014.